

AD-A174 579

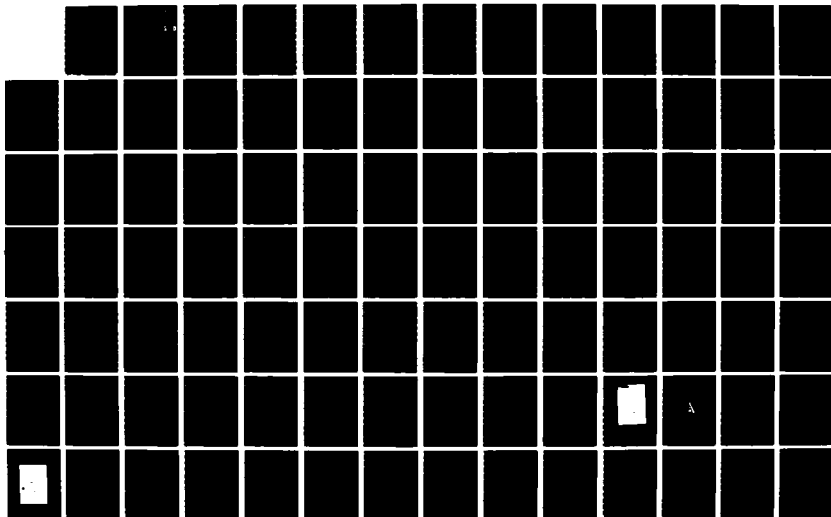
THE ROLE OF THE PLASMA DURING LASER-GAS LASER-METAL
INTERACTIONS (U) ILLINOIS UNIV AT URBANA DEPT OF
MECHANICAL AND INDUSTRIAL ENG T J ROCKSTROM ET AL

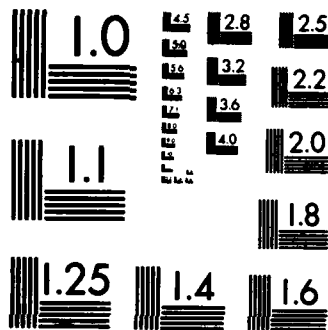
1/3

UNCLASSIFIED

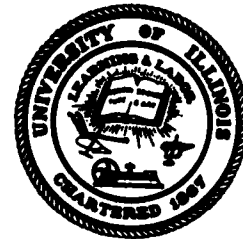
13 OCT 86 UILU-ENG-86-4011 AFOSR-TR-86-1052 F/G 20/5

NL





MICROCOPY RESOLUTION TEST CHART
NATIONAL BUREAU OF STANDARDS-1963-A



2

Department of Mechanical
and Industrial Engineering

University of Illinois at Urbana-Champaign
Urbana, IL 61801

Approved for public release;
distribution unlimited.

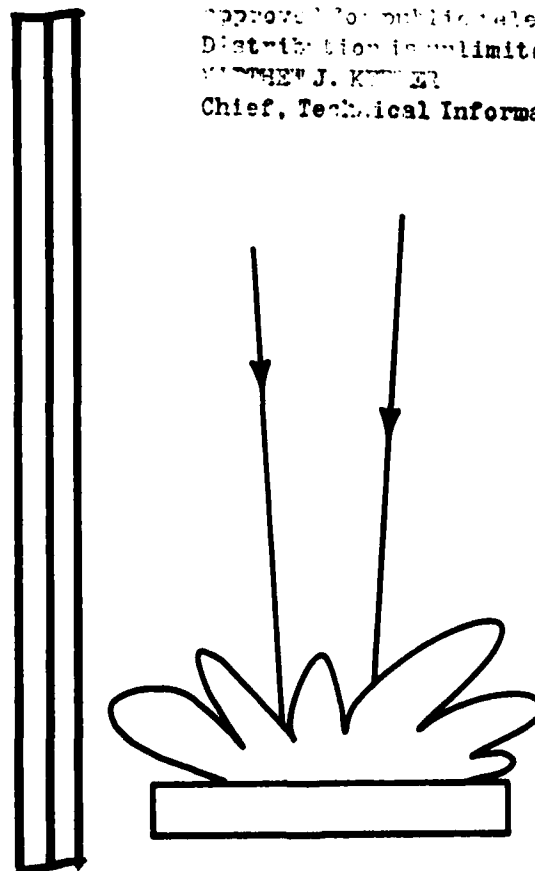
THE ROLE OF THE PLASMA DURING LASER-GAS
LASER-METAL INTERACTIONS

Todd J. Rockstroh and Jyotirmoy Mazumder

DTIC
ELECTE
NOV 26 1986
S D

AD-A174 579

AIR FORCE OFFICE OF SCIENTIFIC RESEARCH (AFSC)
RESEARCH REPORT
This report has been reviewed and is
approved for public release IAW AFR 190-12.
Distribution is unlimited.
MATTHEW J. KUMER
Chief, Technical Information Division



Laser
Applications
and
Materials
Processing

DISTRIBUTION STATEMENT A
Approved for public release;
Distribution Unlimited

DTIC FILE COPY

Unclassified		REPORT DOCUMENTATION PAGE	
1a. REPORT SECURITY CLASSIFICATION Unclassified		1b. RESTRICTIVE MARKINGS None	
2a. SECURITY CLASSIFICATION AUTHORITY		3. DISTRIBUTION/AVAILABILITY OF REPORT	
2b. DECLASSIFICATION/DOWNGRADING SCHEDULE		Approved for Public Release; Distribution Unlimited	
4. PERFORMING ORGANIZATION REPORT NUMBER(S) UILU ENG-86-4011		5. MONITORING ORGANIZATION REPORT NUMBER(S) AFOSR-TR- 86 - 1052	
6a. NAME OF PERFORMING ORGANIZATION University of Illinois at Urbana-Champaign	6b. OFFICE SYMBOL (if applicable) UILU	7a. NAME OF MONITORING ORGANIZATION Air Force Office of Scientific Research	
6c. ADDRESS (City, State, and ZIP Code) Department of Mech. and Ind. Engineering 1206 West Green Street Urbana, IL 61801		7b. ADDRESS (City, State, and ZIP Code) Attn: Dr. Robert Vondra Bolling Air Force Base, DC 20332	
8a. NAME OF FUNDING/SPONSORING ORGANIZATION Air Force Office of Scientific Research	8b. OFFICE SYMBOL (if applicable) AFOSR/NA	9. PROCUREMENT INSTRUMENT IDENTIFICATION NUMBER AFOSR Grant No. 83-0041	
8c. ADDRESS (City, State, and ZIP Code) AFOSR/NA Dr. Robert Vondra Bolling Air Force Base, DC 20332		10. SOURCE OF FUNDING NUMBERS	
		PROGRAM ELEMENT NO. 61102F	TASK NO. 2308
		WORK UNIT ACCESSION NO. A1	
11. TITLE (Include Security Classification) The Role of the Plasma during Laser-Gas and Laser-Metal Interactions			
12. PERSONAL AUTHOR(S) Todd J. Rockstroh and Jyotirmoy Mazumder			
13a. TYPE OF REPORT Interim Tech. Report		13b. TIME COVERED FROM 2/11/85 TO 9/30/86	14. DATE OF REPORT (Year, Month, Day) 13 October 1986
15. PAGE COUNT			
16. SUPPLEMENTARY NOTATION			
17. COSATI CODES		18. SUBJECT TERMS (Continue on reverse if necessary and identify by block number)	
FIELD	GROUP	SUB-GROUP	
		Laser propulsion, Beamed energy propulsion, Laser-sustained plasmas, Laser material processing, Laser-plasma interaction	
19. ABSTRACT (Continue on reverse if necessary and identify by block number)			
<p>The regime of CW laser-plasma-target interaction at intensities below 10^7 W/cm² has been overlooked except for a few studies of gas assist configurations. The recent advances in industrial laser material processing and modeling efforts warrant a detailed study of laser-plasma-target interactions. The University's 10 kW CW CO₂ laser facility has been used to study both pure gas and metal-gas plasmas. Spectroscopic diagnostics have been applied to measure temperature in the plasma core where local electron temperatures are in excess of 10,000 K.</p>			
20. DISTRIBUTION/AVAILABILITY OF ABSTRACT <input type="checkbox"/> UNCLASSIFIED/UNLIMITED <input checked="" type="checkbox"/> SAME AS RPT. <input checked="" type="checkbox"/> DTIC USERS		21. ABSTRACT SECURITY CLASSIFICATION Unclassified	
22a. NAME OF RESPONSIBLE INDIVIDUAL Dr. Robert Vondra		22b. TELEPHONE (Include Area Code) 202-767-4937	22c. OFFICE SYMBOL AFOSR/NA

19. ABSTRACT (continued)

The pure gas studies were performed in argon plasmas in support of a laser propulsion investigation. The pure gas effort allowed the development of the spectroscopic diagnostics and reduction techniques in a relatively simple monatomic plasma. The results indicate that the flowing pure argon plasma can absorb nearly 80 percent of the incident laser power and that more than 25 percent of the incident laser energy is available for conversion to thrust. The pure gas spectroscopic results were verified via independent measurement techniques.

The spectroscopic diagnostics were subsequently applied to plasma formed above aluminum targets in an argon atmosphere. The results show that the metal-gas plasma behavior is dominated by the argon species. In the metal-gas plasma, up to 30 percent of the incident laser power is absorbed with a negligible amount of reradiated plasma energy delivered to the target. The dominant effect in the metal-gas plasma appears to be laser refraction which was determined by coupling the experimental results to a target transport model. Sufficient laser energy is transmitted to the target to maintain melting during plasma formation. Since the laser spot is refracted into a larger area, the laser-target interaction time is increased, resulting in a larger heat affected zone. A first order numerical model of the steady-state metal-gas plasma is proposed for eventual coupling to target transport models for a priori determination of the heat affected zone.

TABLE OF CONTENTS

	Page
1. LITERATURE SURVEY.....	1
1.1 Introduction.....	1
1.2 Material Processing.....	2
1.3 Modeling Efforts.....	15
1.4 Laser Propulsion.....	17
2. PLASMA PHYSICS.....	22
2.1 Breakdown Mechanisms and Threshold.....	23
2.2 Bremsstrahlung Absorption.....	26
2.3 Transport Equation.....	30
2.4 Plasma Propagation and Equilibrium.....	36
2.5 Plasmas in Pure Gases.....	42
2.6 Plasmas Formed Above Metallic Targets.....	45
2.7 Energy Transport to the Ambient.....	48
2.8 Local Thermodynamic Equilibrium.....	50
3. EXPERIMENTAL APPARATUS.....	58
3.1 Plasma Initiation and Flow Chamber.....	58
3.2 Plasma Initiation Chamber.....	66
3.3 Spectroscopy.....	70
3.3.1 Review of the Techniques.....	73
3.3.2 Relative Diagnostics.....	77
3.3.3 Spectroscopic Equipment.....	85
3.3.4 Data Acquisition.....	88
3.3.4.1 Instrument Operation.....	92
3.3.5 Data Reduction.....	94
4. EXPERIMENTAL RESULTS.....	110
4.1 Pure Argon Plasmas.....	110
4.1.1 Power Dependence.....	113
4.1.2 Flow Rate Dependence.....	118
4.1.3 Comparison with a Numerical Model.....	123
4.2 Aluminum Targets in Argon Atmospheres.....	126
4.2.1 Comparison of Data Analysis Techniques.....	127
4.2.2 Power Dependence.....	131
4.2.3 Translation Speed Dependence.....	137
4.2.4 Graphite Coated Aluminum Targets.....	140
4.2.5 Effect of Results on Target Transport Model...142	
5. NUMERICAL MODEL.....	145
5.1 Model Formulation.....	145
5.2 Solution Procedure.....	148
5.3 Argon Properties.....	150
5.4 Results: Comparison with Experiment.....	156
6. CONCLUSIONS.....	164
APPENDIX A: Abel Inversion and Code Listing.....	169

APPENDIX B: Plasma Transport Code Listing.....	174
APPENDIX C: Metallic Plasma Model Code Listing.....	176
REFERENCES.....	177



Accession For	
NTIS CRA&I	<input checked="checked" type="checkbox"/>
DTIC TAB	<input type="checkbox"/>
Unannounced	<input type="checkbox"/>
Justification	
By	
Distribution /	
Availability Codes	
Dist	Avail a. d / or Special
A-1	

LIST OF TABLES

	Page
Table 1 Comparison of Global Properties Calculated Using Various Spectroscopic Diagnostics.....	128

LIST OF FIGURES

	Page
Figure 1 Pure Gas Plasma Physics.....	43
Figure 2 Metal-Gas Plasma Physics.....	47
Figure 3 Electron-Heavy Particle Interaction Diagram.....	53
Figure 4 Non-normalized Calculated Electron Energy Distribution.....	57
Figure 5 PIFC and Optical Assembly Schematic.....	59
Figure 6 Optical Beam Delivery Schematic.....	61
Figure 7 Intensity Profile of f/3 PIFC Focal Volume.....	62
Figure 8 PIFC Components [49].....	64
Figure 9 Double Exposure Photo of PIFC and Plasma.....	67
Figure 10 PIC Schematic.....	68
Figure 11 Double Exposure Photo of PIC and Plasma.....	71
Figure 12 Intensity Profile of f/7 Cassegrain Focal Volume used in PIC Experiments.....	72
Figure 13 Pure Argon Spectra: 394 to 774 nm.....	79
Figure 14 Pure Argon Spectra: 394 to 434 nm.....	80
Figure 15 Aluminum and Argon Spectra: 390 to 440 nm.....	81
Figure 16 Line to Continuum Ratio.....	84
Figure 17 Relative ArII Line Ratio.....	86
Figure 18 Optical Multichannel Analyzer (OMA) Schematic.....	87
Figure 19 Plasma Imaging Technique.....	89
Figure 20 Example of a Multitrack Data Set.....	91
Figure 21 Diagram of Abel Inversion Process.....	96
Figure 22 Abel Inversion Code: Flowchart.....	98
Figure 23 Radial Dependent Error Analysis of Abel Inversion.....	101

Figure 24	Example of an Integrated Line Profile.....	103
Figure 25	Transport Code: Flowchart.....	104
Figure 26	Geometry of Beam Refraction in Plasma Volume.....	107
Figure 27	Three-dimensional Temperature Field of a 5.5 kW Pure Argon Plasma, f/2.4, 15 cm/sec.....	111
Figure 28	Two-dimensional Temperature Fields of: (a) 2.4 kW, (b) 4.1 kW, and (c) 5.5 kW Pure Argon Plasmas, f/2.4, 15 cm/sec.....	114
Figure 29	Global Laser Power Absorption as a Function of Laser Power: Pure Argon, f/2.4, 15 cm/sec.....	116
Figure 30	Comparison of Spectroscopically Determined Parameters with Calorimetry and Thermometry Data..	119
Figure 31	Two-dimensional Temperature Fields of: (a) 15 cm/sec, (b) 60 cm/sec, and (c) 120 cm/sec Pure Argon Plasma, f/2.4, 4.1 kW.....	120
Figure 32	Comparisons of 5.5 kW Spectroscopic Data to a Numerical Model (22) at 5 kW as a Function of Flow Velocity: Pure Argon, f/2.4.....	122
Figure 33	Global Laser Power Absorption as a Function of Flow Velocity: Pure Argon, f/2.4.....	124
Figure 34	Comparison of Spatial Extent of Spectroscopic Data and a Numerical Model (22).....	125
Figure 35	Comparison of Typical Radial Temperature Profiles using Various Reduction Techniques.....	129
Figure 36	Three-dimensional Temperature Field of a 5 kW, f/7 Aluminum-Argon Plasma.....	132
Figure 37	Two-dimensional Temperature Field of an Aluminum- Argon Plasma, f/7: (a) 4, (b) 5, and (c) 7 kW....	133
Figure 38	Global Laser Power Absorption as a Function of Laser Power: Aluminum-Argon Plasmas, f/7.....	134
Figure 39	Effect of Beam Refraction on Spot Size at the Target.....	136
Figure 40	Two-dimensional Temperature Field of a 4 kW, f/7 Aluminum-Argon Plasma: (a) 10, (b) 20, and (c) 60 in/min.....	138

Figure 41	Global Laser Power Absorption as a Function of Target Translation Speed: Aluminum-Argon Plasma, f/7.....	139
Figure 42	Comparison of 4 kW, f/7 Temperature Fields: (a) Pure Aluminum and (b) Graphite Coated Aluminum.....	141
Figure 43	Surface Temperature Distribution and Melt-Solid Interface for 5 kW, f/7; With and Without Plasma Effects.....	143
Figure 44	Cylindrical Domain of Metal-Gas Plasma Model.....	146
Figure 45	Metal-Gas Plasma Model Grid.....	149
Figure 46	Electron Number Density for 1.0 atm Argon.....	151
Figure 47	Inverse Bremsstrahlung Absorption Coefficient for 1.0 atm Argon.....	153
Figure 48	Thermal and Radiative Conductivity for 1.0 atm Argon.....	154
Figure 49	Line and Continuum Radiative Losses for 1.0 atm Argon.....	155
Figure 50	Metal-Gas Plasma Model Flow Diagram.....	157
Figure 51	Plasma Model Predictions: Zero Convection, as a Function of Laser Power.....	159
Figure 52	Model Prediction of 5 kW, f/7 Laser Supported Plasma Above an Aluminum Target.....	162
Figure 53	Plasma Model Predictions: Convection with $u = 100$ mm/sec as a Function of Laser Power.....	163

NOMENCLATURE

A	area	(cm ²)
A _{mn}	transition probability	(sec ⁻¹)
c	speed of light	(= 2.997 x 10 ¹⁰ cm/sec)
C _p	specific heat at constant pressure	(J/g-K)
D _ω	frequency dependent optical depth	(cm)
e	electron charge	(= 1.602 x 10 ⁻¹⁹ C)
E _a	ablation energy	(W/cm ³)
E _m	energy of level m	(eV, cm ⁻¹ , K)
E _{max}	maximum electron energy	(eV)
E ₀	E-field amplitude	(V/cm)
E _∞	ionization potential	(eV, cm ⁻¹ , K)
f	distribution function	(1/eV)
g _m	degeneracy of state m	-
g	average Gaunt factor	-
h	Plancks constant	(= 6.626 x 10 ⁻³⁴ J-S)
H	enthalpy	(J/g)
I	laser intensity	(W/cm ²)
I _m	minimum impulse	(dyne - sec)
I _{opt}	optimal laser intensity	(W/cm ²)
I _{th}	threshold laser intensity	(W/cm ²)
j _ω	frequency dependent emission coefficient	(W/cm ³)
k	Boltzmann constant	(= 1.38 x 10 ⁻²³ J/K)
K	thermal conductivity	(W/cm-K)
K _a	radiative conductivity	(W/cm-K)
ℓ	characteristic plasma length	(cm)

m_a	atomic mass	(g)
m_e	electron mass	(= $9.109 \times 10^{-28}g$)
n	index of refraction	-
N_e	electron number density	(cm^{-3})
N_i	ion number density	(cm^{-3})
N_o	atomic number density	(cm^{-3})
p	pressure	(atm)
P	laser power	(W)
P_r	radiative loss	(W/cm ³)
$\langle q \rangle$	momentum transfer cross-section	(cm ²)
r	radial position	(cm)
S_ω	frequency dependent source function	(W/cm ²)
t	thickness	(cm)
T_e	electron temperature	(K)
T_g	heavy particle temperature	(K)
V_e	electron quivering speed	(cm/sec)
V_T	electron thermal speed	(cm/sec)
y	line-of-sight position	(cm)
z	axial position	(cm)
Z	ion charge number	-
Z_e	electron partition function	-

α	inverse bremsstrahlung absorption coefficient	(cm^{-1})
n	field strength parameter	-
ϵ	emission coefficient	($\text{W}/\text{cm}^3 \text{ -sr}$)
λ	wavelength	(nm)
ν	laser frequency	(sec^{-1})
ν_m	electron-atom elastic collision frequency	(sec^{-1})
ω	laser frequency	(rad/sec)
ω_p	plasma frequency	(sec^{-1})
ρ	density	(g/cm^3)
ζ	non-hydrogenic correction term	-

1. LITERATURE SURVEY

1.1 Introduction

The most widespread commercial use of the laser is in cutting, welding, drilling, and heat treatment. Many applications involve lasers of sufficient power (intensity) such that a laser induced plasma can form. The plasma is defined as the collection of vaporized material and ambient species which are excited to a high enough energy state such that the gases can interact, via absorption, with the laser energy. A review of the literature will demonstrate that the plasma effects are generally circumvented by mechanical means. With the advent of high peak power pulsed lasers (in excess of 10J per pulse) and CW lasers in excess of 1kW, research has focused on the quantitative measurement of laser-plasma-target interaction. The above efforts have been primarily interested in measurement of "enhanced coupling" phenomena at fluxes greater than 10^8W/cm^2 . Enhanced coupling is the effect where more laser energy has apparently coupled to the target than can be explained via simple radiation absorptivity and thermal conductivity.

Along with the experimental work several models of plasma initiation and maintenance were developed. As laser powers increased most of the studies evolved into the areas of fusion and damage. Most of the work was subsequently classified about 1982. Some of the studies were concerned with laser propulsion which received a renewed interest in the early 1980's. From this work, a general understanding of plasma phenomena can be developed. The goal of this effort is to parameterize laser-plasma-target interactions in the sub- 10^7W/cm^2 intensity range and utilize the results to accurately predict heat affected zones (HAZ) in targets.

1.2 Material Processing

One of the earliest experimental studies of laser coupling to targets was presented by Locke, et al. [1]. The authors were concerned with the non-uniform penetration depths in laser welding. Half inch thick 304 stainless steel plates were welded at CW laser powers from 8 to 20 kW, f/8 optics, 1.00mm spot diameter. The results indicated that the edge fit had to be less than 1/10 the thickness for a successful weld. The authors were interested in efficiency of the laser process and defined an arbitrary value of 30%. The efficiency was defined as the ratio of the actual coupled power to the power needed for a hypothetical case of zero conduction. The results indicated efficiencies of 22 to 45 percent for laser powers of 3.8 and 20kW, respectively. The values represented a slight improvement over E-beam welding which increased with increasing power. Finally, a qualitative study of gas assists was made. A gas assist with a component normal to the target surface resulted in a deeper, less uniform penetration. A transverse gas assist was seen to develop a "more luminous... concentrated ionization cloud", but most of the laser energy appeared to be transmitted to the target. The transverse gas assist resulted in a uniform weld. With no gas assist, the plasma was reported to shield most of the laser energy.

Pirri, et al. [2] investigated the momentum transfer to a target when irradiated by a pulsed CO₂ laser, peak flux of 3 to 6x10⁸W/cm², 25 μs pulse. The results of ballistic pendulum measurements indicated that momentum decreases with increasing pulse energy. The effect was

independent of material for carbon, aluminum, and tungsten. The impulse also increased with target area. This result led to the hypothesis that the momentum transfer was due to a surface expansion wave and that the plasma must therefore be radiatively driven. Pirri assumed all of the laser energy was deposited in a point above the target, forming the center of a blast wave. Blast theory was then applied to show that the maximum momentum transfer occurs if the target is large enough for the blast wave to equilibrate prior to expansion off the target. A video system was used to monitor the expansion velocity at a few microseconds into the laser pulse. The expansion velocity was approximately 60 percent below the predicted blast wave velocity of 1.8×10^6 cm/s. By increasing the spot size, the authors bounded a transition between combustion-type and detonation-type waves to be 10^7 to 4×10^8 W/cm², which is close to the classical detonation value. At 10^7 W/cm² most of the laser energy was assumed to be absorbed into a thin surface plasma, but this was a consequence of the observed plasma shielding at higher fluxes. A detailed treatment of combustion and detonation phenomena is presented in Chap. 2.

Lowder, et al. [3] investigated target interaction with a pulsed CO₂ laser. The pulse shape consisted of a 1 μ s spike followed by a lower plateau of 10-30 μ s. The authors were one of the first to admit that the experimental spot size was not diffraction limited. Using streak photography the expansion velocity was measured to be 10^5 to 10^6 cm/s and constantly decreasing, implying combustion wave phenomena. The camera results indicated that laser absorption occurred throughout the plasma volume and the blast wave calculations accounted for the long

absorption length. The conclusion, as in Pirri's work [2], was that the combustion to detonation transition occurred at an intensity of 4×10^7 W/cm² (± 25 percent) for a beam radius of 0.2 to 0.3 cm. Using an electrostatic probe, the authors found that the air instantly photoionizes from the breakdown radiation and that the ionized air expands more slowly than the blast wave. From the absorption length measured from the streak camera, the blast wave energy was found to be of an equal magnitude to the laser energy in the detonation regime. The impulse was again found to be independent of material and due primarily to the high pressure gas volume formed at the surface.

Fowler and Smith [4] reported the use of a 6kW CW CO₂ laser in a study of plasma initiation on metal targets. High speed photography showed that nearly complete decoupling of the laser radiation occurred as the plasma expanded into the 6kW, f/7 beam. The results also indicated that the initiation in air occurred analogously to an arc breakdown and that the plasmas extinguished at f/10 and higher. At lower f/#s where the plasma could be maintained, a calorimeter was placed behind a small hole in the target. Calorimetry indicated that approximately 50 percent of the laser radiation was transmitted by the plasma. Combined with the photographic studies, a volume averaged absorption coefficient was calculated which inferred an average plasma electron temperature of 14,000 K. Minimum plasma maintenance power was less than 2kW ($d = .07$ mm) which agreed with predicted values.

The paper also reports on the threshold intensity of various materials. For spot sizes less than 0.3mm diameter, the threshold was material independent. At spot sizes in excess of 1mm diameter, the

carbon threshold was slightly higher than aluminum, a result that appears to be counterintuitive but no explanation was given. Transverse gas assists had little effect on initiation for spot sizes smaller than .5mm diameter. At larger spot sizes, the transverse gas assist monotonically increased the threshold with spot size, between 25 and 200 percent. The effort also utilized a two wavelength interferometer to measure the electron number density in the air plasma. The calculated number densities were sufficient to suspect refraction or blooming was an effect on the delivered intensity to the target. A detector behind a hole in the target measured the energy during plasma formation. The results showed that as much as 90 percent attenuation occurred which disagrees with the 50 percent value from calorimetry. The conclusion was that blooming indeed further reduced the intensity and altered the spatial distribution of energy deliverable to the target. This conclusion thus contradicts some of the previous effort's conclusions as the various diagnostic techniques did not necessarily account for blooming.

Engel [5] reported the status of CO₂ laser cutting of thin materials with a 1kW TEM₀₀ laser with intensities on the order of 10⁸W/cm². An empirical result was that optimal cutting (minimum kerf width and lateral damage) occurred when the laser focus was located 1/3 the material thickness below the surface. In metals, Engel concluded that surface finish and oxides had little effect on cutting rates. The report provides one of the first empirical relationships for cutting rate:

$$\text{Rate (cm/sec)} = KP/(E_a At) \quad (1.1)$$

where K is an empirical constant (cm/sec), P is the laser power (W), E_a is the ablation energy (W/cm^3), A is the spot area (cm^2), and t the material thickness (cm). Engel also investigated the use of assist gases. The use of oxygen increased cutting rates by 40 percent over inert gases. The effect was attributed to exothermic reactions which aided material removal. For non-metals, the cutting rates demonstrated were as much as two orders of magnitude greater than conventional techniques for quartz. The laser was also shown to improve the cut quality in difficult to machine materials such as Kevlar and the lack of tool wear made these processes competitive.

Robin and Nordin [6] investigated the possibility of improving penetration depths by tailoring the laser energy profile. It was noted that the laser energy mainly went into the heat of vaporization once a melt formed. Mechanical means had been used to remove the melt and maximize the solid/liquid propagation velocity. From the momentum transfer work cited previously, the authors proposed that the impulse delivered by a pulsed laser could be used to drive the melt out of the kerf during CW cutting. The melt was assumed to escape via the pulsed laser impulse in a hollow cylindrical column around the CW focus geometry. The melt mass removal was assumed total and the rate was integrated to determine pulse duration and thus the impulse required. The minimum impulse, I_m , was calculated to be [6]:

$$I_m = 1/2 k_p A (R/S) (1-\beta). \quad (1.2)$$

Where k is the thermal conductivity, A is the spot area ($=\pi R^2$), ρ is the melt density, S is the cylindrical ejection path wall thickness, and $\beta(=k/[k + V_0 h])$ is a measure of the percentage of the maximum solid/melt interface velocity. The approximation is valid for most metals where β is 25 percent below unity for a given melt thickness, h . The result for aluminum was that an impulse of 2 dyne-sec or a microsecond pulse at 10^8 to 10^9 W/cm^2 (20-100 dyne-sec) would be sufficient for a substantial improvement in cutting rates. A reference to an experimental paper showed that the applied impulse was sufficient to open a hole in a thin target which remained closed in the case of no superimposed pulse. Other experiments also indicated a doubling of cutting rates when a small pressure difference was maintained across a thin target.

Duley's classical text [7] on carbon dioxide lasers in 1976 marked the first encompassing treatment of practical laser systems. The text covers laser physics, heating, drilling, welding, diagnostics, and communication aspects of CO_2 lasers. Plasma formation is treated qualitatively in the various applications. It was noted that a laser supported combustion wave (LSC) could completely shield a workpiece from $10.6 \mu\text{m}$ radiation. It was further noted that plasma effects were adequately circumvented through mechanical means. The author suggests the use of a pulsed laser system with a pulse separation long enough to allow the plasma to extinguish. No report of experimental verification was made. The suggestion will be shown to be limited as several subsequent investigations demonstrate plasma formation to be desirable.

Metal drilling processes were treated by von Allmen, et al. [8]. A pulsed Nd-YAG laser was utilized and the decrease in material reflectance with temperature was measured. The change in reflectance was attributed to the metal-dielectric transition during melting and the formation of a stationary plasma layer at the surface. The sample was placed in one focus of an ellipsoid and the detector placed in the other. Three phases of reflectivity were monitored. First, the reflected signal remained constant until the melt began to form. Second, a fast decrease in reflectivity occurred which was inversely proportional to laser intensity. The final range was a constant low value with a slight decrease as the interaction zone increased, i.e., drilling effects became significant. The reflectivity recovers to nominal in 10 to 20 nanoseconds after the laser pulse, depending on target damage.

At times in excess of 720 nanoseconds, the authors noted the beginning of an explosion-like event and development of a surface absorption layer. From the reflectivity data the radial expansion velocity was determined to be 10^4 cm/s. Enhanced coupling (reduced reflectivity) was always noted upon the initiation of a plasma. When the mass removed was compared with previous drilling models, the results indicated that 70 to 80 percent coupling occurred which agreed with the reflected signals. The transition temperature for reduced reflectivity was determined to be a few hundred degrees above the vaporization temperature for Cu, Al, Ni, and Fe. The authors concluded from the plasma volume that conduction was the primary transport mechanism between the plasma and target as a surface temperature conduction model

adequately explained the experimental results. From the conduction model it was determined that the plasma formation corresponds to a relatively low evaporation pressure of 3 to 10 atmospheres. This range is significantly below the ablation pressures proposed by other authors which are on the order of one hundred atmospheres.

McKay and Schriempf [9] proposed a thermal transient analysis of the heating profiles of thin targets as a method of measuring an effective coupling coefficient. The authors used a 5 μ s pulsed CO_2 laser with a maximum pulse energy of 140J. The analysis was considered for pulse times and target sizes such that lateral heat flow was negligible compared to the normal component. With this assumption, the target thermal response could be modeled via Laplace transforms which depended on the material properties and beam parameters. The thermal response was measured at two locations, one on focus center and the second off axis. The two responses could then be applied to adjust the thermal response model parameters to effective values. At low fluences where no plasma formed, the effective fluence deposition and hence absorbtivity could be determined. The thermal response agrees very well until late in the profile (greater than a few seconds) when the finite size of the target made the modeling assumptions invalid. When a plasma was formed, both the fluences and beam area had to be adjusted to fit the thermal responses. The conclusion was that plasma spreading and beam blooming were considerable effects. One should note, however, that the thermal lag of the thermocouples was apparently not considered, an effect that would be very critical when transient slope matching is the basis of the diagnostic tool.

McKay, et al. [11] continued the pulsed interaction studies with the implementation of other diagnostics. Care was taken to renew the surface of Al targets between shots by abrasion. The result was that 4 micrometer dig and 1 micrometer Al particles were left after abrasion. The authors admit the criticality of the "defect" heating in initiation, but were more interested in comparison of the results from a separate investigation. Walters, et al. [11] had proposed the defect heating theory of plasma initiation in an attempt to explain the variation in reported threshold intensities from author to author. The theory is generally accepted but being stochastic is difficult to verify or model.

The results of McKay's effort [10] was that the effective spot radius increased 50% as discussed in Ref. 9. Below the plasma threshold the absorptivity of Al was 9 percent and jumped to 18 percent upon plasma initiation. Spectroscopic studies of the gas volume near the target surface revealed that the unabraded surfaces spectra were dominated by the ambient air N and O. For the abraded surfaces N and Al dominated the spectra which may imply the removal of oxides. The time averaged temperature for the Al^+ to Al^{++} ratio was 12,000 K compared to 16,000 K for a nitrogen line pair. The discrepancy was attributed to the target lines appearing after the ambient plasma formation when cooling processes within the plasma have begun. Interferometric measurements showed the electron number density to be 10^{18}cm^{-3} and the blast wave expansion velocity on the order of 10^5cm/s .

The authors concluded from a simple analysis that a blackbody plasma at 16,000 K, $\lambda_{\text{max}} = 220 \text{ nm}$, and a target absorptivity of 40 percent, could not sufficiently explain the enhanced coupling as measured. The 33% discrepancy had to be made up by conduction which is possibly the dominant effect. The conclusion was that the HAZ doubled at threshold intensities and increased up to nine times the area at peak powers.

Maher and Hall [12] were also interested in pulse tailoring. The authors noted that the thermal profile radius increased with increasing pulse energy but did not elaborate if the energy was in the pulse spike or in the tail region. From previous experiments, the authors concluded that optimal laser coupling occurs when a plasma forms near the surface. For this case, the primary transport mechanism was assumed to be UV radiation from the plasma. Thus a pulse with an initial spike (1 μs) to initiate the plasma followed by a lower power ($5 \times 10^5 \text{ W/cm}^2$) plateau to maintain the plasma should result in optimal coupling. The results indicated that no optimal pulse shape could be found in direct contrast to the results of Ref. [10]. The authors also looked at the production of Al lines during the plasma formation. The increasing strength of Al in the plasma/volume with increasing laser power was interpreted as an increased amount of laser energy going into vaporization and hence a higher plasma absorption.

Carlhoff, et al. [13] investigated continuous optical discharges in pure gases at very high pressures (1-210 bars). The experiments involved a 2kW CW CO_2 laser with intensities in the range of 10^6 to 10^7 W/cm^2 . Spectroscopy of Ar and He continuum and a Mach-Zender

interferometer in the finite fringe mode were used to characterize the plasma electron parameters. The qualitative results indicated that the peak temperature volumes lie upstream from the laser focus. Maintenance power increased with pressure for low $f/\#$ systems and decreased for high $f/\#$ systems. The plasmas were stable with He being more stable than Ar at pressures above 100 bar. The effort demonstrated that high pressure plasmas could be maintained relatively easily in contrast to the then current theory. No further investigation was presented and the direction of the research was not clear.

Rosen, et al. [14] investigated the coupling of ultraviolet laser radiation (XeCl at $.35 \mu\text{m}$) to aluminum targets in vacuum. A model of the plasma was developed, including the effects of photoionization. Other mechanisms found to be important were the ionization of excited aluminum and the elastic collisional deexcitation leading to a temperature difference between the electrons and heavy particles. The model results indicate that the aluminum number density drops in 10^{-6} seconds and in the case of an ambient gas presence, inverse bremsstrahlung absorption would be governed by the non-aluminum species. The model agreed with the measured initiation intensity of pulse durations of 10^{-7} to 10^{-6} sec, demonstrating photoionization being important at UV laser wavelengths. For 2024 Al the as received coupling coefficient was determined to be 0.4 and ground and polished 2024Al was seen to be 0.2. For 99.999 percent pure Al, the coupling coefficient was 0.08 to 0.11 over the range of 20 to 5 J/cm^2 . The plasma threshold was measured to be in excess of $6 \times 10^7 \text{W}/\text{cm}^2$ and decreased with increasing pulse duration, as predicted by the model.

At this point in time, late 1981, much of the American literature was classified or had been redirected into the area of laser fusion. Several non-American efforts were made and new groups began to investigate the concept of laser propulsion.

One of the foreign efforts, and now one of the leading institutes of industrial laser-target interaction was presented by Miyamoto, et al. [15] from Osaka University. This paper attempted to quantify the role of the gas assist in laser welding noting the poor reproducibility. Several gas assist parameters were investigated beginning with nozzle angle of attack. It was noted that the penetration depth increased with increasing nozzle angle (increasing component normal to target surface). The effect saturated at approximately 30 degrees and subsequent experiments were performed at 40 degrees. Three regimes of pressure dependence were found. First, the plasma bead regime at low gas pressure was found to result in a shallow bead deemed unacceptable. In the second regime (sub-atmospheric pressure) a sound and uniform bead resulted with an increased penetration depth. The third range resulted in the bead being blown off the weld and large porosities were formed during solidification. A smaller nozzle diameter and placing the nozzle closer to the surface resulted in a larger operational range (second regime). The cavity in region two was located at the leading edge of the pool and periodic changes in cavity shape led to eddy behavior in the molten flow behind.

The effect of using a gas with a higher ionization potential was an increase in penetration depth for the case of zero dynamic pressure exerted on melt pool. Eventually, pressure overwhelmed the ionization

potential effects at pressures above half an atmosphere. The effort also demonstrated the use of phototransistors for the monitoring of the weld regime. Conclusions were that suppression of plasma formation was critical and at low speeds, vacuum welding was preferable.

Another text, edited by Bass [16], treats laser material processing on a more general level. The various applications of welding, cutting, etc. are treated individually, to some extent comparing the use of different lasers. Again, however, the plasma formation is treated on a semi-quantitative basis. In the chapter on laser cutting by Steen and Kamalu, efficient nozzle design is noted as a prerequisite. The authors discuss the effects of shock wave formation from the nozzle exhaust resulting in poor cut quality. Little or no reference of plasma formation other than intermittent plasma formation may further degrade cut quality. Only now have studies begun to investigate the gas dynamic effects of shocks on target transport. Also in Bass, the chapter by Mazumder on laser welding reports qualitatively on scattering and absorption of laser radiation as the beam propagates through a plasma volume. Effective assist gas systems were shown to be capable of circumventing the problem. It was further suggested that a shield gas with a higher ionization potential would serve to inhibit plasma formation, as was indicated in several experimental efforts.

Another effort on CW CO₂ material processing was presented by Donati, et al. [17]. The experiments involved the use of a 15kW CO₂ laser, with an f/7 telescope resulting in a focus spot diameter of 0.7mm. High speed photography and CO₂ laser transmission experiments were used to monitor plasma formation. The transmission experiments

indicated that plasma formation was intermittent, appearing to extinguish and re-form in response to temporal laser and gas fluctuations. From the authors data, the plasma appears to decouple from the target at a frequency between 300 and 4000 Hz. However, the CW interaction times may have been relatively short (less than 1 sec) and the transmission data appears to approach a DC value near the end of the interaction time. The effect of the plasma coupling data was not evident in the absorbed energy measurements. If the plasma is indeed decoupling, it is doing so at a relatively high, random frequency with the net target effects being the result of a smooth integrated effect.

1.2 Modeling Efforts

During the course of the previously cited experimental efforts, several attempts were made to model initiation and plasma propagation. Most of these efforts expanded upon the early work of Raizer, whose classical treatment of blast wave theory will be treated in Chap. 2.

Wu and Pirri [18] treated the breakdown of contaminated air at intensities from 10^6 to 10^7 W/cm^2 at $10.6 \mu\text{m}$. The process was modeled in three temporal stages. First, heating and vaporization of the contaminant material in air. The contaminant material was necessary for absorption to occur at room temperature and pressure. Second, the absorbed energy is transferred to the surrounding air and finally an air plasma bubble forms. To obtain a solution, several assumptions regarding vaporization of the contaminants were made and a perturbation analysis of the energy and propagation equations were solved. As the plasma expands at later times, a snowplow model was developed in which

the plasma front pushes away the ambient air. Any mass transfer across the front was assumed to immediately equilibrate with the higher pressure plasma volume. The results indicated that plasma formation is nearly complete in 45 μ s which agreed with an experimental effort. The plasma peak temperature rose and stabilized at 17,800 K after about 1 μ s, and peak temperatures rose with increasing intensity. Finally, plasma growth rate (volumetric) increased with increasing intensity for both the early stage and snowplow models.

More recently, Muller and Uhlenbusch [19] developed a model for continuous optical discharges in conjunction with Ref. [13]. The paper considers two-dimensional heat flux, one dimensional imposed flow field with a constant mass flow rate. The beam absorption of a focused Gaussian profile was also taken into account. The authors made the simplification of C_p/K is constant, which is not valid at these temperatures, and also utilized a volume averaged absorption coefficient. Even with the questionable assumptions, the results showed reasonable agreement with the measured temperature fields of Ref. [13] at 5 bar argon. The results indicated a weak dependence on focused beam quality and a stronger dependence on flow velocity.

The brief treatment of the early models is somewhat warranted. Almost all the models made various simplifying assumptions in order to obtain analytical solutions. In the late 1970's, interest was renewed in the concept of laser propulsion. With the experimental work came several numerical models which incorporated real gas properties and more recently full two-dimensional analysis. The literature survey is completed by a review of the field of laser propulsion.

1.3 Laser Propulsion

Many of the works on pulsed laser interaction and momentum transfer evolved into the study of laser propulsion. A separate group of investigators began to experimentally study continuous wave laser propulsion in the early 1980's. The concept is that a remote laser source, either satellite or ground based, be directed and focused into an absorption chamber onboard a payload. Direct heating of the propellant occurs upon plasma formation and the hot gas subsequently expanded, converting thermal energy to kinetic energy or thrust. The relatively simple absorption chamber eliminates much of the mass involved in classical combustion processes. Since no combustion is involved, low molecular weight propellants can be used, further reducing propulsion mass. The net effect is that moderate thrust levels at high specific impulses are feasible. The current application appears to be low-earth to geosynchronous orbital transfer. A comprehensive review of the history and status of laser propulsion was made by Glumb and Krier [20].

Part of the research to be discussed in this study and in Ref. [21] deals with the use of a 10kW CW CO₂ laser (f/2.4-3.4) for initiation and maintenance of atmospheric pressure argon plasmas at low flow rates. The results indicated that the plasma volume grew with increasing power resulting in a net absorption of 80 percent of the incident laser power at 7kW. The absorbed power was measured via a copper cone calorimeter which intercepted the transmitted laser beam. Thermocouple measurements of the downstream temperature profiles were used to calculate the net

power retained by the gas as thermal energy. The results indicated that thermal efficiencies in excess of 25 percent were obtained. The trend of the absorption and efficiency curves were corroborated by results calculated from the spectroscopically measured temperature fields at the corresponding laser powers.

The impact of this study and similar research at the University of Tennessee Space Institute which will be discussed subsequently, were that plasma initiation, an early concern, was in fact routine. Both studies utilize metallic targets injected into the focal region to lower the breakdown intensity by the creation of the first free electrons. The electron densities created in this manner have been found to be sufficient for cascade breakdown in the ambient gas to occur. A second early concern was the ability to stabilize a plasma in the systems which has again proven to be routine. The two efforts are in the process of mapping larger ranges of flow and pressure parameters to attain thermal efficiencies up to 50 percent where laser propulsion appears feasible. The University of Illinois is also looking at more classical means of improving efficiency such as regenerative preheating of the propellant and multiple plasma formation to minimize radiative view factors to chamber walls.

A simultaneous modeling effort was begun at the University of Illinois by Glumb and Krier [22]. The model is numerical with a one-dimensional flow field with two-dimensional heat transfer. The converging beam geometry and real gas properties for argon incorporated in that model were at the time unique. The results agreed with the experimental results of Ref. [21], and continue to do so. The model has

been used to look at more realistic powers and pressures in an attempt to develop scaling laws for full-scale propulsion systems. More importantly, the model has been used to direct the current experimental work in the investigation of regions of optimal thermal efficiencies within the physical limitations of the current laboratory facilities.

Welle, Keefer, and Peters [23] recently reported the Tennessee effort at lower laser powers (sub-kW) but higher flow rates (.4 to 4.5 m/s). Earlier results demonstrated similar trends as the U of I effort but particular importance was placed on beam geometry. The latest results indicate a lesser dependence on beam geometry versus flow rate as noted in Ref. [19]. All of the Tennessee data has been calculated from the continuum emission of argon at 626.5nm, with no independent diagnostic technique having been reported to date. The results appear reasonable with peak temperatures in excess of 15,000 K and thermal efficiencies approaching 40 percent. The increase in thermal efficiency is as expected due to the smaller volume and generally cooler plasma formed at the higher flow rates, resulting in smaller radiative losses. The study also notes that the experimental error, assumed to be $\pm 10\%$, resulted in a net difference of the global properties of absorption and radiative losses of a few percent, as will be shown in this effort.

The University of Tennessee has recently presented the results of a numerical modeling effort by Jeng and Keefer [24]. The model currently incorporates laminar, incompressible Navier Stokes equations in two-dimensions and geometric ray tracing of the converging/diverging laser beam, as well as real gas properties. The model agrees well with

experimental flowing argon temperature fields for static pressures in excess of two atmospheres. The model was compared with the results of a quasi two-dimensional model similar to that developed in Ref. [22]. The results indicated that the optically thick radiation at pressures below two atmospheres was not accurately modeled by the diffusion approximation. Apparently by trial and error, it was found that by using 50 percent of the radiative conductivity, agreement between the model and experiment was satisfactory. Assessment of the solution procedure remains to be performed as well as the applicability of the radiative conductivity criteria in the quasi two-dimensional models. The model is currently being reworked to account for beam diffraction and refraction in an attempt to clear up some minor discrepancies. A useful outcome of this model may be the ability to impress a more realistic flow field onto the quasi two-dimensional model grid. The predicted effects are that the radial component is small compared to the axial velocity. However, the axial velocity approaches zero at the centerline near the peak temperature contour and local variations in the radial velocity may be significant.

It has been demonstrated that a considerable effort has been devoted to laser-plasma-target interaction. The results of various authors have varied significantly in threshold values, optimizing laser parameters and dominant transport mechanisms. The regime of CW laser interaction in industrial applications has been largely ignored except for some quantitative studies of optimal gas assist configurations. Many of the efforts that quantitatively defined experimental plasma parameters did not calculate transport phenomena. Due to these

discrepancies and the availability of accurate material transport codes [25,26] this investigation proposes to experimentally monitor plasma parameters and perform the subsequent plasma-target transport calculations. The goal of this effort is complete a priori determination of nominal laser parameters required to effect a given material transformation.

2. PLASMA PHYSICS

When a laser of sufficient energy is focused into a gaseous medium (10^9W/cm^2) or onto a solid target (10^5W/cm^2), a plasma will form. The plasma is a collection of particles which can range from a few percent to complete ionization. In this investigation, the concern is for low temperature plasmas where the particle temperatures range from 5,000 to 20,000 K. The plasmas formed are at or near atmospheric pressures which imply equilibrium number densities on the order of 10^{16} to 10^{17} cm^{-3} for the heavy particles and electrons [27].

In this chapter, the physics of low temperature plasmas is discussed. Although the study is of steady state CW plasma formation, a discussion of the initiation and breakdown mechanisms is warranted and is presented first. Next, the mechanisms of laser energy transport within the plasma volume are discussed. The transport equation is developed with emphasis on the radiative properties of the plasma. The propagation of the plasma into a converging laser beam is discussed with respect to the instabilities associated with the steady state plasma volume. Since the effort is concerned with both pure gas and gas/metal vapor plasmas, these two cases are treated separately. The conduction, convection, and radiative transport to the ambient is discussed next. Finally, the concept of local thermodynamic equilibrium (LTE) is treated. LTE is the fundamental assumption made throughout the study, without which plasma characterization becomes unwieldy.

2.1 Breakdown Mechanisms and Threshold

Two mechanisms contribute to the initiation of a plasma. First, on the basis of quantum mechanics, there is a finite probability of multiphoton absorption by a bound electron. The absorbed photon energy would be sufficient to ionize the atom, freeing the initial electron "seed". The second mechanism is cascade or avalanche breakdown. In this case, it is assumed that the initial free electron is available for photon absorption in the presence of an atom or ion. The process is called inverse bremsstrahlung absorption and is inversely analogous to "brake radiation" emission of a photon by the heavy particle in the presence of an electron.

Multiphoton absorption probability can be shown to be low, especially at 10.6 micrometer radiation. For example, the ionization potential of argon is 15.8eV and the energy of a 10.6 micrometer photon is 0.124eV. Thus, 128 photons need to be absorbed simultaneously at this wavelength, neglecting loss mechanisms, for ionization to occur in the cold gas. Experiments have shown that multiphoton absorption is indeed negligible, especially at pressures near atmospheric.

In avalanche breakdown, the first free electron, or, more exactly, a large number of free electrons are necessary to initiate the plasma and overcome loss mechanisms. In the ideal case, the electron oscillates with the electromagnetic field in the laser focal volume. The electron transfers kinetic energy to the atoms leading to an increased amount of energy in the random motion of the heavy particles. The random motion enhances the effective cross-section of the atom which facilitates inverse bremsstrahlung (IB) absorption. The

net result is that the average electron energy remains the same. However, if the intensity of the laser is sufficient to overcome the loss mechanisms, the electron will eventually acquire enough energy to ionize an atom during collision. The process results in two slow electrons which continue the process and hence the avalanche phenomena.

The loss mechanisms consist of electron diffusion, recombination, and both elastic and inelastic collisions. Electron diffusion is where the electron moves out of the focal volume prior to sufficient energy absorption for ionization. For the relatively large focal volume dimensions with respect to the electron mean free path at atmospheric pressures, macroscopic diffusion losses can be shown to be minimal. At the high optical frequencies in this investigation, the electron diffusion is further restricted by the oscillating field reversal. Discrepancies in threshold measurements indicate that diffusion may be a factor. Zeldovich and Raizer [28] hypothesize that local "hot spots" in the focal volume due to diffraction and aberrations are the sources of avalanche. These volumes are small compared to the focal volume and may depend heavily on electron diffusion. However, the stochastic nature of the isophotes due to laser mode changes make the hypothesis difficult to verify or model.

Recombination is a highly probable process, especially in gases at room temperature. The elastic collisions can be modeled as hard sphere interactions in which the electron gives up the mass ratio, m_e/m_a , energy per collision, where m_a and m_e are the atom and electron masses, respectively. The inelastic collisions only become important as the

electron energy approaches the ionization potential. The electron transfers energy to excite the atom. The higher energy criteria is due to the relatively large energies associated with the first excited states of inert gases. In argon, for example, the first level is roughly 75 percent of the ionization potential.

The result of the above absorption and loss mechanisms is that there is a threshold effect. The effect has been noted since the early studies of arc plasmas. From the net rate of increase in electron energy of a cold gas, taking into account elastic collisions, the maximum electron energy can be expressed classically as:

$$E_{\max}(\text{eV}) = 5.8 \times 10^{20} AI(\text{W/cm}^2)/(\omega + \nu_m^2) \quad (2.1)$$

where E_{\max} is the maximum energy, A is the atomic weight, I the laser intensity, ω the laser frequency (rad/sec), and ν_m the effective elastic collision frequency. Therefore, for ionization to begin, E_{\max} must exceed the ionization potential. For example, argon at atmospheric pressure, CO_2 laser radiation, and assuming an initial electron density of 10^{11}cm^{-3} , Eqn. (2.1) shows that the required laser intensity is 10^9W/cm^2 . In most "clean" gases, the 10^{11}cm^{-3} is a number which comes from pre-ionization via arc discharge, otherwise the IB process does not occur at any laser intensity.

It is seen in Eqn. (2.1) that the threshold intensity (I_{th}) is proportional to the elastic collision frequency and hence pressure. As is expected, I_{th} decreases with increasing pressure (number density) which increases the collision frequency. Other parameters play a role

in the threshold effect. First, the threshold increases with ionization potential as expected. An unexpected effect is the threshold peak in the visible spectrum as one were to change the laser frequency from UV to IR. Again from Eqn. (2.1), one expects the threshold lowering in the infrared, as ω is decreasing. However, experiments have shown an increase in the threshold in the IR. The IR values are too low for multiphoton absorption to be a factor, but no definitive theory currently exists.

Another factor, as mentioned before, is the focal volume in the case where electron diffusion may be a factor. At atmospheric pressures, where this study's interests lie, the effect is negligible. The effects of pulse duration are not a major concern in this investigation, since CW radiation is utilized. There are indications of threshold lowering with increasing pulse duration. The lowering is marginal and was concluded by comparing the results of several authors under varying conditions. It should be noted that other efforts have reported no dependence on pulse duration, only on pulse power.

2.2 Bremsstrahlung Absorption

Inverse bremsstrahlung (IB) absorption is the basic mechanism of power absorption within the plasma volume. The absorption coefficient can be derived via classical or quantum theory. The main difference in the two results is that the quantum derivation maintains separate terms accounting for IB absorption and losses due to stimulated emission at the laser frequency. The classical derivation is a net calculation and the individual terms are lost in the final form.

The IB absorption coefficient was first derived by Kramers [29] in 1923. Kramers used classical theory in the derivation of the bremsstrahlung emission coefficient. The author then applied the quantum theory of detailed balancing to arrive at the IB absorption coefficient which is of the form:

$$\alpha(\text{m}^{-1}) = \frac{4}{3} \frac{2\pi e^6 Z N_i N_e}{\sqrt{6\pi} k m_e^3} \frac{\lambda^3}{hc^4 T_e^2} \quad (2.2)$$

where N_i is the ion density, N_e the electron density, and Z the ion charge. The derivation was hydrogenic and was based on calculations that line emission energy offset continuum reductions of the actual hydrogen spectrum compared to Planck's blackbody radiation relation.

Equation (2.2) represents the electron-ion coefficient. The electron-atom coefficient plays a role at lower electron temperatures near 10,000 K. As the ionization exceeds a few percent, the long range ion Coulomb interactions overwhelm the relatively short range atomic cross-sections. Several authors have attempted to account for atom-ion IB, non-hydrogenic behavior of certain gases and stimulated emission by developing effective coefficients. Notably, Wheeler [30] made corrections for argon. To account for stimulated emission, Wheeler showed that the net effect was a reduction of α by a factor of $[1 - \text{Exp}(-h\nu/kT_e)]$, where ν is the laser frequency. To account for non-hydrogenic behavior, the free-free Gaunt factor (g_{ff}) multiplies Eqn. (2.2) as well as the effective charge, \bar{Z} . A corrected "effective" Gaunt factor was proposed by Stallcop [31]. The first correction of g_{ff} was to account for electron-atom IB. Secondly, a term, $h\nu/kT_e$, was

added to g_{ff} to account for photoionization effects. Although photoionization was shown to be negligible at 10.6 micrometers during initiation, the effects increase to a non-negligible value when excited species are present. The result is an effective inverse bremsstrahlung absorption coefficient:

$$\alpha(m^{-1}) = \frac{4}{3} \frac{2\pi e^6 \bar{Z}}{6\pi k m_e^3} \frac{N_e^2 \lambda^3}{hc^4 T_e^2} [1 - \exp(-h\nu/kT_e)] (g_{ff} + \frac{h\nu}{kT_e}) \quad (2.3)$$

This absorption coefficient has been successfully used in a numerical model [22] for atmospheric laser supported plasmas in pure flowing argon.

Loss mechanisms such as electron and heavy particle diffusion out of the laser geometry will also affect the net absorption. The breakdown threshold criteria is defined by $N_e/N_0 = 10^{-3}$ from Hughes [32]. Once the plasma has been initiated (N_e/N_0 approaching unity) and particularly at atmospheric pressures, diffusion losses should be minimal due to collisional effects. Recombination is a high pressure loss mechanism which is approximately accounted for in the $1 - e^{-h\nu/kT}$ term of Eqn. (2.3).

The question remains as to whether the semi-classical derivation is valid for the plasmas in this investigation. Hughes [32] notes that the classical derivation is valid for the case when the laser frequency exceeds the plasma frequency. This implies that binary collisions accurately account for photon absorption. This indirectly implies the existence of local thermodynamic equilibrium (LTE) as a Maxwellian distribution is prerequisite. Thus, if one considers the oscillating

motion of an electron in the E-field of the laser, the electron achieves some maximum velocity and hence energy. The "quivering" speed, from Hughes [32], can be shown to be:

$$V_e = \left| \frac{eE_0}{m_e \omega} \right| = 25 \lambda T_e^{1/2} \quad (2.4)$$

where λ is in micrometers and T_e in degrees K. The thermal velocity of the electron is on the order of:

$$V_T = \sqrt{kT_e/m_e} \quad (2.5)$$

From this, the field strength parameter can be defined:

$$\eta = V_e/V_T.$$

If $\eta > 1$, the laser radiation field has an effect on the electron energy distribution, reducing the validity of LTE. For cases in which $\eta \ll 1$, the laser radiation has no effect and the classical IB absorption coefficient, Eqn (2.3), is valid. At a T_e of 20,000 K, $V_T = 5.5 \times 10^5$ and $V_e = 3.75 \times 10^4$, and $\eta < 1$. At a T_e of 10,000 K, the ratio is smaller still and the classical approach appears valid.

One problem in the above simplified treatment is that there is a finite probability of multiple photon absorption prior to stimulated emission. The result is that the criteria for the field strength parameter is relaxed and an average value of V_T should be used. Due to the stochastic nature of the above process, the average thermal velocity

is a nebulous entity and the rule of thumb is that η is less than or equal to one.

An interesting artifact of the difference between classical and quantum derivations is that there is an optimal intensity value, I_{opt} . At this value the plasma will absorb a maximum amount of energy from the incident laser radiation. The classical absorption coefficient (α), valid in the weak field case, shows that power absorption increases with intensity. The quantum derivation accounts for non-linear radiation interaction, the result being that α is inversely proportional to $I^{3/2}$. Thus, the absorbed power decreases with increasing intensity. In the modified limit of the field strength parameter, $\eta = 1$, it can be shown that [32]:

$$I_{opt} \approx 3 \times 10^{12} T_e / \lambda^2 \text{ (W/cm}^2\text{)} \quad (2.7)$$

where T_e is in eV. This generalized term may be of some value in the optimization of laser propulsion systems thermal efficiency. It will also serve as a value to avoid in high energy laser material processing applications as I_{opt} at 20,000 K and 10.6 micrometers is $4.85 \times 10^{10} \text{ W/cm}^2$.

2.3 Transport Equation

The radiative transport equation accounts for the change in intensity as a ray passes through an emitting and absorbing medium. The equation takes the form:

$$n^2 d\left(\frac{I_\omega}{n^2}\right) = (-I_\omega \alpha_\omega + j_\omega) dz \quad (2.8)$$

where n is the refractive index, I_ω , α_ω , and j_ω the frequency dependent intensity, absorption coefficient, and emission coefficient, respectively, and z the direction of propagation. Defining the optical depth, D_ω , and source function, S_ω , as:

$$D_\omega = \int_{\Delta Z} \alpha_\omega dZ \quad (2.9)$$

$$S_\omega = \frac{1}{n^2} j_\omega / \alpha_\omega \quad (2.10)$$

When substituted into Eqn. (2.8), the result is the classical form of the equation of radiative transfer:

$$\frac{d}{dD_\omega} \left(\frac{I_\omega}{n^2} \right) = \frac{-I_\omega}{n^2} + S_\omega \quad (2.11)$$

If the index of refraction variation is small enough over dD_ω (dz), and the source function is negligible at the laser frequency, ω , Eqn. (2.11) reduces to:

$$I_{\omega OUT} = I_{\omega IN} \exp(-\alpha_\omega Z). \quad (2.12)$$

Equation (2.12) is the form utilized in this investigation as detailed in Chapter 3 and Appendix B for the calculation of absorbed laser energy. The complete radiative transport equation is employed in the system energy balance which will be detailed in Chapter 5, discussing the numerical modeling effort.

The radiation terms that comprise the source function, S_ω , are bound-bound, free-bound, and free-free transitions. A detailed treatment of the above terms can be found in Griem [33]. The following is a brief description of the physical nature of the various processes.

Bound-bound (b-b) emission occurs when an electron decays between two well defined energy levels of the system. The result is a discrete line spectrum. A given transition profile depends upon the upper level spontaneous lifetime and the velocity distribution of the atoms which can be expressed via quantum physics as:

$$I_\lambda = \frac{hc A_{mn} g_m N}{4\pi\lambda Z_e} \exp(-E_m/kT_e) \quad (2.13)$$

Where I is the line intensity ($\text{W}/\text{cm}^3\text{-sr}$), at wavelength λ , A_{mn} , the transition probability, g_m the upper level degeneracy, Z_e the electronic partition function (~ 1 for argon), E_m the upper level energy, and N the total number of emitting particles. This relation applies to radiation at a pure wavelength, λ . In practice, the line profile depends on collisions and fields within the plasma volume as well as self-absorption. One broadening mechanism is due to the thermal motion of the heavy particles or Doppler broadening. The Doppler effect results in a Gaussian line profile centered at λ and the half-width is proportional to the heavy particle temperature, T_g . A second effect is Stark or pressure broadening. Stark broadening is due to Coulomb interactions and impresses a quadratic profile which is proportional to the electron number density, N_e . The two broadening mechanisms are

difficult to resolve and one treatment can be found in Griem [33]. A general rule [32] is that Stark broadening dominates the profile when the ionization percentage exceeds 0.1 percent. This is due to the relatively long-range effects of the Coulomb forces. In this investigation, the plasma line radiation is mainly in the near UV to near IR.

The second radiation source is the free-bound or recombination effect. This source occurs when an electron is captured by an ionized atom which subsequently decays with the excess energy emitted as a photon. The spectrum is a continuum with a low frequency cutoff called the recombination limit. The limit corresponds to the minimum energy required to ionize the atom and was seen in the calculation of the bremsstrahlung absorption coefficient. The process is difficult to model as each bound state has a unique continuum which overlaps and the terms must be summed over all bound states. Also, as the density increases, three body processes compete with recombination. Two electrons can collide with an ionized particle and the excess energy carried off by the non-captured electron which further complicates theory.

The third process is free-free or bremsstrahlung radiation. The form is a continuum due to an electron-heavy particle collision resulting in a slow electron and the emission of a photon. In the hot regions of the plasmas electron-ion collisions dominate and in the cooler regions ($<10,000$ K) electron-atom collisions dominate due to the relative number of particles. However, as shown by the rough temperature boundary above, pure numbers are not the only effect.

Electron-ion bremsstrahlung is aided by the long-range Coulomb fields which effectively increase the collision cross-section, similarly to the case of inverse bremsstrahlung absorption. The bremsstrahlung continuum dominates the total emission, particularly in the infrared when $h\nu < 0.7 kT_e$. The relationship arises from the criteria that the emitted photon energy must be less than the local electron energy.

Summing the continuum terms over the internal energy levels and applying Kramers-Unsold theory [29] yields:

$$I_{c\lambda} = 5.44 \times 10^{-46} \bar{g} Z_{\text{eff}}^2 \frac{N_1 N_e}{T_e^{1/2}} \frac{\Delta\lambda}{\lambda^2} \text{ (W/cm}^3\text{-sr)} \quad (2.14)$$

Where \bar{g} is the Gaunt factor averaged over the continuum interval $\Delta\lambda$ and Z_{eff} is the effective charge. Equation (2.14) was calculated using the Planck radiation function based on the assumption that line radiation energy offsets the continuum reduction between lines. A more detailed calculation of the continuum emission was given by Dresvin [34]:

$$I_{c\lambda} = 5.44 \times 10^{-46} \frac{N_e N_1}{T_e^{1/2}} [\exp(hc\Delta\lambda/\lambda^2 kT_e) + \exp(-hc/\lambda kT_e)(\bar{g} - 1)] \zeta(\lambda) \quad (2.15)$$

The first exponential term accounts for recombination to widely spaced lower levels and the second exponential describes the more closely spaced upper level recombination. The factor $\zeta(\lambda)$ is a term derived by Biberman [35] which accounts for the non-hydrogenic behavior of a given system and has been calculated for argon.

The problem is that both Eqns. (2.14 and 2.15) tend to oversmooth the actual continuum, however, the effect is minimal in total integrated

calculations. The total radiation loss calculations are difficult, especially for an optically thick plasma where radiation trapping can occur. In general, real plasmas are treated as optically thin and the optically thick transport is left as a radiative conductivity term, as has been done in this effort. The spectral regions of interest are as follows. In the VUV, the radiation is trapped as the resonant lines and continuum are of comparable magnitudes. The result is that this region is modeled well as a blackbody as long as the pressure is near atmospheric and the temperature distribution is such that higher ionization effects are negligible. The IR spectrum is generally opaque as recombination of the free electrons dominates the process. A general rule in the UV and visible spectrums is that absorption is critical only when $p\lambda > 10\text{-}50$ atom-cm where p is the pressure and λ is a characteristic length of the plasma volume. In the spectroscopic studies in this investigation, $p\lambda$ is typically on the order of 1-2 atom-cm, however, the effects of self absorption are treated in more detail in Chapter 3.

The radiative conductivity has been shown by Dresvin [34] to be approximately:

$$K_r = 3 \times 10^{-4} L T_e^3 \quad (2.16)$$

where L is the mean free path of a photon (Rosseland length). Equation (2.16) can be used over small intervals where the line and continuum magnitudes do not differ by several orders. The contribution of K_r is large in the 2,000 to 16,000 K range and agrees well with experimental

results. However, experimental results have been used in this investigation as detailed in Chapter 5.

2.4 Plasma Propagation and Equilibrium

Early investigations reported the phenomena of plasma propagation into a converging laser beam. Propagation velocities were estimated to be supersonic on the order of 10^5 m/sec. Thus, the analogy to detonation or blast wave phenomena was drawn. Citing the analogy between laser plasma propagation and combustion wave theory is generally attributed to Raizer [36]. The two regimes are laser supported detonation (LSD) and laser supported combustion (LSC) waves. In LSD propagation, the plasma propagates at supersonic velocities and the expansion is radiatively driven. In LSC propagation, the plasma expands at subsonic velocities. The LSC propagation is slow enough for conduction to dominate the transport mechanisms. As was shown in the literature survey, much of the early work, including Raizer's, was interested in defining the plasma/laser parameters involved in the transition regime between LSC and LSD behavior.

In LSD propagation, a strong shock develops near the plasma focus and rapid heating occurs within a narrow shock front. Nearly all the laser energy is absorbed in the narrow expanding front. As the front expands out of the laser beam, the plasma abates due to the lack of an energy source. The gas behind the shock also relaxes to ambient conditions for similar reasons. Due to the high propagation velocities, the shock front is radiatively driven as conduction effects are only important outside the laser beam.

The early experiments were performed with giant laser pulses 10^9 to 10^{12} W/cm². It was soon realized that plasmas could be formed at lower intensities via an external source of electrons to initiate. In this, the LSC regime, the shock expansion does not accurately explain the propagation and plasma state behind the shock. The propagation velocity is subsonic, heat transport is primarily due to conduction and the expansion occurs at close to ambient pressure. The subsonic propagation velocity is proportional to the local laser intensity and the expansion front slows down as it propagates into the converging laser beam. The front stops propagating at the point where the propagation speed matches the induced flow speed. It should be noted that the local mass velocity can be co-directional with the propagation velocity if the expansion front is strong enough to "snowplow" the ambient gas to temperatures well above ambient. This regime was thought to be analogous to slow combustion wave theory, however, the measured expansion velocities were on the order of ten times larger than theory. This discrepancy was later explained by noting that the pressure across the expansion front is nearly constant. In this case, the density ratio across the front is:

$$\rho_a/\rho_s \approx T_s/T_a \text{ and if } T_s \approx 10,000\text{K and } T_a \approx 300\text{K},$$

the factor of 30 accounts for the theory underestimate, where subscripts a and s correspond to ambient and shock conditions, respectively.

In the slow combustion wave, upstream and downstream regions have little effect on one another. The downstream plasma has relatively low

thermal gradients compared to the upstream region. Since weak absorption occurs at any given axial location, the transmitted laser energy is sufficient to maintain the downstream plasma.

The steady-state energy equation is two-dimensional and difficult to solve. An analytical one-dimensional axial solution can only be determined with the application of several simplifying assumptions. These assumptions include linear or constant thermophysical properties and a parallel (non-focused) beam. The analytical models gave way to numerical models incorporating realistic beam geometries and non-linear properties. Most notably Glumb and Krier [22] developed a quasi-two-dimensional model which accounts for real gas argon properties and a converging beam. The model accounts for two-dimensional conduction and one-dimensional (axial) convection. More recently, Jeng and Keefer [24] demonstrated a full two-dimensional solution of the incompressible Navier-Stokes equation. The results of the effort are impressive, however, the need for a full 2-D solution in the case of buoyancy driven plasmas above targets is questionable.

The present effort will follow the work of Glumb and Krier [22]. With the assumption of zero radial velocity, the continuity equation reduces to $\rho u = \text{constant}$. Assuming a constant pressure flowfield, the energy equation remains to be solved:

$$\frac{\partial}{\partial z} \left[K \frac{\partial T}{\partial z} \right] + \frac{1}{r} \frac{\partial}{\partial r} \left[(rK \frac{\partial T}{\partial r}) \right] + \rho u C_p \frac{\partial T}{\partial z} + \alpha I - P_R = 0 \quad (2.17)$$

Where K is the thermal conductivity, ρ the local density, u the axial velocity ($\rho u = \text{constant}$), C_p the specific heat, αI the absorbed power,

and P_R the radiative loss term. It should be noted that the assumption of a constant pu value may be unnecessary. The recent effort of Jeng and Keefer [24] has utilized a full two-dimensional solution of the Navier-Stokes equations for this system. It may be possible to utilize the results of the radial velocity field solutions as a perturbation in the quasi-two-dimensional model. The effect is treated in detail in Chapter 5 as well as the energy equation. It should be noted that in general the various under/over-estimates in properties mentioned previously tend to cancel one another. For example, the underestimate in continuum loss is somewhat compensated by the VUV preheating of the gas which is not accounted for in Eqn. (2.17).

The equilibrium solution of Eqn. (2.17) depends on the thermal conductivity and specific heat. For an equilibrium composition, three relations for each specie and each reaction are necessary. First, the various reactions need to be accounted for. In the case of argon at $T_e < 25,000$ K, only two reactions are applicable:



Equation (2.18) can be expressed via Saha equilibrium as:

$$\frac{N_+ N_e}{N_0} = \frac{2Z_+}{Z_0} \left(\frac{2\pi m k T_e}{h^2} \right)^{3/2} \exp \left[- \frac{(E_\infty + \Delta E)}{k T_e} \right] \quad (2.20)$$

Where N_+ , N_e , and N_0 are the ion, electron, and neutral densities, respectively, Z is the electronic partition function, and E_∞ is the ionization potential. When combined with macroscopic charge neutrality and the law of partial pressures, the composition of any plasma can be determined. Obviously, the number of equations and solution becomes unwieldy except for simple monatomic and diatomic systems.

To determine the specific heat, the enthalpy must first be calculated. The enthalpy is composed of several effects including kinetic, excitation and ionization for argon (monatomic).

$$H = H_{kin} + H_{exc} + H_{ion} \quad (2.21)$$

$H_{kin} = 3/2 kT \sum (N_i + n_e)$ from statistical thermodynamics where the summation is over all energy levels. $H_{exc} = \sum E_{ij} N_{ij}$, where E_{ij} is the excitation energy difference between states i and j . $H_{ion} = E_i N_{i+1}$ where E_i is the ionization potential summed over the pertinent ionization states. Finally, the specific heat is defined from classical thermodynamics as:

$$C_p = \left(\frac{dH}{dT} \right)_p \quad (2.22)$$

It should be noted that for systems involving non-monotonic species, there is a dissociation component of the enthalpy. This factor typically dominates C_p in the 3,000-8,000 K range. Thus, diatomic gases are sometimes preferable in laser welding and cutting as the effect enhances the heating capacity of the laser/plasma system.

The thermal conductivity requires the knowledge of all pertinent elastic collisional cross-sections since at low temperatures (.5 to 2 eV) elastics dominate. The cross-sections of interest in a monatomic system are the electron-ion and electron-atom terms. The e-e, i-i, a-a, and i-a cross-sections are typically orders of magnitude smaller than the e-i and e-a terms. From gas kinetic theory:

$$K = 6.3 \times 10^{-4} \sqrt{T_e/M} / \langle q \rangle \quad (2.23)$$

where M is the molecular mass (gm) and $\langle q \rangle$ is the effective cross-section for momentum transfer (cm^2). Ambipolar and diffusive transport are critical in the exact calculation of the thermal conductivity:

$$K = K_{\text{atom}} + K_{\text{ion}} + K_e + K_{\text{reactive}} \quad (2.24)$$

and

$$K_{\text{reactive}} = K_{\text{ionization}} + K_{\text{excitation}} \quad (2.25)$$

for the case of a monatomic gas. In general, K_e dominates once the ionization is above a few percent. An empirically based relation for K_e was shown by Dresvin [37] to be:

$$K_e = \frac{1.84 \times 10^{-12} T_e^{5/2}}{1/4 \ln(\Lambda_1^4 + \Lambda_2^4 + e^4)} \quad (2.26)$$

where Λ_1 and Λ_2 are simple functions of T_e and N_e . It should be noted that experimental values of thermal conductivity are greater than theory at temperatures above 10,000 K. This is due to the radiation effects

(radiative conductivity) as discussed in the previous section. The experimental measurements cannot distinguish the effects of thermal and radiative conductivity. Thus, numerical modeling efforts utilize the experimental values and could implement a ratio of Eqns. (2.26 and 2.16) to attempt to specify a relative magnitude, if necessary.

2.5 Plasmas in Pure Gases

In this investigation, pure argon plasmas are initially investigated. The effort is in support of a study of the use of laser supported plasmas for the direct heating of a propellant for propulsion. Argon has been chosen from the standpoints of well documented thermophysical properties and safety. Argon is also used as an assist gas in several laser material processing applications. Thus diagnostics developed in the pure gas system can be used in the study of plasmas formed above metallic targets in argon atmospheres. This section summarizes the effects and properties of the pure argon plasmas as detailed in the previous sections.

Figure 1 is a schematic of the physics of a flowing gas laser supported plasma (LSP) system. The plasma is initiated by inserting a zinc foil or tungsten target at the laser focus. The vaporization/thermionic emission of the targets produces an electron density in the range of 10^{11} to 10^{14} cm^{-3} . These densities are sufficient to lower the breakdown threshold in the argon but not alter the physics of the breakdown mechanisms. Upon initiation, the target is removed and the plasma stabilizes in the converging beam. Since the laser intensity is in the 10^5 to 10^7 W/cm^2 range, the breakdown is

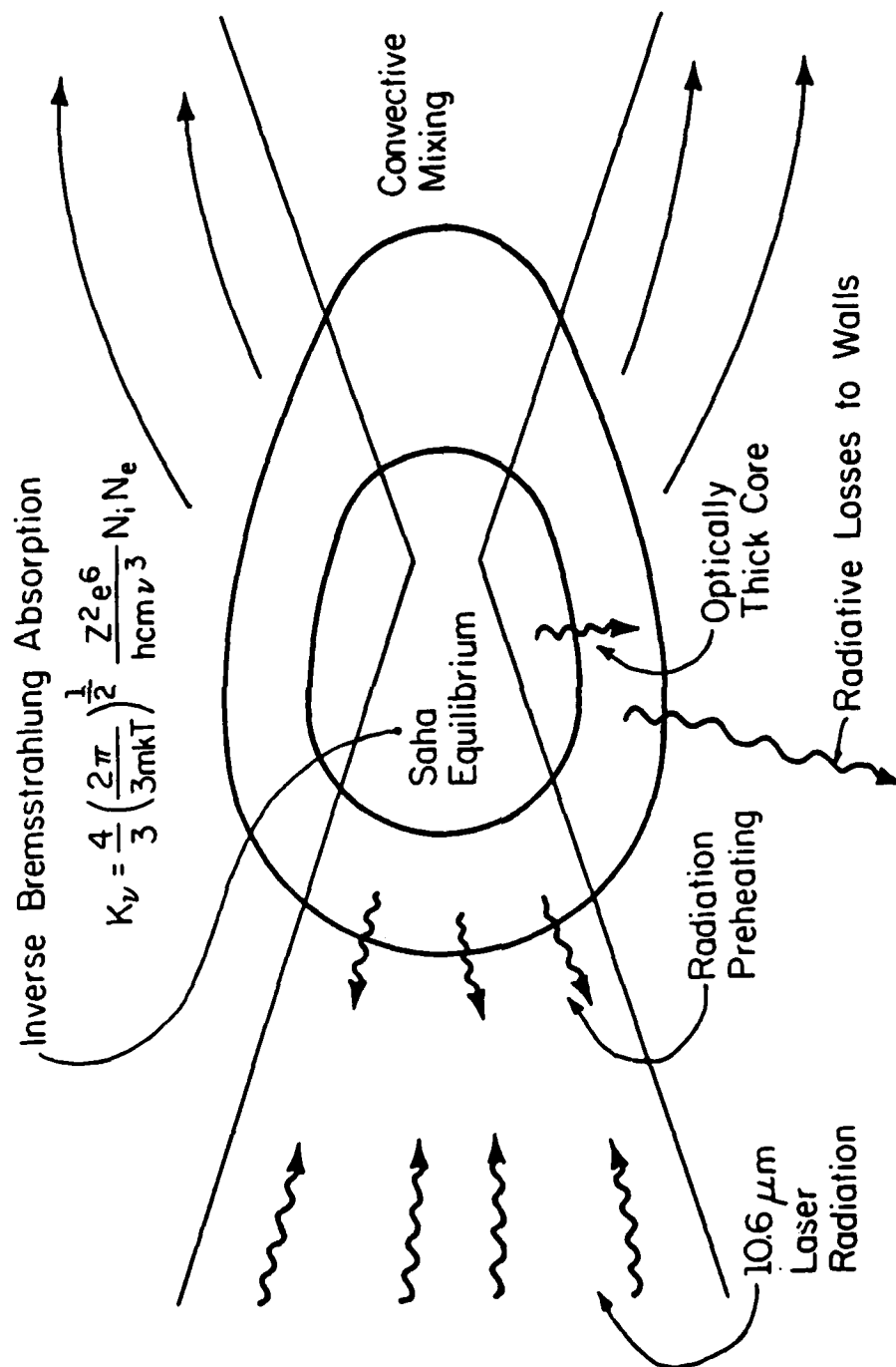


Figure 1 Pure Gas Plasma Physics

characterized as the "slow combustion wave" or laser supported combustion (LSC) regime.

In the LSC regime the plasma expansion front propagates at subsonic velocities and the velocity is intensity dependent. The plasma front stabilizes at a position in the converging laser beam where the propagation velocity matches the applied flowfield velocity. The plasma expansion is driven primarily via conduction to the gas upstream from the plasma front. The front is weakly absorbing and sufficient laser energy is transmitted to the downstream regions to maintain the plasma volume.

The absorption mechanism is inverse bremsstrahlung in the focal volume and conduction drives the plasma volume outside the laser beam geometry. There are two effects of radiation. First, the VUV emitted by the hot plasma core preheats the upstream gas. Second, the radiative conductivity is a significant percentage of the effective thermal conductivity which supports the plasma outside the laser geometry.

Two concerns arise in a laser propulsion scheme. First, the radiation losses from the hot plasma region to the containment vessel walls may be considerable. Factors affecting radiation losses are pressure, flow rate, and beam geometry. In general a long, narrow plasma at high flow rates or a larger, cooler plasma is desirable. The purpose of the LSP investigation is to quantify these effects and verify the trends predicted by a numerical model [22]. The system shown in Fig. 1 is a dual flow system in which part of the impressed flowfield is directed over the chamber walls for convective cooling. The main goal of the LSP work is to optimize thermal efficiency defined as

$E_{\text{thermal}}/E_{\text{incident}}$. Thus the convective mixing of the cooler outer flow field and the directly heated gas is critical. Thermal efficiencies in excess of 50 percent are desired if laser propulsion is to be feasible. An additional constraint is that the mixing in the downstream region results in temperatures in excess of typical combustion product temperatures ($> 4,000$ K). The gas would eventually be expanded in a supersonic nozzle to convert thermal energy to kinetic energy or thrust. A complete review of this application can be found in the paper by Glumb and Krier [20].

2.6 Plasmas Formed Above Metal Targets

To accurately model the breakdown of an ambient gas and vapor system the target physics of heating, melting, vaporization, and ionization must be accounted. Two extreme cases exist. At low intensities the target surface temperature rises and conduction increases internal temperatures, with no phase changes. At high intensities multiphoton ionization rapidly initiates the plasma above the target. Between the two limiting cases, the breakdown physics must include the processes of change of phase, vaporization pressure, thermionic emission, and shock wave formation. To further burden the effort, the temperature dependent optical properties must also be accounted.

In this investigation, the main concern is with the steady state plasma volume. The initiation mechanics can be disregarded as they have been shown to effectively be a source of free electrons. The breakdown and subsequent plasma formation are independent of the initiation

mechanisms. A detailed treatment of the initiation physics can be found in Raizer [38] for the CW case and Hughes [39] for the pulsed case.

Intensities are again in the 10^5 to 10^7 W/cm² range and LSC theory adequately describes the plasma initiation and propagation. At higher intensities ($>10^{10}$ W/cm²) the plasma formation is analogous to detonation or blast wave theory and several references can be found in the literature review. Figure 2 is a schematic of the physics of a plasma formed in an atmosphere above a metallic target. When the laser beam is focused onto the target rapid melting and vaporization occur. Surface defect heating also aids in the plasma initiation. The metallic vapor is initially contained in the keyhole region which is at high pressures on the order of a few atmospheres.

A shock wave may initially expand, but the shock is weak in the LSC case and does not heat the ambient gas to temperatures high enough for laser absorption to begin. The shock is followed by a slower contact discontinuity which separates the initial nonequilibrium expansion of the metallic vapor as it "snowplows" through the ambient gas. Experimental results in the LSC regime have indicated two significant features. First, the pressure throughout the steady-state plasma volume including the region at the keyhole/ambient interface is nearly constant at the ambient value. Second, the Mach number just outside the keyhole region has been measured to be on the order of 0.05. Thus some effect must restore equilibrium to the metallic vapor across the interface. The currently accepted model was proposed by Knight [40]. A discontinuity analogous to a Knudsen layer could be attached to the target surface to restore translational equilibrium to the metallic vapor. The

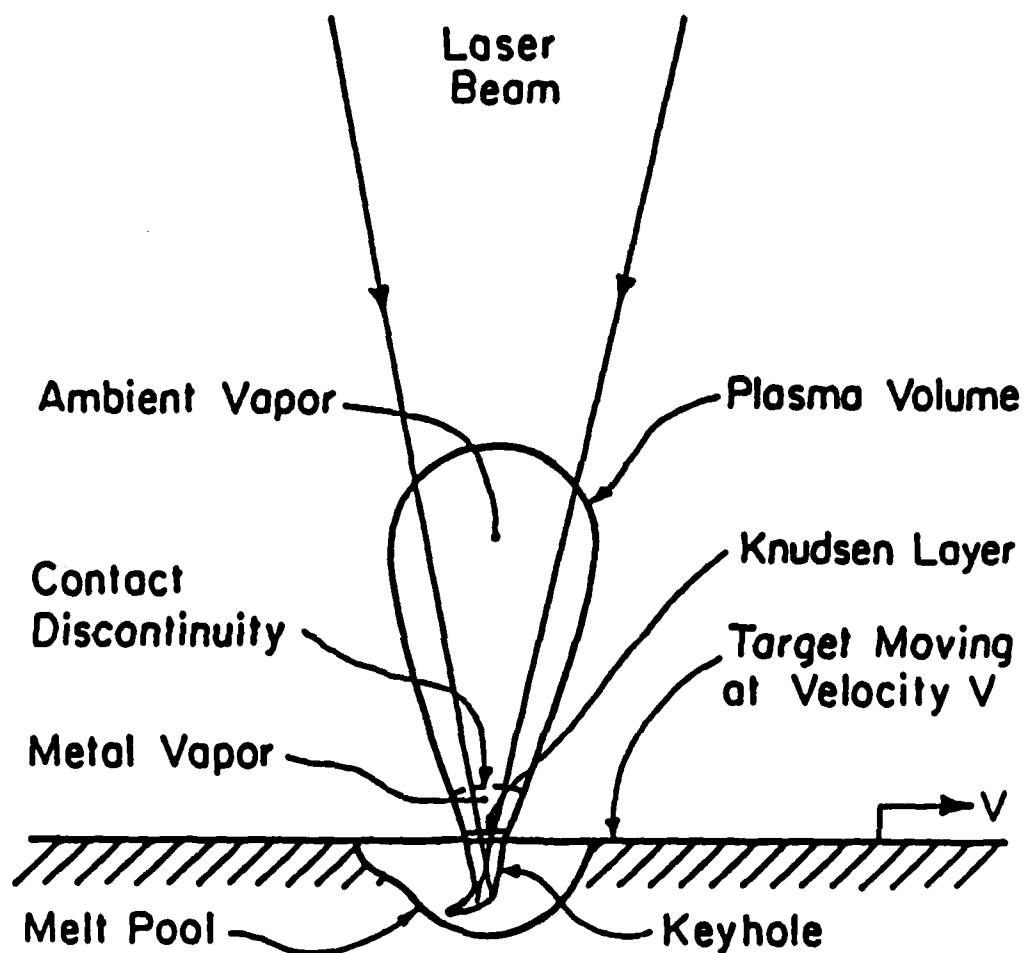


Figure 2 Metal-Gas Plasma Physics

Knudsen layer is a discontinuity which restores translational equilibrium to the high pressure material vapor as it expands into the ambient. The temperature decrease across the Knudsen layer would be sufficient to maintain the plasma by supporting a sufficient electron density at the interface. In this study, it has been seen that the metallic vapor line spectrum is evident in a small region near the target surface. The metal vapor continuum may affect the continuum throughout the plasma and will be analyzed in Chapter 4.

The remaining problem concerns the electron and heavy particle temperatures near the target surface. The metal vapor, as expected, is a few hundred degrees above the melting point. If total equilibrium were to exist, the electron temperatures would also be at a similar temperature. However, for the plasma to exist, the electron temperatures in this region must approach 10,000 K for IB absorption to occur. This criteria also forms a necessary boundary condition for the plasma modeling. The analysis of this region is presented in Chapter 5.

2.7 Energy Transport to the Ambient

As was seen in the literature survey (Chap. 1) little or no effort has been made to assess the role of various heat transport mechanisms between the plasma and a target. In a laser supported plasma the primary mechanisms are conduction and radiation. The magnitudes of the effects with respect to the transmitted laser flux are of primary concern if an accurate assessment of the target flux is to be made.

Most references on plasma heat transfer concern convective transport to a body in transverse flow. In this application, similarity

functions with appropriate reference temperatures and temperature corrections have been successfully applied to plasma transport calculations. Other factors affecting the calculations include nonequilibrium mechanisms such as dissociation and ionization and the inverse processes. Hot particle diffusion to walls, plasma radiation, and generation of sheaths are other considerations.

However, for the plasmas investigated herein, the major concern is of transport to confinement vessel walls and/or to a target. As examples of the magnitudes of the transport phenomena, various figures in the literature reported the radiative flux from the plasma varying between a few percent to nearly 100 percent of the total flux delivered to the target. Several arc plasma studies have attempted to monitor the radiative and total flux for the regions of a) chamber walls and b) anode (target) surface.

Lukens and Incropera [41] showed that radiation accounts for as much as 30 percent of the wall loading. The effort was an attempt to model various mechanisms in a constricted argon arc jet. The 30 percent figure corresponds to the fully developed flow region near the anode. The result of the equilibrium model was an overestimate of the radiative flux. It appeared that a nonequilibrium model incorporating unique electron and heavy particle temperatures was more realistic. However, this effect may be an artifact explained by Ref. [24] in that the diffusion approximation overestimates radiative conductivity at pressures below two atmospheres. This argument will be treated in Chap. 5.

Ushio and Matsuda [42] assessed the target transport in an argon TIG welding assembly. The TIG process involves a forced convection flow from the cathode to anode (target) and the relative magnitudes of conduction and convection are not separable. However, the combined effect of conduction and convection was calculated to be 8 percent of the total arc power. Radiative transport was not mentioned except in the problem formulation and one assumes this to mean that radiation effects have little significance.

As a first order formulation, from the results presented in Chap. 4, an assessment of the radiative flux will be made. The plasma is modeled as a disk in the range of 2-5mm radius, residing 1-3mm above the target. A classical radiative view factor can be calculated between the disk and the refracted laser spot. Assuming all the absorbed laser energy is lost as radiation, half of which is emitted toward the plasma, the net radiative flux can be shown to be less than 2 percent of the transmitted laser flux. In most cases, the value is less than 1 percent. The radiative flux is on the order of 10^2 W/cm^2 in this region, so effects outside the laser geometry should also be negligible. Thus, it remains to assess the conduction heat transfer as the small radial velocities encountered in this investigation should minimize the effect of convection. Conduction will be detailed in Chapter 5.

2.8 Local Thermodynamic Equilibrium (LTE)

Several equilibrium models exist for high temperature ionized gas systems. All the models are based on the assumption that all particles

have Maxwellian velocity distribution although not necessarily at the same characteristic temperature. LTE also assumes that the system is of sufficient density for collisional processes to dominate the rate equations. This implies that all energy levels obey Boltzmann statistics. Coronal equilibrium assumes that the density is low enough for radiative processes to dominate the rate equations. This can be interpreted as the gas temperature being low enough that inverse bremsstrahlung absorption does not occur in the plasma volume ($< 10,000$ K). This condition is obviously invalid in the case of a laser supported plasma and applies more to arc discharge plasmas. The gray area between the two regimes is covered by collisional-radiative equilibrium and various partial- or multi-temperature local thermodynamic equilibrium models. These last models are more complex and make it desirable to use either of the first two models. At pressures approaching atmospheric, the LTE model appears to be valid. In most investigations, LTE has been applied via statements such as "...has been shown in previous studies..." or, "It is well known that LTE prevails at these conditions.". The validity of LTE will now be explored for the plasma conditions of T_e greater than $10,000$ K and atmospheric pressures.

Griem [43] makes several points regarding LTE. Spatial variations in the temperature field should be small enough that diffusion of heavy particles is negligible during equilibrium relaxation times ($\sim 10^{-12}$ sec). Griem also notes that if LTE is valid, the electron and heavy particle temperatures should not differ significantly. This is due to the relatively efficient coupling of energy between electrons and heavy particles since the heavy particle mean free paths are

relatively short, offsetting the effect of mass ratio. Electron loss processes such as radiation actually lower the restrictions on LTE since the energy transfer requirements between particles have been decreased. Heavy particle conduction losses would restrict LTE but are usually small compared to electron losses. Finally, in the outer radial regions where temperature gradients are maximum, diffusion of hotter heavy particles from the core tend to offset the gradients and maintain LTE.

A schematic of the energy transport within a monatomic plasma is shown in Fig. 3 [27]. In general, the electron density must be high enough for collisional de-excitation to be roughly ten times more probable than radiative de-excitation. For an optically thin plasma, considering the cross-sections, the Saha equation can be reduced to [43]:

$$N_e > 1.6 \times 10^{12} T_e^{1/2} (\Delta E)_{\max}^3 \text{ cm}^{-3} \quad (2.27)$$

Where ΔE is the largest energy difference (eV) between excited states. For pure argon, the first excited states are approximately 70 percent of the ionization energy hence E_{\max} is in the range of 3 to 5 eV. This range corresponds to an electron number density of 10^{16} cm^{-3} which appears a reasonable value at the prescribed conditions.

To investigate the temperature difference between the electrons and heavy particles one looks at the energy equation:

$$\rho u C_p \frac{dT}{dz} = b(T_e)(T_e - T_g) \quad (2.28)$$

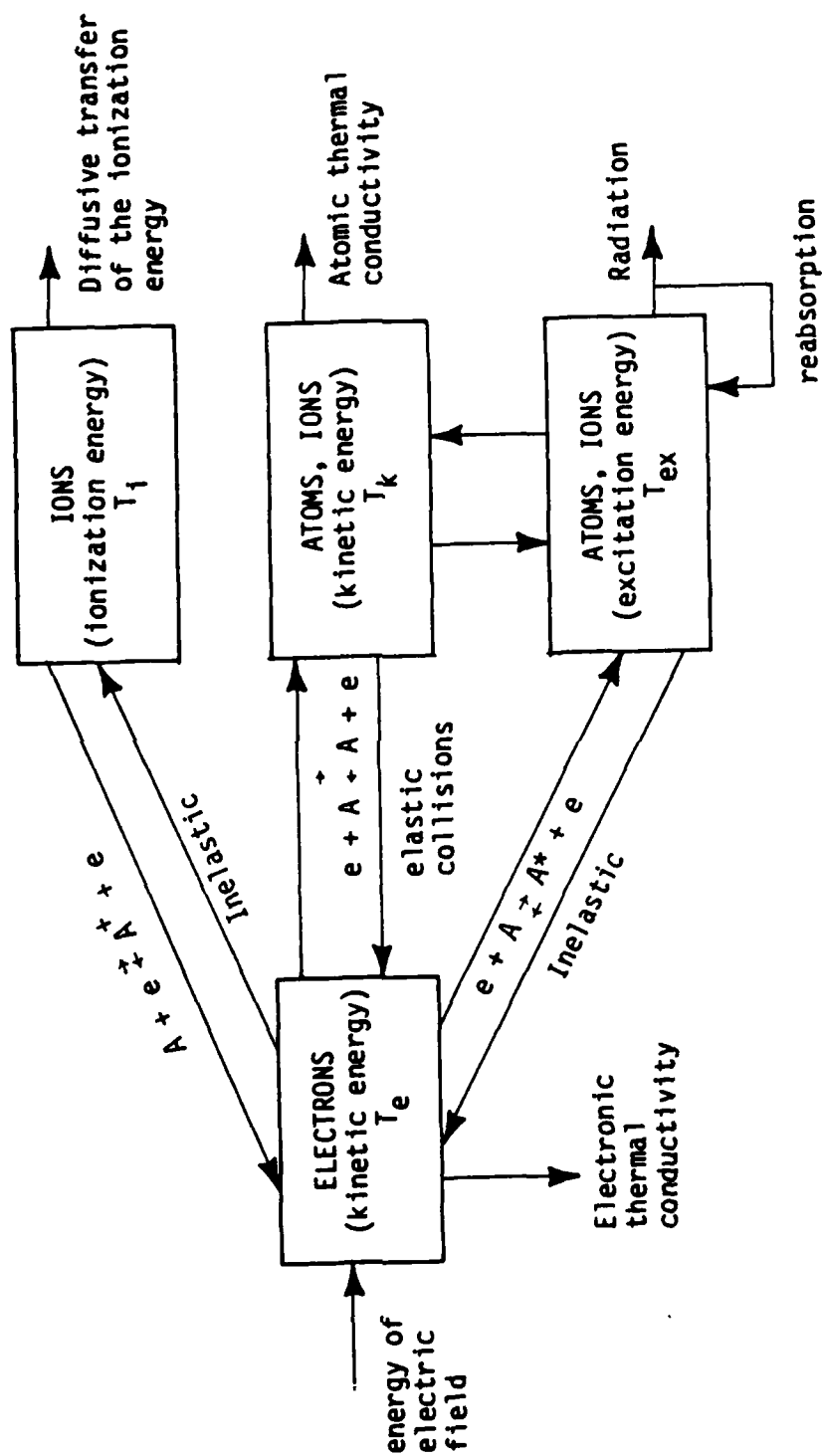


Figure 3 Electron-Heavy Particle Interaction Diagram

where b is a function of the electron number density and plasma frequency, hence $f(T_e)$. The equation assumes radial conduction is negligible and has been solved numerically by Dresvin [37]. At $\rho u = .5 \text{ g/cm}^3\text{-sec}$ and constant $T_e (=13,000 \text{ K})$, $T_g = T_e$ within the first 4mm of cool gas flow into the plasma volume. If the energy equation is solved assuming the axial (z) temperature gradients are zero, one finds that the electron and heavy particle temperatures are within a few percent over the central 2-5cm radii. Thus, at temperatures in excess of 10,000 K, the equivalence should extend to larger spatial dimensions.

Eddy [44] published a classical review of equilibrium models and proposed the concept of multithermal local thermodynamic equilibrium (MLTE). In the MLTE analysis, the various excitation, electron, and heavy particle temperatures are accounted for. Eddy also analyzes the probable error of the various spectroscopic diagnostic techniques where LTE is assumed. The analysis assumes a 10 percent measurement error. The absolute line intensity method appears to be the minimal error at .3 to 3 percent at $T_e = 20,000 \text{ K}$. The off-axis peak method also has a 3 percent error. The ratio of ionic to atomic argon lines resulted in a 5% error in temperature. Thus, the ion-ion ratio should be near this magnitude as the energy differences are similar and the ion-ion ratio does not depend on validity of the Boltzmann relations as much as the ion-atom technique. Line to continuum technique errors at similar conditions appear to be 10 percent. It will be shown in this investigations experimental results that a ± 15 percent error in the

calculated temperature field results in a less than ± 5 percent deviation in the global properties of absorption and radiation loss.

Farmer and Haddad [45] attempted to experimentally verify LTE in an argon arc plasma. The theory is that the measured emission coefficient ($\text{W/cm}^3\text{-sr}$) must be identical for regions of identical temperatures. The baseline temperature was the off-axis peak or "norm" temperature location. The authors concluded that an arc plasma at a pressure of 1.4 atm demonstrated LTE behavior (± 5 percent) over the entire arc column. However, at 1 atm pressure, the error is also ± 5 percent except in the region near the cathode ($\pm 20\%$). This is possibly due to electron charge repulsion in the area near the cathode and LTE again appears to be valid for an atmospheric pressure laser supported plasma.

Finally, as a first order calculation, theory is combined with experiment in order to derive a function proportional to the electron energy distribution. From gas kinetic theory, the thermal conductivity can be expressed as in the form of Eqn. (2.23). Equation (2.23) was derived for $\langle q \rangle$ independent of temperature. A rigorous derivation of thermal conductivity makes comparison between experiment and theory difficult. Thus, as a first order approximation, $\langle q \rangle$ will be allowed to vary with temperature in Eqn. (2.23). It should be noted that the large range of calculated values of $\langle q \rangle$ make the variation with electron temperature assumption a small error since a discrete analysis could be performed by adjusting the constant term of Eqn. (2.23).

If one applies the conductivity data of Emmons [46] for argon at 1 atm, 4,000-14,000 K, one can calculate $\langle q(T_e) \rangle$ by inverting Eqn. (2.23). Using the measured data of Golden and Bandel [47] for the

total momentum transfer cross-section, $q(E)$, it is possible to derive a function proportional to the "experimental" distribution function, $f(E)$.

$$\langle q(E) \rangle \propto \int q(E) f(E) dE \quad (2.29a)$$

and

$$f(E) \propto [d \langle q(E) \rangle / dE] / q(E) \quad (2.29b)$$

The data and theoretical profiles were fit to fifth order polynomials via least squares. The resulting distribution function (not normalized) is shown in Fig. 4.

One notes the two-temperature appearance of the distribution with the break occurring at 1.05eV (~ 11,000 K) This is due to the radiative conductivity, as discussed previously, in the data of Emmons [47] at temperatures above 10,000 K. If one uses theoretical values of thermal conductivity (no radiation effects) the result is the dashed line in Fig. 4. Thus the piece-wise linear (logarithmic) behavior of the distribution further supports the assumption of a Maxwellian velocity distribution. Since the effort is concerned with temperatures above 10,000 K, it appears that a single characteristic electron temperature will describe the system adequately.

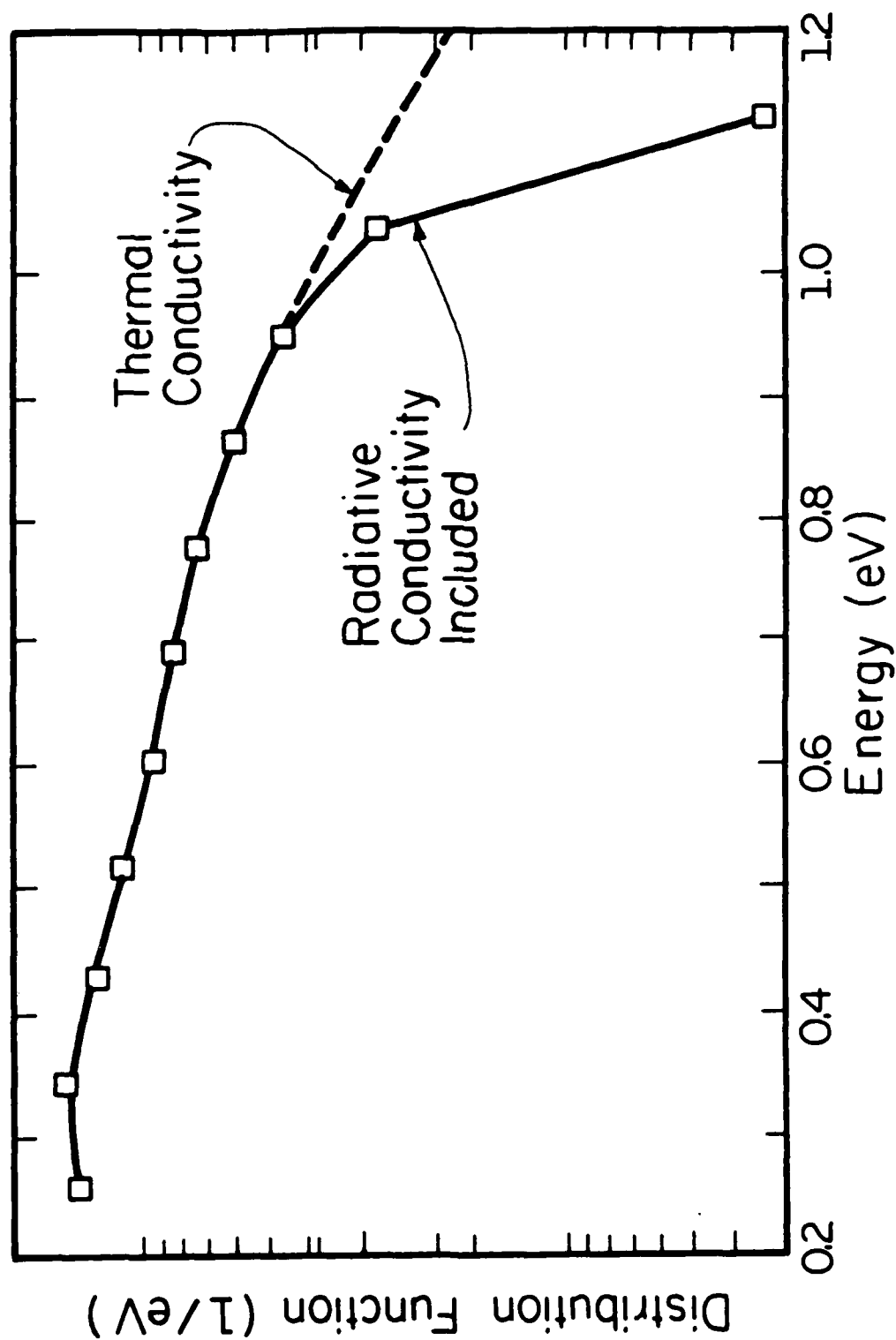


Figure 4 Non-normalized Calculated Electron Energy Distribution

3. EXPERIMENTAL APPARATUS

Two plasma chambers have been developed for this research effort. The first chamber is used in the pure argon studies and was designed to incorporate multiple diagnostics. The plasma initiation and flow chamber (PIFC) includes thermocouple, calorimeter, pressure, and optical diagnostic ports. The PIFC was a collaborative design effort for the previously mentioned AFOSR project. The details of the design can be found in the theses of J. Bender, M.S. 1985 [48] and R. Glumb, Ph.D. 1986 [49]. The second apparatus, the plasma initiation chamber (PIC), is used in the study of metallic plasmas in controlled atmospheres. PIC incorporates a translation stage to continually refresh the target material as well as pressure and optical diagnostic ports. This chapter will detail the two plasma chamber features, describe the diagnostic apparatus, and pertinent data reduction techniques.

3.1 Plasma Initiation and Flow Chamber (PIFC)

A schematic of the PIFC, support stand, and beam steering optics is shown in Fig. 5. The stand is constructed of heavy steel unistrut framing and is mounted on four pneumatic tires. The system is positioned into the laser beam path and can be located via alignment pins into holes in the floor.

The laser is a 10 KW CW Avco Everett HPL-10 system. The laser is an unstable oscillator with an annular beam similar to a TEM_{01+} beam profile. The beam is focused to pass through an aero-window and subsequently reimaged to an approximate 2.6 in. diameter at the outer $1/e$ location (1.98 in. ID). The beam is delivered horizontally across

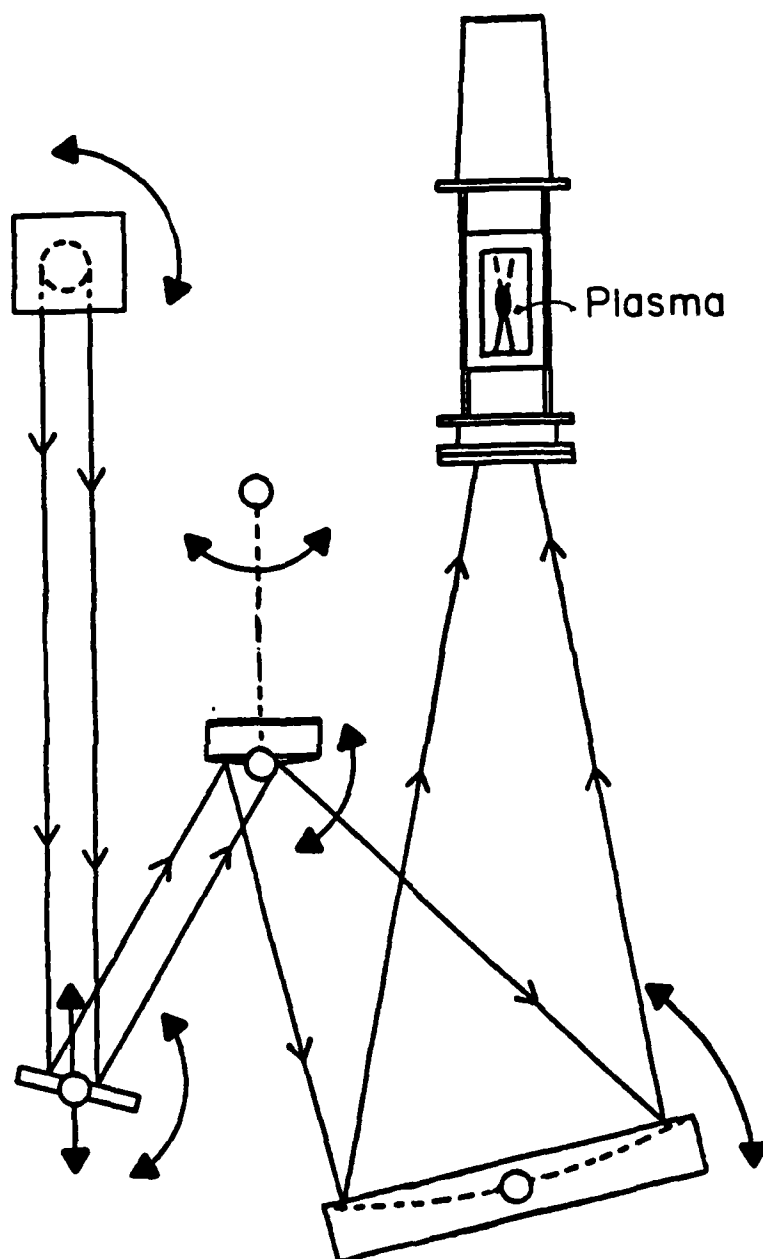


Figure 5 PIFC and Optical Assembly Schematic

the laboratory to the flat copper mirror shown in the upper left-hand corner of Fig. 5. The beam is reflected 90 degrees downward onto a second copper flat which reflects the beam upward into a 6.0 in. diameter convex copper mirror ($R = 12$ in.). The convex mirror expands the beam into a 20 in. diameter concave primary focusing mirrors ($R = 31$ in.).

The arrangement permits the beam to be focused vertically upward into the PIFC which minimizes the effects of buoyancy in plasma stability and diagnostics. The system also permits a variable $f/\#$ (defined from the primary mirror to focus) of $f/2$ to $f/3.4$ which was a parameter of interest at the onset of the project. The $f/\#$ is changeable by relative translation and rotation of the lower flat, convex, and concave mirrors as shown in Fig. 6. The low $f/\#$ s provide for a large beam cross-section, minimizing local intensity, as the beam enters the PIFC through a NaCl window, minimizing window damage. All the mirrors are water cooled to prevent thermal damage except the 20 in. mirror which has sufficient mass to conduct energy away from the mirror surface.

The optical system is off-axis and depending on the $f/\#$, a significant amount of aberration may be present in the focal volume. Figure 7 shows two orthogonal intensity mappings of the annular focal volume. The data was acquired using a laser beam analyzer, Model LBA-1A, from ALL GmbH, West Germany. The instrument passes a molybdenum needle through the laser beam and the reflected energy is detected by two orthogonal photodiodes. The output is stored on a digital storage oscilloscope where accurate time-base measurements of the intensity

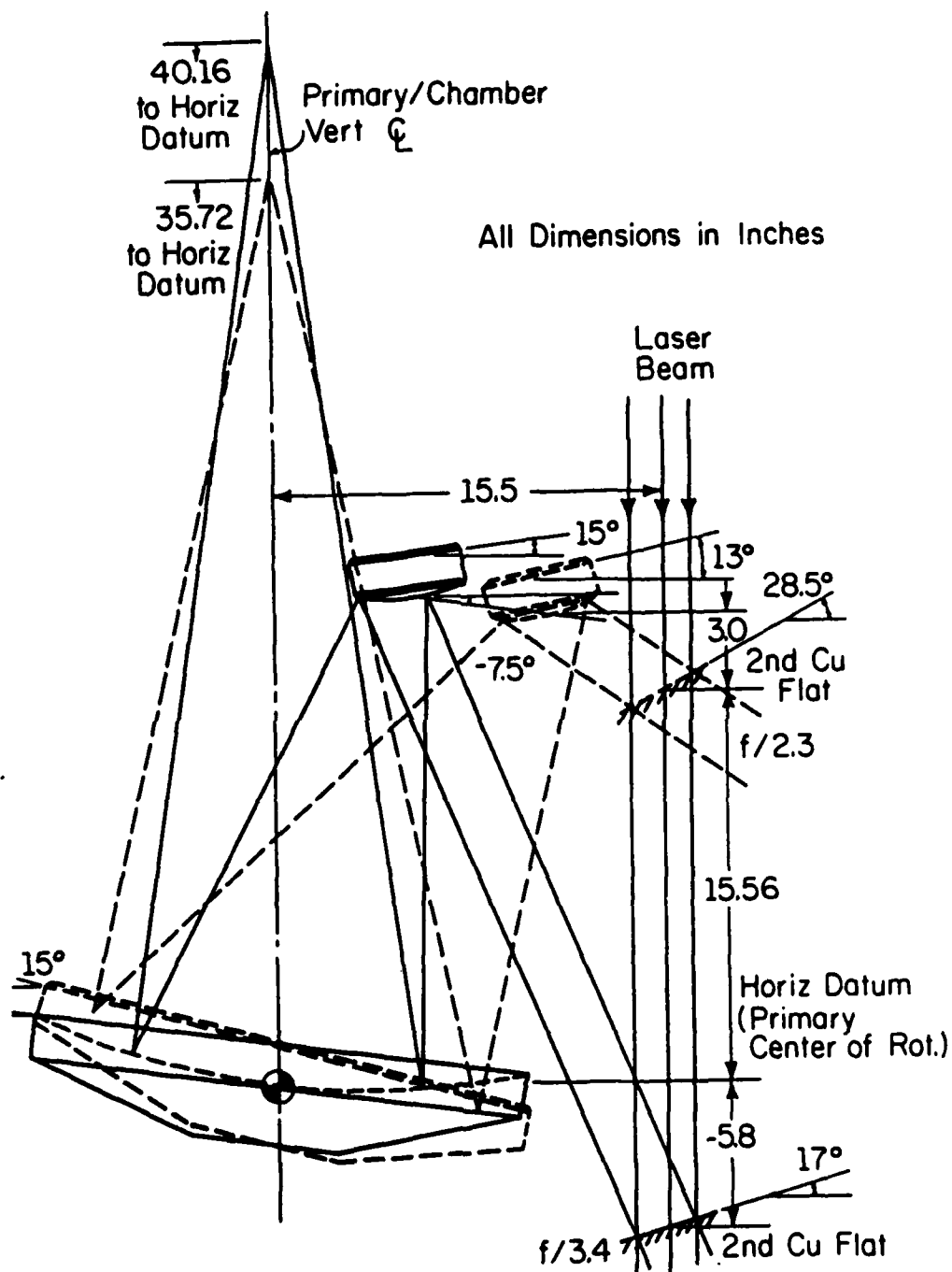


Figure 6 Optical Beam Delivery Schematic

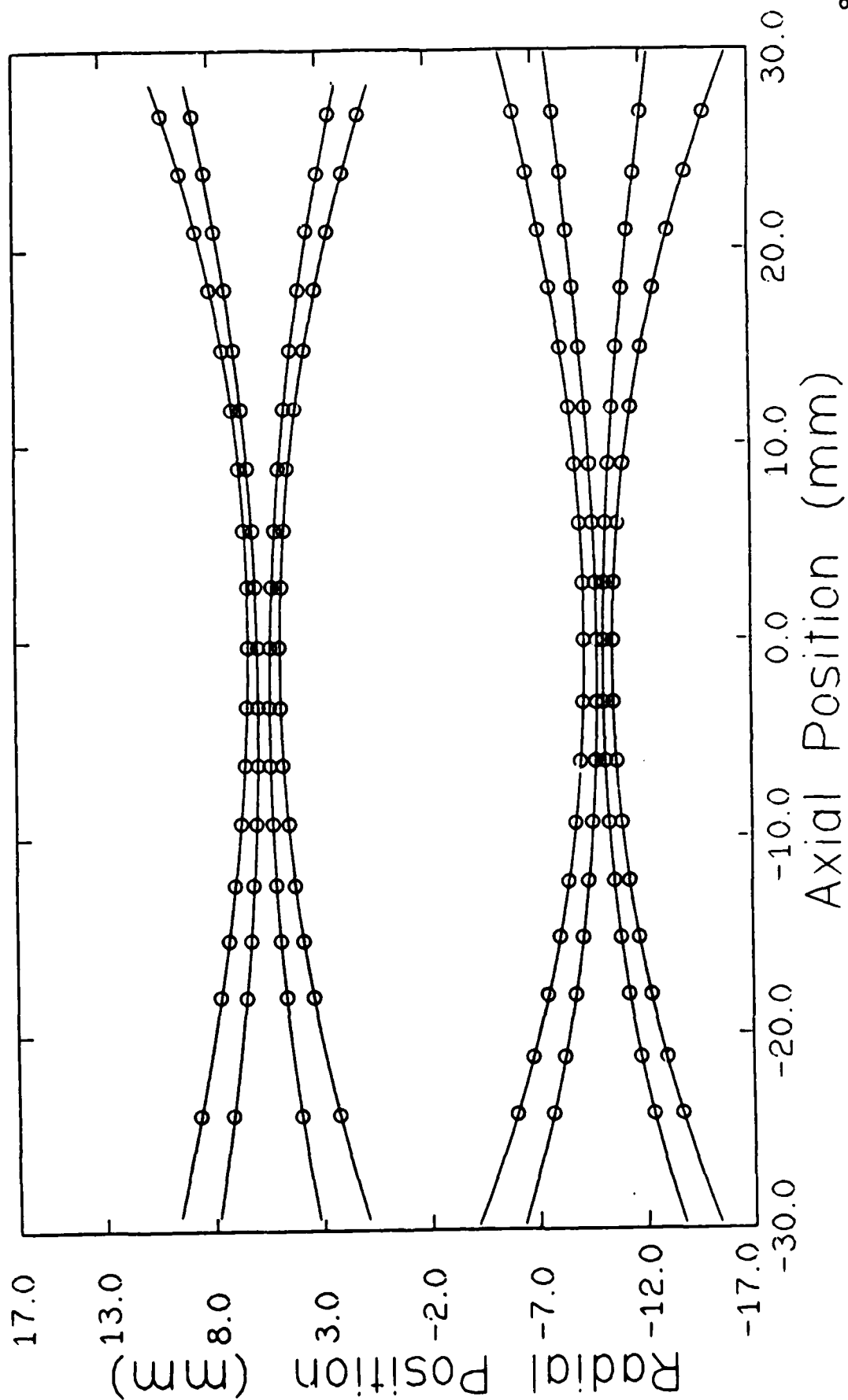


Figure 7 Intensity Profile of f/3 PIFC Focal Volume

profiles can be made. The time-base is converted to spatial dimensions using the calibration figures supplied with the LBA.

The solid lines in Fig. 7 are a third order curve fit of the indicated data points which are the $1/e$ loci of the annular focal volume. One sees the effect of the off-axis optical system in Fig. 7. The one trace is generally wider than the other on the positive side of the focus. The trend is reversed on the negative side of the focus. This implies that the beam is elliptical and astigmatism is present. However, no tangential or sagittal focus could be found in the IR or visible (HeNe) focal volumes. Unfortunately the detector saturates at the intensities encountered in the focus region, resulting in a narrow trace. The best estimate of the circle of least confusion is two millimeters based on the behavior in the outer thirds of the traces. This figure agrees fairly well with the HeNe tracer laser estimates but further attempts to prevent LBA saturation should be made.

The PIFC is a 5.0 in. ID stainless steel cylinder. Stainless steel was chosen for corrosion resistance, relatively high melting point, and strength. The large diameter was chosen to minimize radiative heating of the walls and minimize wall effects in the downstream mixing region. This type of design is typically called a dual flow chamber. Cooler outer gas convectively cools the walls and subsequently mixes with the directly heated gas from the plasma volume. Figure 8 is a schematic of the various components of the PIFC.

At the bottom of the PIFC is a flange which holds the NaCl inlet windows of varying thickness, depending on chamber pressure. Inlet gas is brought in radially via a series of small holes on the inside of the

- (A) Laser Inlet Window Assembly
- (B) Gas Inlet Assembly
- (C) One-Half Inch Inlet Pipes (2)
- (D) Main Chamber Section
- (E) Thermocouple Wire Retract Box
- (F) Viewing Windows (2)
- (G) Target / Solenoid Assembly
- (H) Pressure Transducer and Popoff Valve
- (I) One-Half Inch Exhaust Pipes (4)
- (J) Thermocouple Drive Motor
- (K) Calorimeter
- (L) Laser Inlet Window

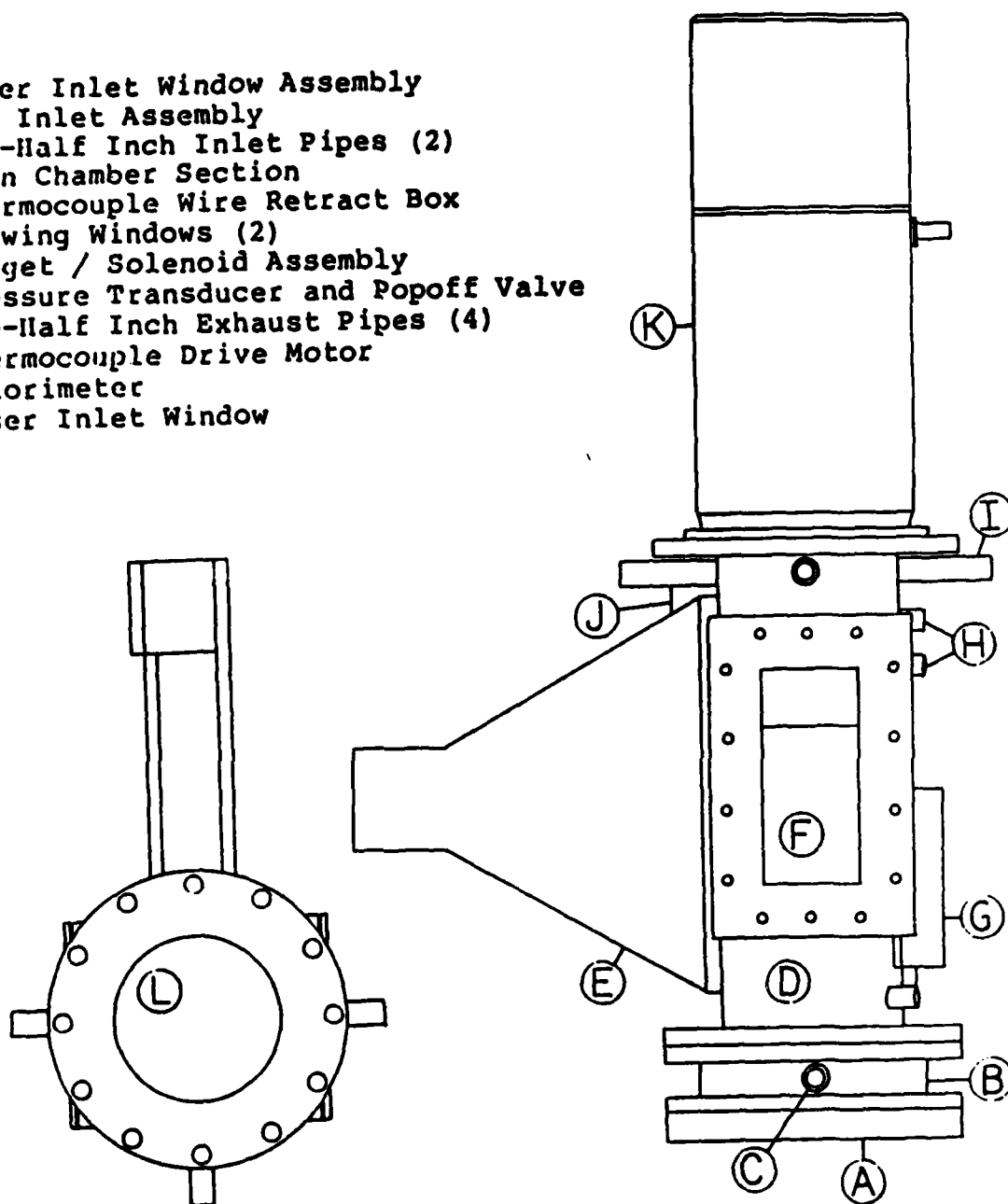


Figure 8 PIFC Components [49]

PIFC. Some of the gas is diverted onto the window for cooling, part is directed normal to the vertical, and the remainder directed downstream.

Above the inlet assembly is the plasma containment region. Diagnostic windows provide direct optical viewing of the plasma event. The thermocouple box contains the excess wire needed to permit thermocouple movement along the vertical via a carriage/slider assembly. Pressure transducers, pressure relief valves, stationary thermocouples, as well as other ports, are also located in this region. Above the main chamber the gas is exhausted through four ports, recombined in a manifold and passed through a tube in shell heat exchanger before being exhausted to the ambient. At the top of the chamber a water cooled copper cone calorimeter is mounted. The calorimeter is used to measure the laser power transmitted by the plasma and the global plasma absorption can be determined. When not being used as a diagnostic tool the calorimeter serves as a beam dump. Particular details of the design and assembly can be found in the theses by Bender [48] and Glumb [49].

The experiment begins when the laser beam is delivered to the mirror system and focused into the chamber. Peak intensities of the laser/optical system are on the order of 10^6 W/cm^2 which are insufficient to breakdown the flowing argon without an initial source of free electrons. The electrons are created by inserting a zinc foil or more recently a reusable tungsten rod, into the focal region via an air cylinder/solenoid assembly. Target vaporization is sufficient to create a high enough electron density for cascade breakdown in the argon to

occur. The plasma then stabilizes in the converging beam as discussed in Chapter 2 and the various diagnostic techniques can be applied. Figure 9 is a double exposure of the chamber and plasma during a typical experiment.

3.2 Plasma Initiation Chamber (PIC)

To facilitate the study of plasmas formed above metallic targets, a second chamber (PIC) was designed. Figure 10 is a drawing of the PIC features. The system is a rectangular aluminum box (inside dimensions of 14 in. by 5 in. by 5 in.) with 0.5 in. thick walls. Aluminum was chosen for machinability as wall degradation was found to be minimal in the PIFC experiments. One-half inch thick walls were chosen to add mass to the unit in consideration of heat transfer effects. The thick walls also permit absolute pressures up to 3 atmospheres to be maintained with a factor of safety of two, assuming proper window design and installation.

The beam is delivered to the target via a rectangular or circular NaCl window in the top of the chamber. All windows are flange mounted with inner and outer O-rings for sealing and cushioning. Since the laser focus rapidly begins drilling the target an internal translation stage was incorporated. The stage continually refreshes the target material minimizing drilling effects and maintaining the laser target interaction as a surface event. The translation speed can be varied up to the point where the plasma deflects out of the laser beam geometry. This condition makes the diagnostic techniques invalid from symmetry considerations. Translation speeds up to 60 in./min were found to have

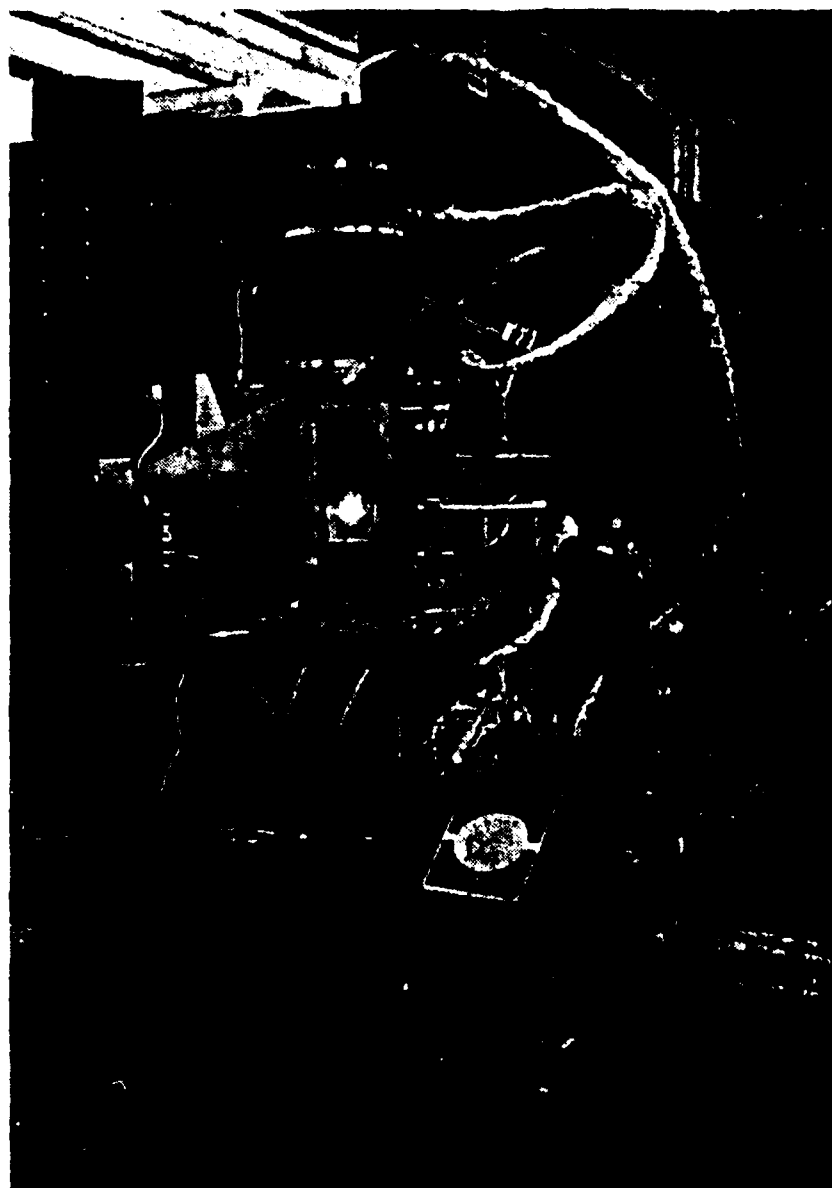


Figure 9 Double Exposure Photo of PIFC and Plasma

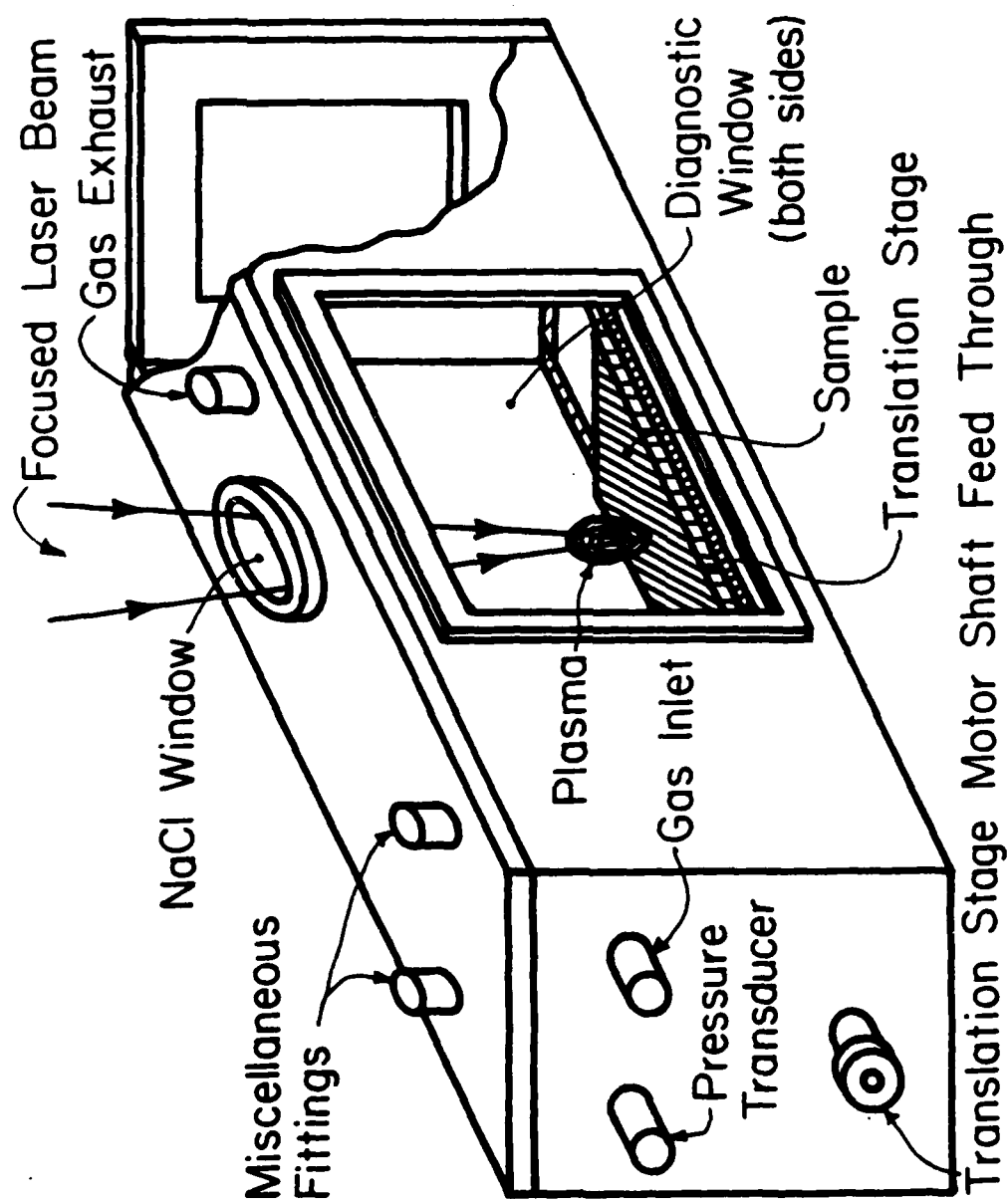


Figure 10 PIC Schematic

no effect on plasma deflection in this study. The translation parameters are controlled via a Vellmex® control unit configured as a dumb terminal and connected to a host terminal. The system uses a form of BASIC language and up to four motors can be controlled independently. This system will be discussed further in Section 3.3.

The stage motor is mounted externally and is sealed with an O-ring and flange apparatus to prevent infiltration. The stage is 12 in. long with a net translation distance of 8 in. end-to-end. In general the translation speed was set to a slow value to permit multiple data acquisition during a single translation. Multiple data acquisition ensures data integrity and typically two to four scans at various elevations above the target could be performed during a single translation. After a given internal translation of the PIC stage, the PIC is translated laterally such that subsequent internal translations are made on target material which has not undergone laser damage.

The chamber lid is mounted via socket screws and a teflon gasket to prevent leaks and infiltration. Various 0.25 in. pipe thread ports are available on the top and various positions about the chamber. The ports typically have pressure transducers and inlet and exhaust fittings attached. The gas is fed into the chamber in a slow flow such that the plasma is not disturbed by any local gas dynamic effects as might be found in various gas assist nozzle systems. The pressure is monitored to insure that internal pressure is slightly above atmospheric, again to minimize infiltration. The side walls have opposing 3 in. by 4 in. window ports to facilitate emission, transmission, or interferometric diagnostics. An end window also permits simultaneous application of

multiple diagnostics. Figure 11 is a double exposure photograph of the PIC and plasma during an experiment. A major concern is damage to the NaCl window by the plasma and reflected laser beam. The 5 in. clearance between the window and target was a compromise between the above damage effect and the desire to use the PIC with a variety of laser systems. The window system has been redesigned with an internal gas jet applied to the window for cooling and to prevent oxide deposition. The system has recently been used to reduce window damage.

Figure 12 is the LBA intensity traces for the f/7 Cassegrain telescope focal volume. The beam is relatively symmetrical. The spot size is approximately 1.0 mm (average between the two traces) and the intensity profile appeared to be near-Gaussian at the focus. The results agree with the HeNe tracer system which also shows symmetry. The spectroscopic data demonstrated symmetrical behavior, further supporting the assumption of cylindrical symmetry.

3.3 Spectroscopy

The temperatures in excess of 10,000 K encountered in the plasma core render conventional temperature diagnostics ineffective. Spectroscopy, as adapted from astrophysics, is the primary tool used in the study of laboratory plasmas. Spectral emission and absorption behavior can be used to map local properties such as temperature and number density (pressure). The main assumption is local thermodynamic equilibrium as discussed in Chapter 2, without which the relationships between emission behavior and plasma parameters are unwieldy. Since the spectral behavior is dominated by electron interactions, the calculated

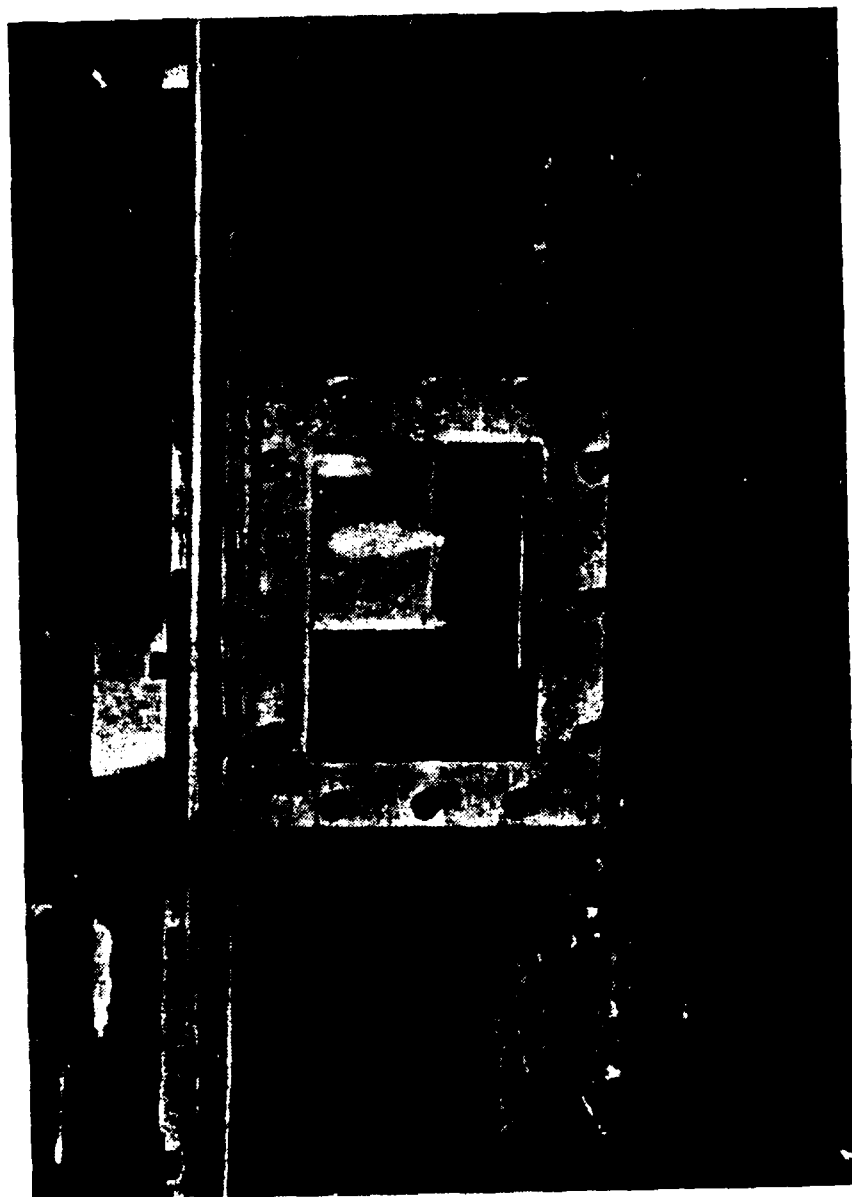


Figure 11 Double Exposure Photo of PIC and Plasma

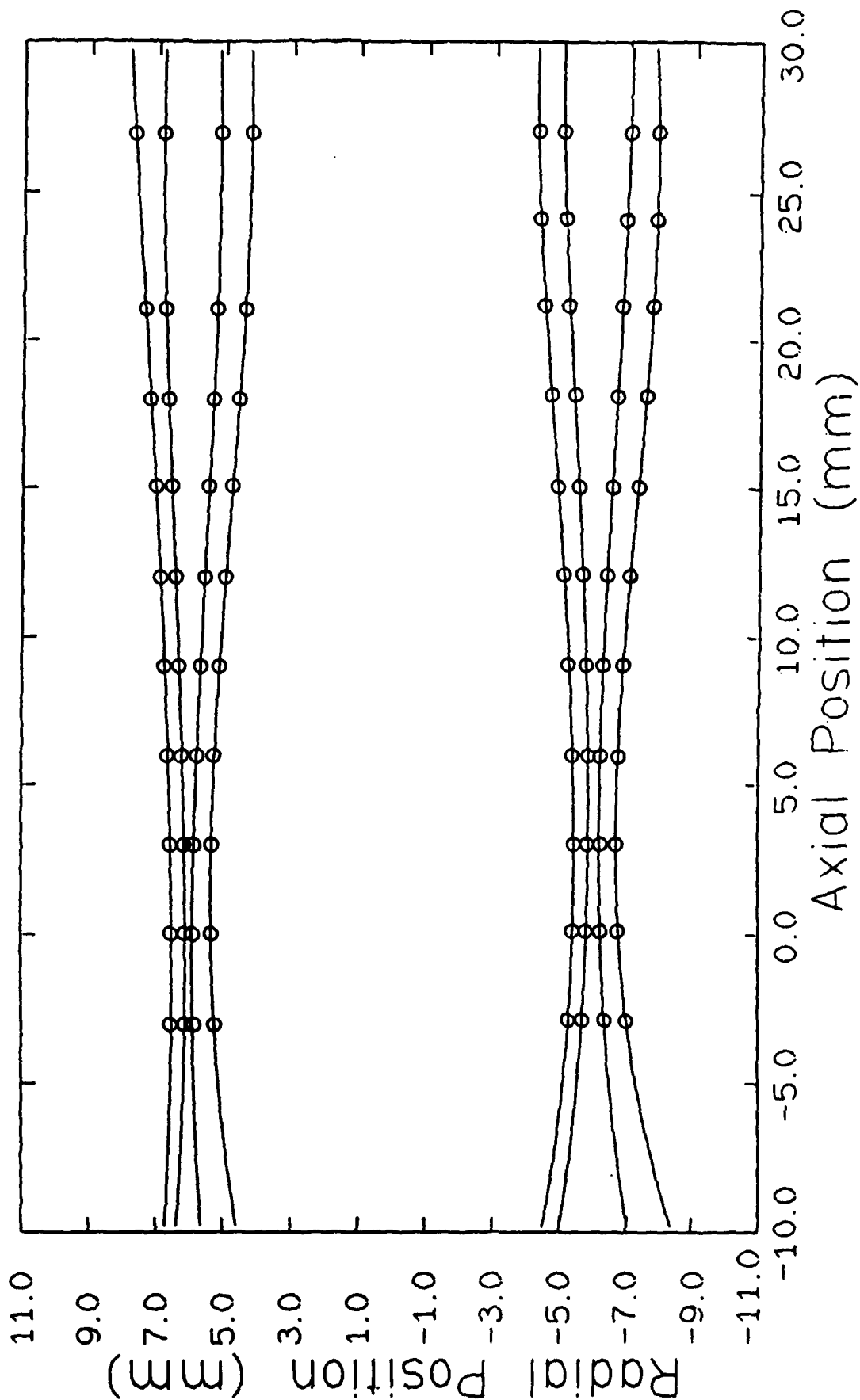


Figure 12 Intensity Profile of f/7 Cassegrain
Focal Volume used in PIC Experiments

parameters correspond to the electrons. The heavy particle temperatures must be determined independently with no reliable diagnostic techniques currently available. Instead, the heavy particle parameters are typically calculated from the measured electron distributions as will be discussed in Chapter 5. Fortunately the electron parameters dominate the laser plasma interaction physics associated with this investigation.

3.3.1 Review of the Techniques

Spectroscopy can be divided into two general categories, absolute and relative. Each type has been used successfully in the diagnostics of laboratory plasmas. Absolute techniques typically involve the measurement of a narrow spectral continuum band. The absolute emissive power ($\text{W}/\text{cm}^3\text{-sr}$) is calculated and compared to a calibrated source such as a tungsten ribbon lamp. By matching the emissive powers, the local electron temperature can be determined.

Henricksen, et al. [50] and Carlhoff, et al. [13] have successfully demonstrated absolute measurements of laser supported plasmas in pure gases. Henricksen measured a 10 angstrom band of Ar continuum centered at 626.5 nanometers. The region is isolated from line spectra to insure negligible self-absorption. Carlhoff similarly measured the intensity of a continuum band near 587.6 nanometers in helium. Both investigations reported peak temperatures approaching 15,000 K. The equipment needed for absolute measurements is relatively modest but inflexible due to the need of optical filters centered about the band of interest. The need to accurately account for the filter transmission function, calibration source fluctuation, and the optical transfer function in the above investigations can lead to significant error.

The other area of spectral diagnostics of interest are the relative techniques. Two spectral events, line and/or continuum, as mapped from the same elemental plasma volume, are used to determine local electron parameters. Key, et al. [51] and Mills [52] have used the relative intensity of two spectral lines in argon arc plasmas. Both studies used the 457.9 and 458.0 nanometer ArII lines. The upper energy level separation of the lines allowed the determination of temperatures approaching 15,000 K. The general rule is that the upper level energies of the line events should differ on the order of the electron temperature to be determined, i.e., in excess of 9,000 K. The 9,000 K figure is an arbitrary value.

As will be shown in Section 3.3.5 of this chapter, the line ratios are typically on the order of unity. The nature of the line intensity equation is that small fluctuations in the line ratio result in small fluctuations about the 9,000 K energy difference. Thus the energy difference should be on the order of the expected temperature field to minimize error. The lines mentioned above meet this requirement. The use of ionic argon lines in this temperature range at atmospheric pressures allow accurate measurements along the arc plasma centerline where the current density is a maximum. The remainder of the temperature field is extrapolated from the near-centerline behavior of the neighboring atomic line structure. The two studies above appear to be the best data to date.

Tsao and Pavelic [53] utilized the 415.8 and 425.9 nanometer atomic argon lines to determine electron temperature in an arc plasma. The peak temperatures below 10,000 K are expected as the energy difference

between the two lines is relatively small (2,000 to 3,000 K) leading to an underestimation in temperature. The small energy difference implies errors approaching 50 percent [44] for temperatures which actually exceed 10,000 K. Kobayashi and Suga [54] utilized the 430.01 nanometer ArI and 434.8 nm ArII line pair to determine the temperature in an arc plasma. Peak temperatures of 18,000 K were reported which appear high. It was not obvious whether the authors accounted for the more explicit dependence of subsequent ionization stage relationships on LTE. The lowering of the ionization potential also may have had an effect.

The ratio of a line to continuum event or continuum to continuum event can also be used. Generally, continuum to continuum errors are large even in the presence of LTE [33,44]. Line to continuum ratios have been used successfully at the University of Tennessee by Henricksen [55]. The technique was later abandoned as the hardware and software was developed for absolute measurements. Predicted errors for line to continuum diagnostics are slightly higher than the same as relative line techniques, ± 10 percent versus ± 3 percent, respectively [44]. Also under the pressure conditions present in this investigation LTE should prevail [55], minimizing the difference in error between the various techniques.

Other spectroscopic diagnostics generally involve the measurement of line broadening. The broadening mechanisms compete and make resolution of individual contributions difficult. Stark (pressure) and Doppler broadening dominate the plasma behavior at the temperatures and pressures encountered in this investigation. Most authors agree that Stark broadening dominates once the ionization exceeds a few percent.

Stark broadening is due to the forces exerted on the electrons by the neighboring heavy particles. The effect is a quadratic (sometimes linear) broadening of the emission line profile. The measured line width at half maximum is proportional to the electron number density. The technique has been used successfully in systems where the hydrogen Balmer series H_β was resolvable. Stark half widths could be incorporated in future work to measure the electron number density as a continuity check on temperature measurements. This study was unable to resolve the Balmer H_β line from the water content in the argon. It appears that a small percentage of hydrogen would need to be introduced to the flow chambers in future work.

Doppler broadening results in a Gaussian line profile which is difficult to resolve from the Stark effect. This is unfortunate as the Doppler half width is proportional to the heavy particle temperature and is the only diagnostic available for this purpose. Griem [57] presents a method of resolving Stark and Doppler effects via Voigt profiles. However, the non-ideal laboratory conditions and associated errors due to instrumental broadening made measurement of line widths to $\pm 0.25 \text{ \AA}$ a difficult task with the current apparatus and laboratory conditions.

To implement any line broadening diagnostic technique several precautions must be taken. First, broadening measurements are typically made on relatively low intensity glow discharge type events [43]. Extreme care should be taken in reducing the laser plasma intensity delivered to the detection equipment, more so than in the spectral mappings of this investigation. Background signals should be minimized which was not possible in all areas of this investigation. Secondly, a

means of accurately assessing the target responsivity and blooming characteristics using a resolution target standard would have to be implemented. Finally the optical transfer function of the imaging and filtering system would have to be determined as well as the spectrometer characteristics. Only when each of the above areas has been quantified can one begin to achieve the accuracy and resolution required for line broadening measurements.

3.3.2 Relative Diagnostics

Relative spectroscopic diagnostics have been utilized exclusively in this investigation for several reasons. First, the necessity of a calibration source in absolute methods requires a second set of measurements. The calibration run should be performed after each data set under identical optical conditions. The large number of experimental conditions to be investigated made the calibration unnecessarily costly. The successful studies using absolute techniques for two-dimensional plasma mappings [13,50] have invested a considerable amount of time and money into specialized hardware and software systems. The systems far out cost the system required for relative diagnostics. The main advantage of absolute diagnostics is that snapshot images of the entire plasma volume can be made. This makes for very smooth and uniform profiles in the reduced data. Relative diagnostics are more flexible in that multiple spectral events can be mapped in a one-dimensional plasma cross section. The trade off between absolute and relative diagnostics is a second spatial dimension versus a spectral dimension, respectively. It was decided that the spectral dimension was more important in the assessment of LTE.

Figures 13 and 14 show the strong atomic argon spectra resolvable in the pure argon plasmas. Since the upper energy level differences in atomic argon are small, relative line techniques are not accurate. Thus relative line to continuum techniques have been used in this study. The lines selected should be optically thin to minimize the effects of self-absorption. As mentioned previously, it has been shown that self-absorption even of the metastables is minimal in the 400 to 500 nm region of argon.

In the metallic plasma, the presence of aluminum vapor appears to push the system closer to LTE conditions. This is evidenced in Fig. 15 where the ionic argon lines have begun to appear. The bottom (solid) trace is the pure argon spectra of Fig. 14. The dashed curve is the aluminum-argon spectra. One notes the ArII lines at 428, 437, and 437.9 nm which are not observable in the pure argon results. However, the upper energy level differences of these lines are on the order of 30,000 K and thus cannot be used to determine temperature in this region.

The only aluminum structure observable was the strong resonant pair at 394.4 and 396.1 nm. The aluminum lines were observable only within a few mm of the target surface indicating that the plasma behavior is dominated by the argon species. This is consistent with the results of Ref. 12 wherein the plasma was found to have little metal vapor. The effect was attributed to the attenuated laser energy being insufficient to support vaporization although considerable melting was occurring. Also, in Ref. 14 it was noted that the metallic number density in the vacuum plasma was negligible after 1 μ s. The authors concluded that

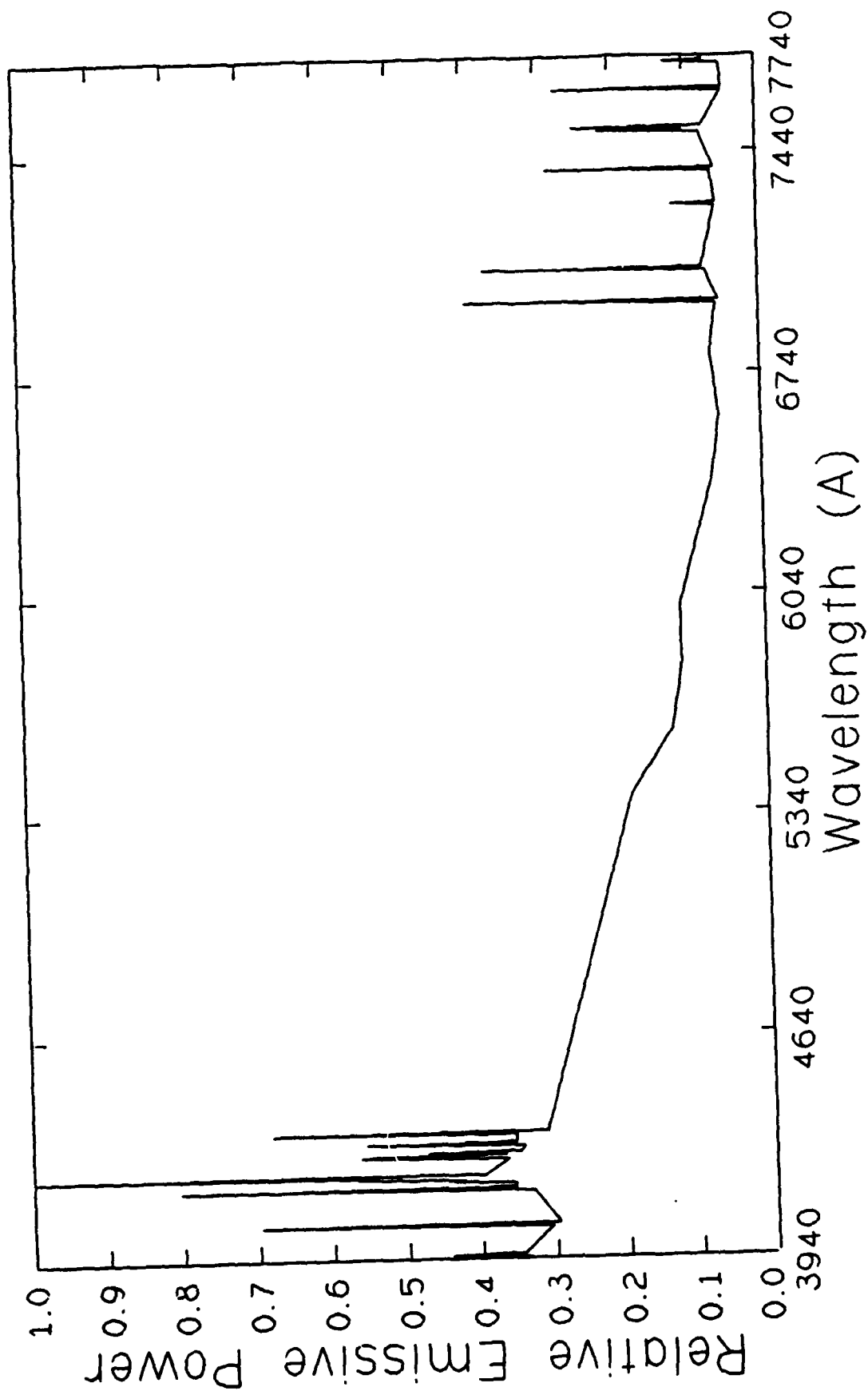


Figure 13 Pure Argon Spectra: 394 to 774 nm

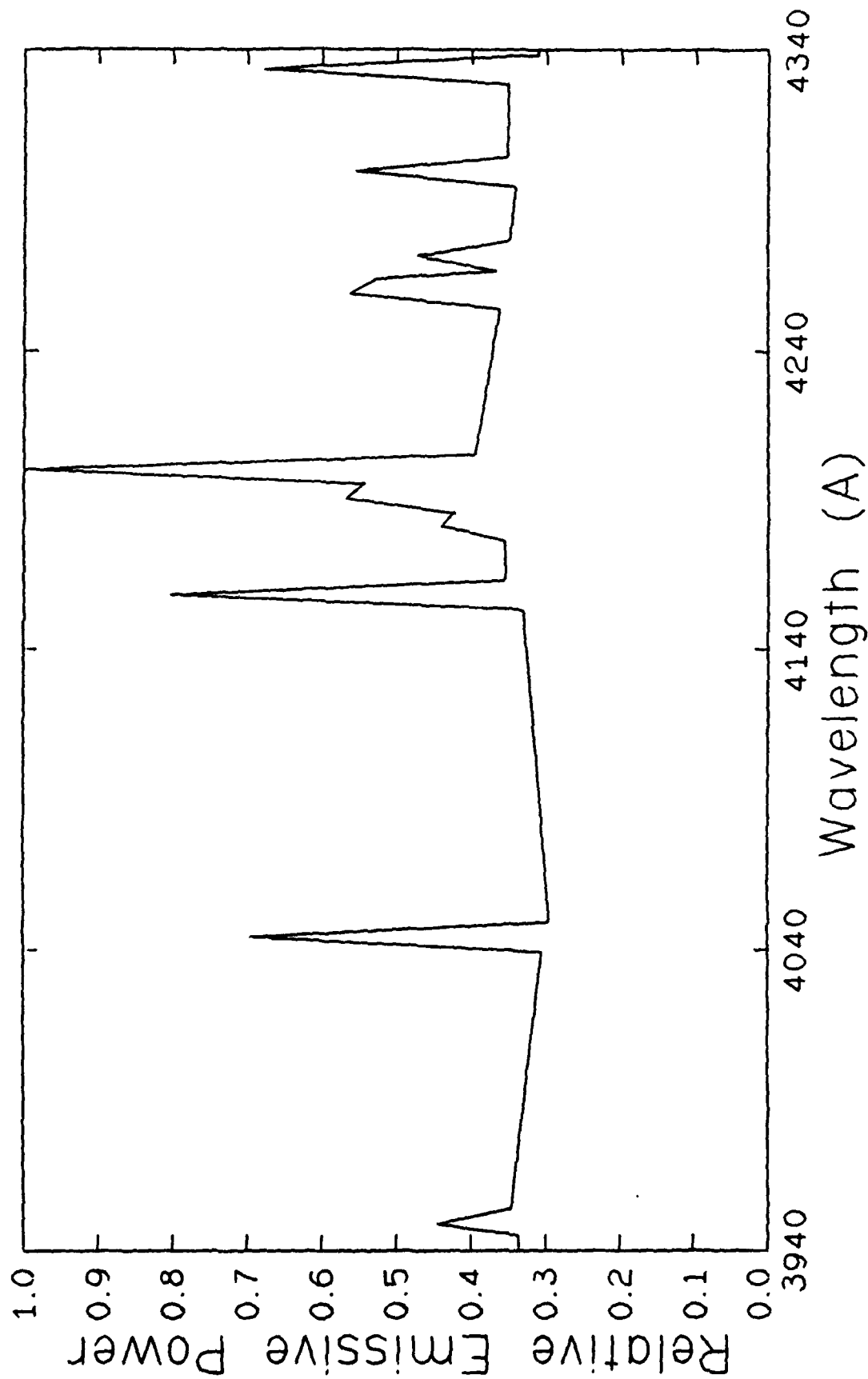


Figure 14 Pure Argon Spectra: 394 to 434 nm

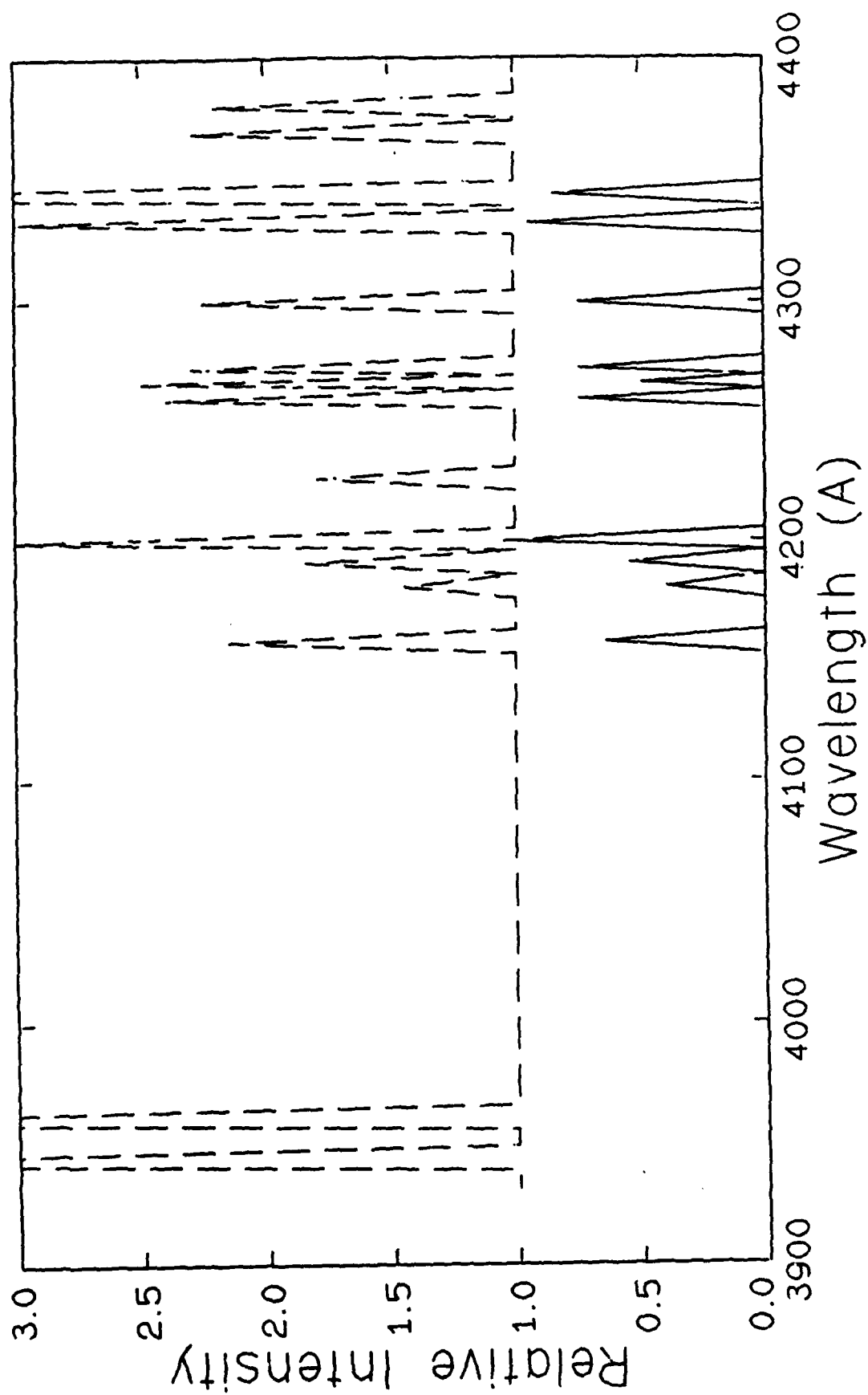


Figure 15 Aluminum and Argon Spectra: 390 to 440 nm

similar results would occur in non-vacuum atmospheres and plasma behavior would be dominated by the ambient species.

The line radiation resulting from bound-bound transitions is expressed via quantum physics as:

$$I_{\lambda} = \frac{A_{mn} h c g_m N}{4\pi\lambda Z_e} \exp(-E_m/T_e) \quad (3.2)$$

in $\text{W/cm}^3\text{-sr}$ where A_{mn} is the transition probability ($1/\text{s}$), h is Planck's constant, g_m the upper level degeneracy, E_m is the upper level energy, Z_e the electronic partition function, and N the atomic number density. Equation (3.2) is the result of quantum theory for radiative emission and absorption of a system as an electron transfers between energy levels.

Several authors have found the Kramers-Unsold theory adequately describes the argon continuum below 20,000 K [58]. The continuum emission consisting of free-free and free-bound transitions summed over internal energy levels yields

$$I_{C_{\lambda}} = 5.41 \times 10^{-46} c \Delta\lambda \bar{g} N_e^2 / (\lambda^2 T_e^{3/2}) \quad (3.1)$$

in $\text{W/cm}^2\text{-sr}$. c is the speed of light, \bar{g} the average Gaunt factor, N_e the electron number density, λ the center wavelength of the interval $\Delta\lambda$, and T_e the electron temperature. Equation (3.1) is a form of the Kramers-Unsold continuum theory [29,58]. Equation (3.1) was derived by comparing classical and quantum radiation theory. At long wavelengths in the infrared quantum and classical theory agree. Above

some frequency, ν_0 , the spectral nature of quantum theory differs significantly from classical theory. By mapping the two theories in this region, it was shown that the energy of the quantum line events is equal to the energy of the surrounding spectrum as predicted by classical theory. Thus classical theory was shown to accurately predict continuum radiation. Classical theory is particularly valid for integrated measurements over a large wavelength interval.

Using the value of $g = 2.2$ from Oettinger [59], g_m and A_m for the 415.8 nm ArI line from the NBS Reference Book [60] and Z_e as derived by Tan [61], Eqns. (3.1) and (3.2) are combined to yield

$$I_\lambda/I_c = 1.3357 \times 10^{20} (NT_e^{1/2}/N_e^2) \Delta\lambda \quad (3.3)$$

Assuming LTE at one atmosphere, N and N_e are functions of T_e only and Eqn. (3.3) can be reduced to a function of T_e . Figure 16 is the ratio I_λ/I_c as a function of T_e for a continuum band ($\Delta\lambda$) of 10 Å for the 415.86, 420.0, and 696.5 nm ArI lines. The ratio rapidly decreases as T_e approaches 17,000 K with a minimum at approximately 17,500 K when ArII contributions to the number density become significant.

In the calculation of temperature from relative line intensities, Eqn. (3.2) can again be applied to each line resulting in

$$\frac{I_{\lambda_1}}{I_{\lambda_2}} = \frac{A_1 g_1 \lambda_2}{A_2 g_2 \lambda_1} \exp \left[\frac{E_2 - E_1}{kT_e} \right] \quad (3.4)$$

which can be rearranged:

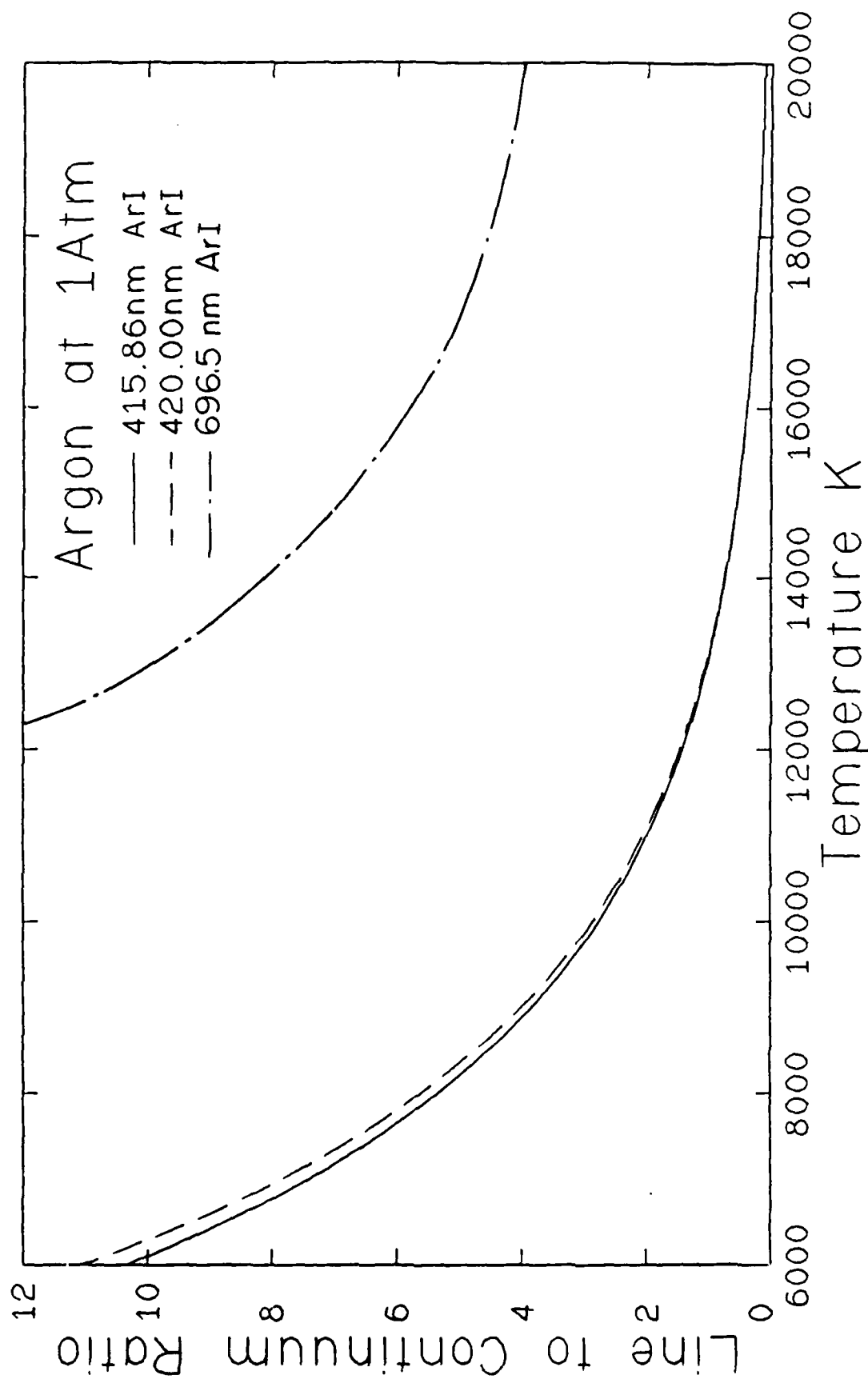


Figure 16 Line to Continuum Ratio

AD-A174 579

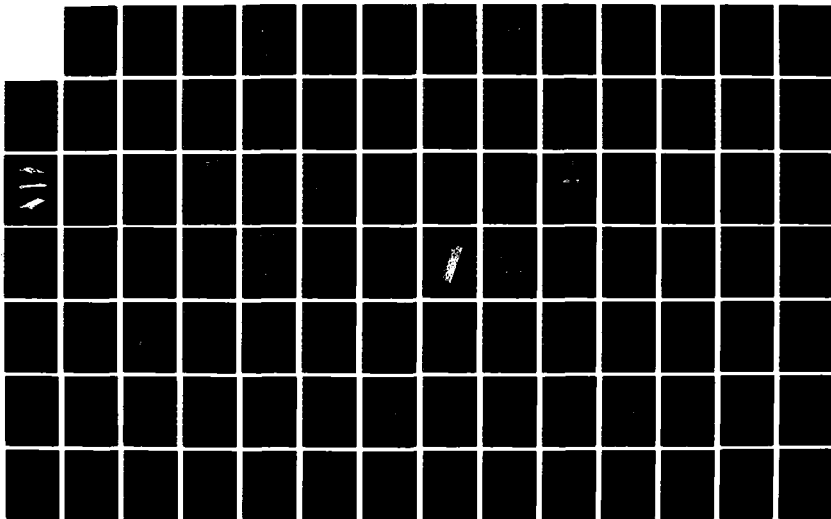
THE ROLE OF THE PLASMA DURING LASER-GAS LASER-METAL
INTERACTIONS (U) ILLINOIS UNIV AT URBANA DEPT OF
MECHANICAL AND INDUSTRIAL ENG T J ROCKSTROH ET AL

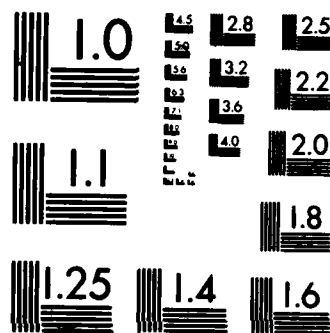
2/3

UNCLASSIFIED

13 OCT 86 UILU-ENG-86-4811 AFOSR-TR-86-1852 F/G 28/5

NL





MICROCOPY RESOLUTION TEST CHART
NATIONAL BUREAU OF STANDARDS-1963-A

$$T_e = (E_2 - E_1) / k_B \ln [I_{\lambda_1} A_2 g_{2\lambda_1} / (I_{\lambda_2} A_1 g_{1\lambda_2})] \quad (3.5)$$

As mentioned earlier, the energy difference, $E_2 - E_1$, must be on the order of T_e , i.e., 0.9 eV or 10,000 K) as the denominator of Eqn. (3.5) typically does not vary much about unity. The values of A_i vary from author to author, however the variation from similar sources should be offsetting in Eqn. (3.4). Figure 17 shows the ratio of the 457.9 and 458.9 nm ArII lines. No ArI spectra was resolvable near the 457.9 nm and 458.9 nm pair. Thus two separate measurements are required if this technique is to be used.

3.3.3 Spectroscopic Equipment

The spectroscopic equipment chosen for this investigation was an EG&G PARC Optical Multichannel Analyzer (OMA) III. The OMA system consists of a console (CPU), detector controller, two-dimensional vidicon detector, monochromator, optical system, and translation stages. Figure 18 is a schematic of the system configuration.

The console is used to set up the scanning sequence of the detector and acquire data in various modes. The console also stores the data via a 150 K floppy disk and/or a 15M Winchester hard disk. The detector controller is a 16-bit parallel peripheral device which accepts the scanning code from the console and derives the vidicon scanning sequence.

The detector is a silicon intensified target (SIT) detector, 500 by 512 pixels. The pixels are 25 by 3 micrometers with a total active area of 12.2 by 12.5 mm. The spectral range is 365 to 800 nm and the

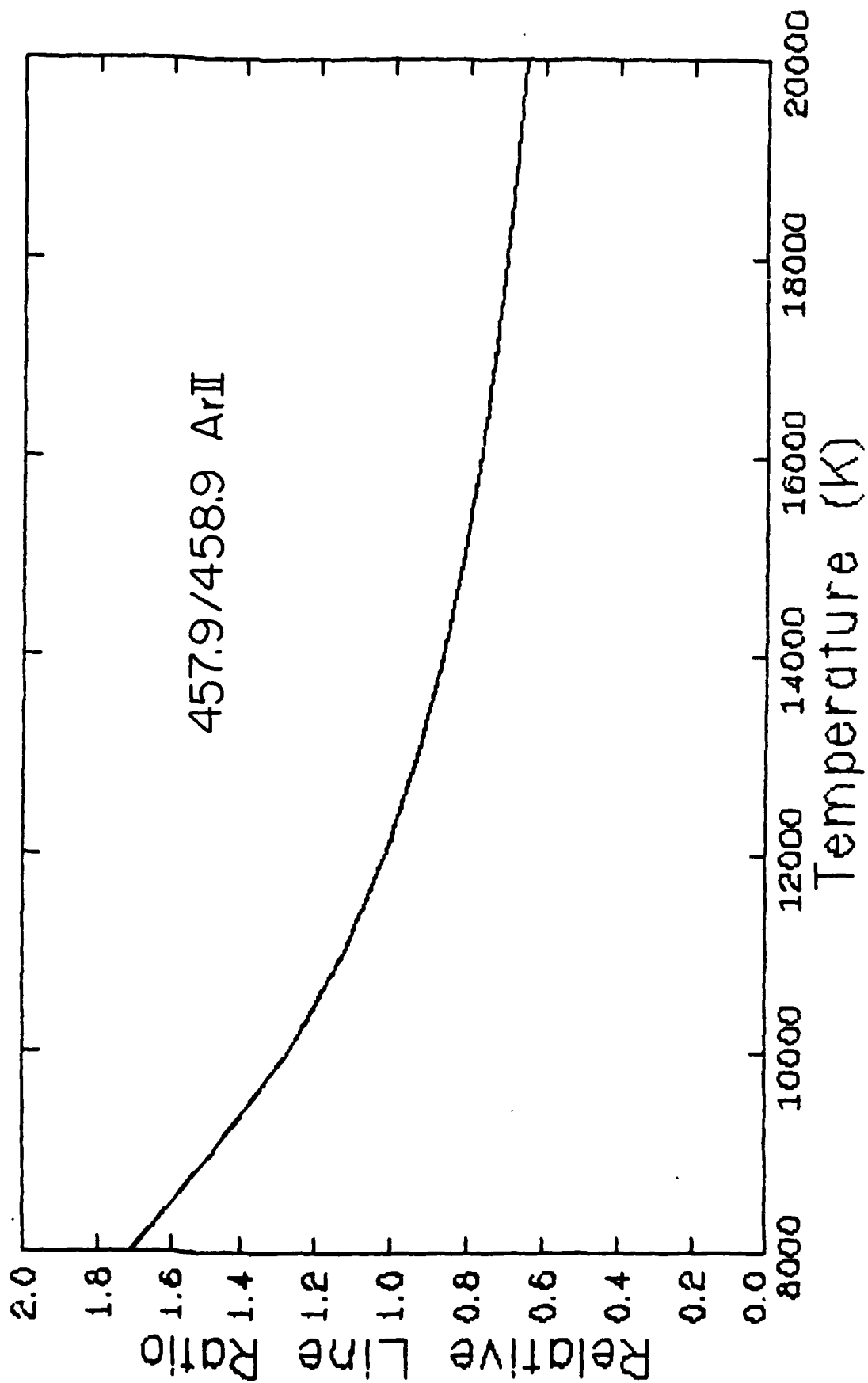


Figure 17 Relative ArII Line Ratio

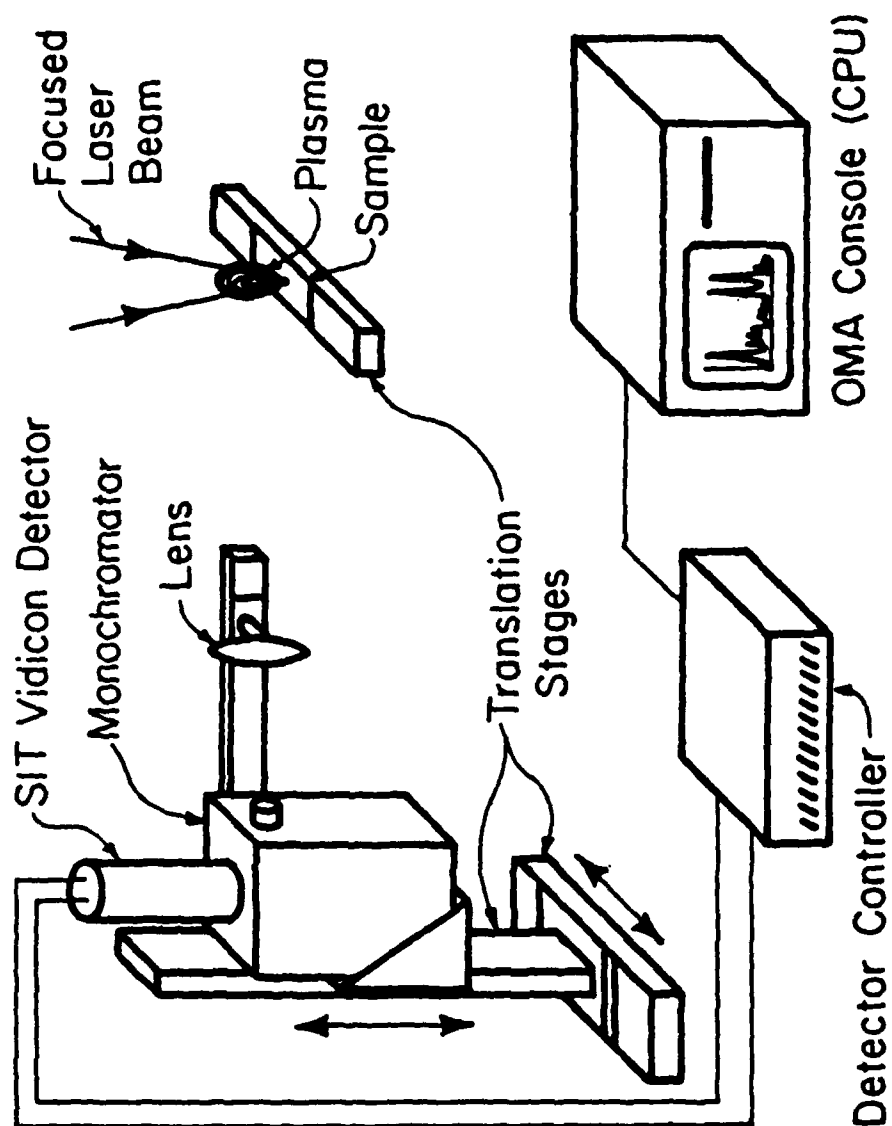


Figure 18 Optical Multichannel Analyzer (OMA) Schematic

detector has been coated with a UV scintillator which lowers the range to 200 nm. The sensitivity is uniform over the active area to ± 10 percent. The linearity is ± 2 percent but a function of sensitivity. The sensitivity is 10 to 20 photons per count and the detector response was found to be linear as long as the counts per scan were below 1000. The detector can also be gated down to 40 ns if temporal resolution is desired. The monochromator is utilized in a spectrograph configuration. Thus the two-dimensions of the detector correspond to the spatial extent of the entrance slit length and spectral spread of the diffraction grating. The monochromator is a 0.32 in. Czerny-Turner configuration with kinematically mounted components such that the system can be mounted in any orientation. For the majority of experiments in this investigation, a 1200 line/mm holographic grating was used. This results in a resolution of .5 to .6 Å at the detector face.

3.3.4 Data Acquisition

As was shown in Fig. 18, the monochromator is aligned vertically, that is with the entrance slit horizontal. The plasma event in all cases is vertical to minimize the effects of buoyancy. The plasma is imaged onto the horizontal entrance slit as shown in Fig. 19. By dividing the detector spatial dimension into N individual tracks, the entrance slit and hence the plasma radial dimension is effectively divided into N elements. The minimum number of pixels in a given track was five. This number corresponds to the minimum number of pixels which must be grouped together to minimize the effect of thermal blooming at the detector surface. This dimension is the means of calculating the

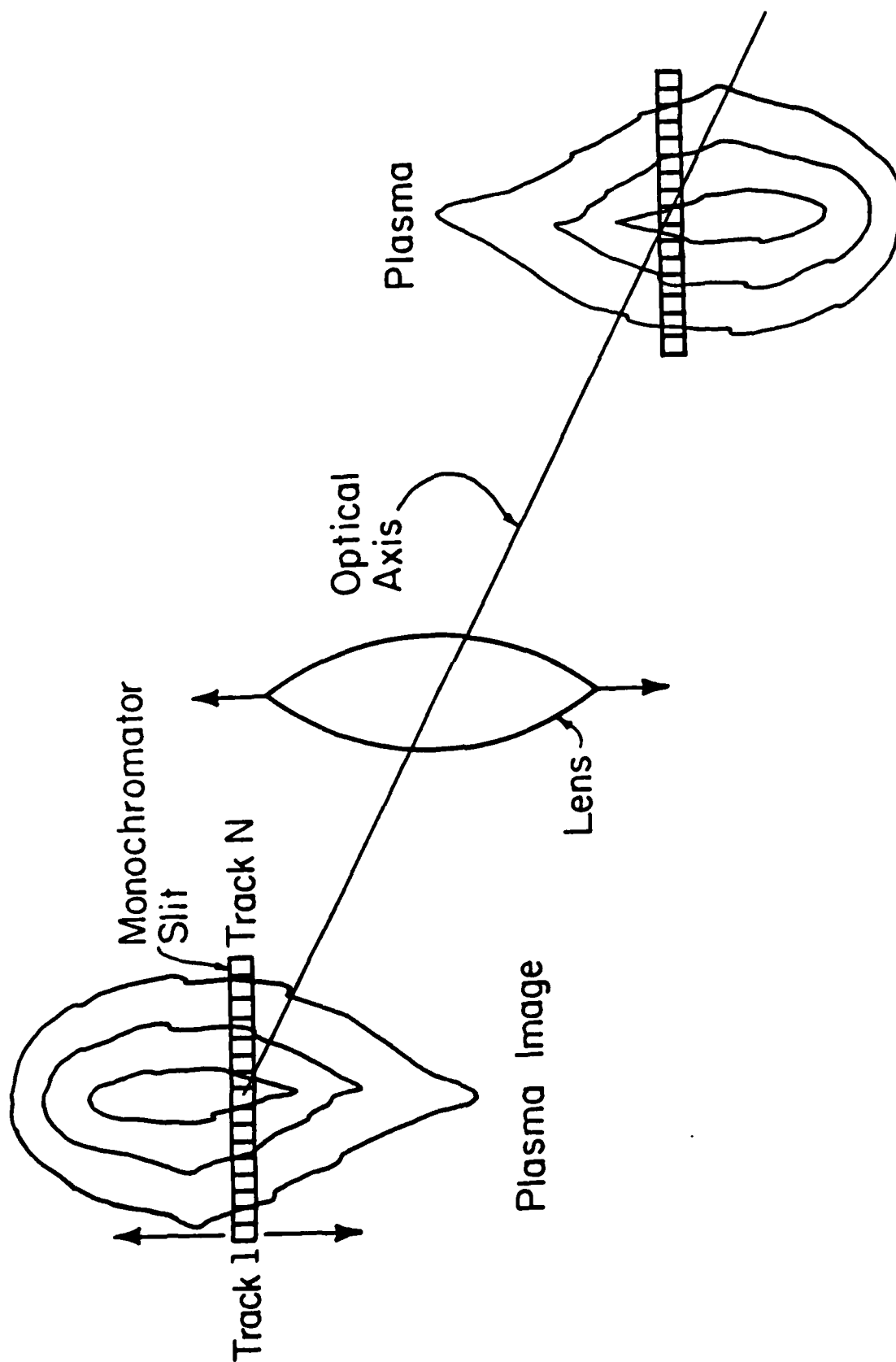


Figure 19 Plasma Imaging Technique

radial dimension of the plasma volume. For example, 5 elements out of 500 elements corresponds to the radial increment. Since the 500 dimension is 12.2 mm wide, the radial increment at the detector is: $5/500 \times 12.2 \text{ mm} = 0.122 \text{ mm}$.

To calculate the magnification of the monochromator, one follows the guidelines of Lerner and Thevenon [62]. Assuming the optical system $f/\#$ was matched to the monochromator $f/\#$ at the given wavelength [62], the magnification of the monochromator will be on the order of 1 to 1.1 times. For example, at the 415.8 nm ArI line, the monochromator is an $f/4.96$ system. Thus the radial increment at the entrance slit is $\frac{0.122 \text{ mm}}{1.1} = .111 \text{ mm}$. The actual radial increment at the plasma is this value divided by the magnification of the optical system. From Fig. 19 the optical magnification is $-S_o/S_i$. If this value is $1/3$, then the actual increment is $0.111/(1/3) = 0.333 \text{ mm}$. When designing an experiment, one is constrained to match the monochromator $f/\#$ at the given wavelength and ensure that the optical magnification is such that the plasma image underfills the entrance slit length. The axial increment is somewhat easier to calculate being the slit width divided by the optical magnification. Thus for the above system with a 0.1 mm slit width, the axial dimension is 0.3 mm, as shown in Fig. 19.

Once the detector has been divided into N tracks, each track is spectrally spread across the other detector dimension. The result is a multitrack spectral data set as shown in Fig. 20. The x-axis corresponds to wavelength, y-axis is radial position, and z-axis intensity ($\text{W/cm}^2 - \text{sr}$). One sees that the plasma emission is "hotter" near the centerline, as expected, and the continuum has also increased in this region.

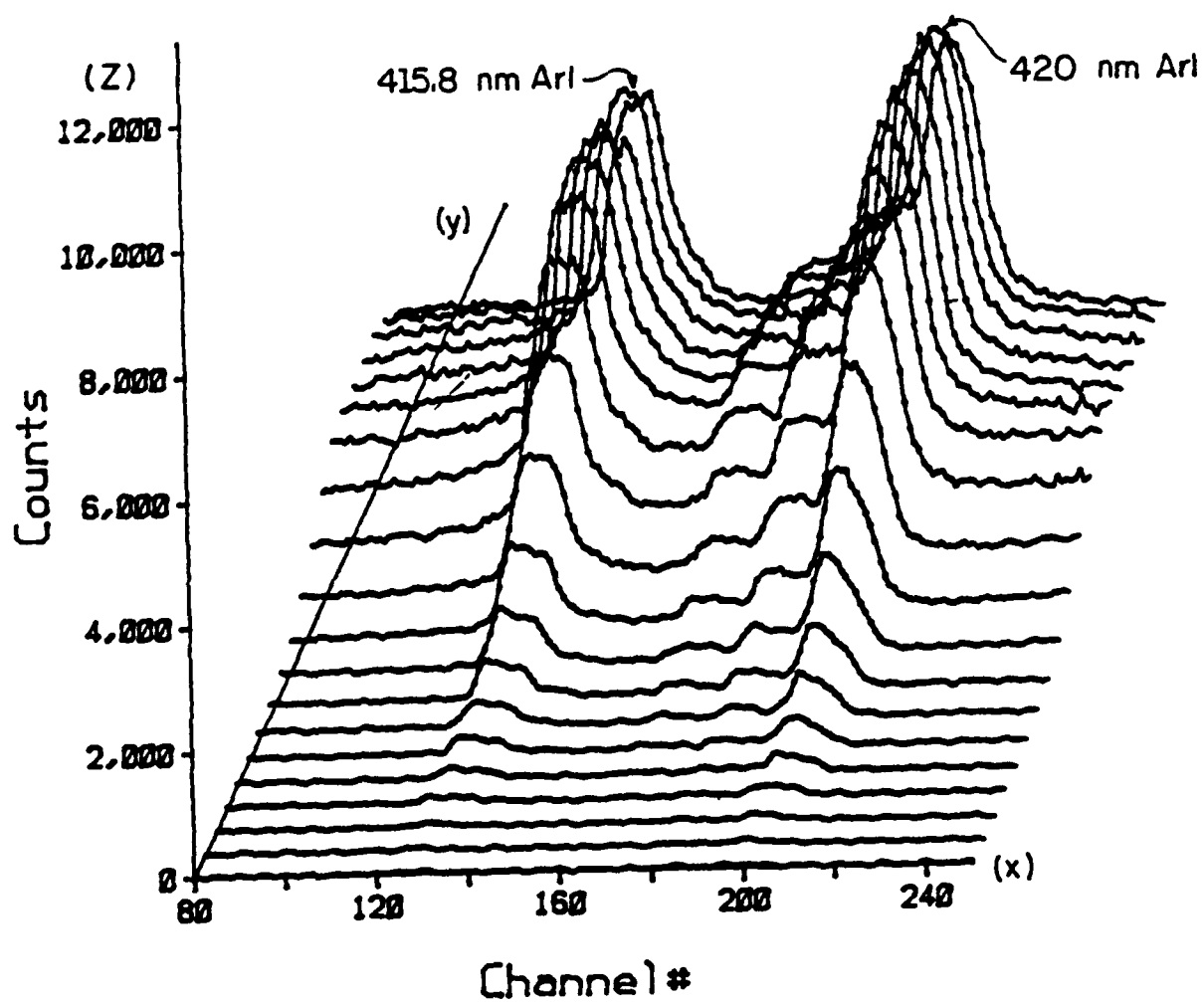


Figure 20 Example of a Multitrack Data Set

3.3.4.1 Instrument Operation

The operation of the OMA will now be discussed. Data can be acquired in a number of modes. Initially, the plasma is scanned in the live mode where the display is updated continuously. The refresh rate is determined by the total number of elements scanned on the detector. Typically, a large single area (track) is scanned initially to find the plasma. The horizontal translation stage is moved (Fig. 18) to accomplish this. Once the plasma has been found the detector is divided into larger numbers of tracks with the horizontal stage being moved to again center the plasma. Plasma centering is not particularly critical but the plasma should be maintained close to the center to minimize the effect of detector response which drops off rapidly in the outer 10 percent regions.

Once the number of tracks has been reduced to the desired size or minimum (5 elements) the intensity of the plasma is monitored. The detector can be damaged at intensities in excess of 14,000 counts which has been shown to easily occur in laser supported plasmas. The local intensity is reduced by reducing the channel dwell time (20 μ s minimum), the reduction of the slit width, and the addition of neutral density filters. Filters with optical densities ranging from 0.5 to 5.0 were used in this investigation depending on the optical system and laser power. The plasmas investigated in this report are relatively strong emitters compared to the events the OMA was designed to monitor. Thus another possibility for intensity reduction is the addition of an aperture at the imaging lens. The aperture will change the effective

f/# of the optical system but will affect relative calculations minimally at the detector face.

In this investigation, the data was accumulated over ten to twenty consecutive scans per axial location. Thus, the intensity had to be reduced to less than 1000 counts peak per scan to insure linearity in the summation. The accumulated scans were selected to minimize local fluctuations in the plasmas. Fluctuations were seen in the live mode to be minimal in most plasmas and were at best a random type feature. Once the given radial scanned been acquired, the vertical translation stage (Fig. 18) was incremented to the next highest location, Δz typically 1 to 3 mm.

As mentioned previously, finding the plasma is the most difficult process. Once the focus position of the laser is known, a spectral lamp is aligned in this region with the laser axis. The optical/monochromator system is then adjusted via the lamp. The vertical location of the system is aligned to a point where the plasma is known to exist. Thus, only horizontal adjustments of the optical/monochromator system should be necessary to find the plasma. Once the plasma was found, absolute vertical scaling is performed. In the pure gas, a HeNe laser is aligned horizontally through the focus in the PIFC and through the optical/monochromator system. Once the plasma is initiated, the optical system is translated downward (upstream) until the plasma emission ceases, forming a datum relative to the focus. In the metallic plasmas, a HeNe laser beam is split as it intersects the target parallel to the surface. The transmitted beam is used to align the optical system and the target surface forms the datum. A brief

document on the data acquisition procedures can be found in the laser lab (ME). "Guidelines to be Used for Implementing the OMA III System into an Experiment," is meant to be used in conjunction with the various OMA manuals.

3.3.5 Data Reduction

Once the multitrack data (Fig. 20) has been stored the data must be reduced via Eqns. (3.3) or (3.4). The data that has been stored includes whatever background radiation there is in the laboratory. This effect can be accounted for by acquiring data without the plasma present. Typically one background file is required for each set of plasma scans as the variation in the background signal is small along the plasma axis. The background file will also account for any dark signal and/or "burned" elements which may be present on the detector face. The file is then subtracted from each of the data files via the "Curve Calculations" mode in the OMA III console. The resulting file is now pure plasma intensity data ($\text{W/cm}^2 \cdot \text{sr}$).

Equation (3.2) corresponds to the emission at a pure frequency. In the case of a laboratory plasma, the energy has been spread out into a profile. There has been much debate as to whether the peak or integrated intensity values are applicable in the analysis of temperature. The peak intensity calculations generally result in lower temperatures since it has to be ratioed to a single element continuum value. The procedure has been used primarily in attempts to reduce the amount of data processing required in attempts to make real-time temperature measurement systems. The integrated intensity of the line

profile is the figure of merit which corresponds to the theoretical value of Eqn. (3.2). Since real-time data reduction is not possible with the current OMA software, the integrated profiles have been used throughout this investigation.

To integrate the line profile the "Data Utilities" - "Channel Profile" routine on the OMA has been used. The given file is analyzed and a starting and ending wavelength is selected. The utility then sums the intensity values from start to end wavelength, inclusive. This value is now proportional to the total line and continuum energy in this range and the continuum contribution must be subtracted for use in Eqns. (3.3) or (3.4). To do so, the continuum adjacent to the line profile is integrated over an equivalent number of channels (wavelength). The continuum file can then be subtracted from the line/continuum file, yielding the approximate line term. Approximation is used here as ideally one would attempt to subtract the actual continuum, which is not possible in the current OMA III software. In older OMA systems when integrating line profiles, the outermost edges of the band were trapezoidally fit to calculate the actual continuum. This feature should be included in future OMA software releases. The net result is typically a slight underestimation of the continuum in the red wing and overestimation in the blue wing.

Now that the actual line and continuum file are ready it should be noted that the values are line-of-sight integrated intensity ($\text{W}/\text{cm}^2 \text{ - sr}$) values. To accurately use the data, it must be deconvoluted into point emissive powers ($\text{W}/\text{cm}^3 \text{ - sr}$). This is accomplished via the Abel inversion, as shown in Fig. 21. A numerical inversion code was

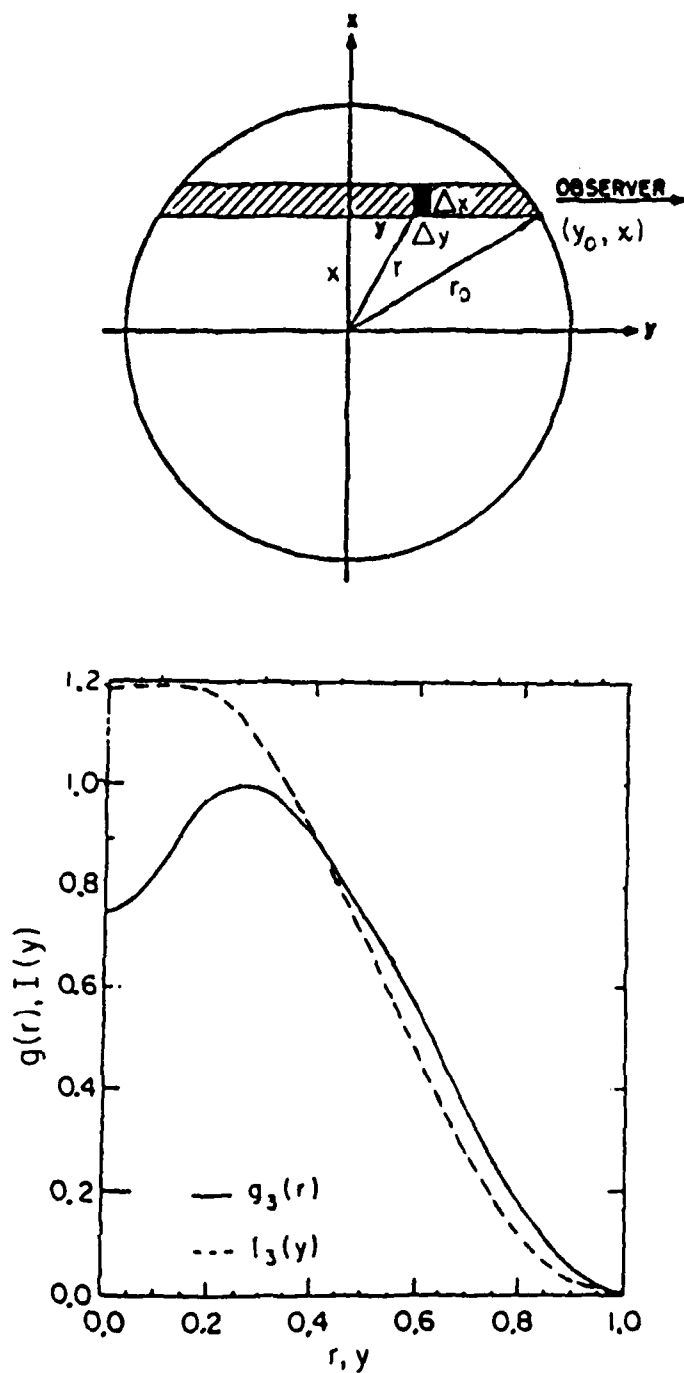


Figure 21 Diagram of Abel Inversion Process

developed after the work of Cremers and Birkebak [63]. The code listing as well as a brief review of the extensive work in this area is presented in Appendix A.

A flow chart of the numerical Abel inversion code is shown in Fig. 22. The line of sight intensity data is read into the code via a formatted data file. The radial positions of a given scan (1 axial location) are normalized to unity for ease in later curve fitting and analysis. The code then curve fits the data via cubic splines, the number of knots being determined by the number of data points. Typically 7 to 20 data points on a given radius were resolvable which were subsequently cubic spline fit with three, four, or five knots. The data was relatively smooth and cubic splines were found to adequately follow the trends. The cubic splines are analyzed at the data points and an average error file is made. Now that the cubic coefficients are available, the inversion is begun.

The Abel integral is of the form (see APPENDIX A):

$$I(y) = 2 \int_y^1 \epsilon(r) r (r^2 - y^2)^{-1/2} dr \quad (3.6)$$

where $I(y)$ is the integrated intensity ($W/m^2 - sr$), $\epsilon(r)$ is the emissive power ($W/m^3 - sr$), and y and r as shown in Fig. 21. The integral can be inverted yielding:

$$\epsilon(r) = \frac{1}{\pi} \int_r^1 \frac{dI(y)}{dy} (y^2 - r^2)^{-1/2} dy \quad (3.7)$$

If $I(y)$ has been fit to the form:

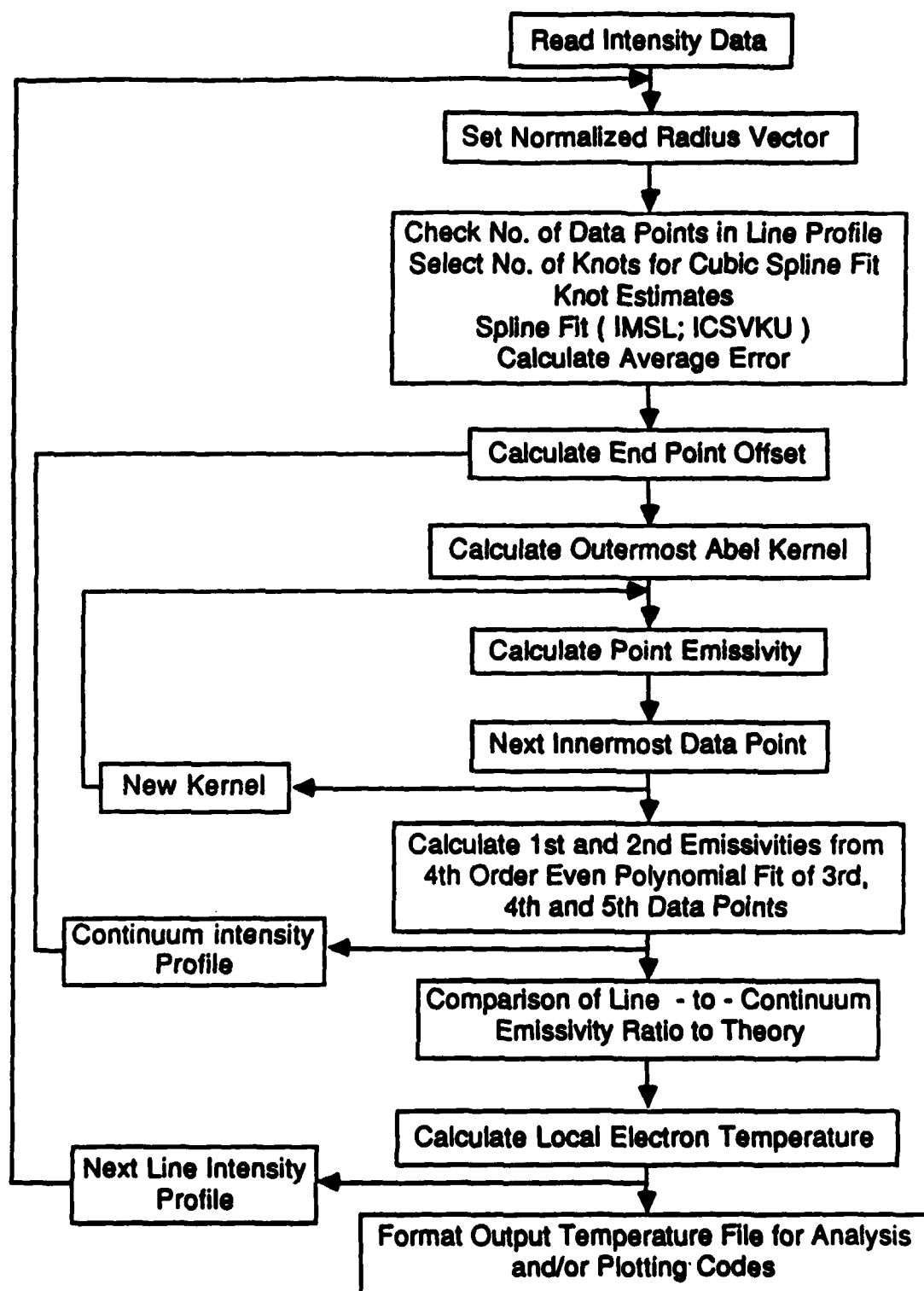


Figure 22 Abel Inversion Code: Flowchart

$$I(y) = A + By + Cy^2 + Dy^3 \quad (3.8)$$

then differentiating $I(y)$ and substituting into Eqn. (3.7) yields:

$$\epsilon(r) = \frac{1}{\pi} \int_r^1 \frac{B + 2Cy + 3Dy^2}{\sqrt{y^2 - r^2}} dy \quad (3.9)$$

Where the integration begins at the radial point r and proceeds to the outermost radius in this case normalized to unity. The equation is a simple integral easily evaluated analytically on the computer. The derivation assumes the outermost intensity to be zero which is typically not the case in experiment. To account for this effect the finite end value of a given scan is extrapolated linearly to zero at a fictitious radial point at $1 + \Delta r$. The slope of the resulting triangle is then integrated yielding a DC offset which is added to Eqn. (3.9) at all points.

The advantage of the above evaluation, outside-in versus inside-out is that inversion errors are carried over to the next calculation in diminishing margins. This makes the inversion less error-prone compared to previous matrix and numerical techniques. Since the inversion is analytical, data at fictitious points in between real data can be evaluated. The evaluation does not "blow-up" as easily at the centerline and can invert flattened centerline profiles, typical of laboratory plasmas. To account for symmetry at the centerline, the first two inverted data points are extrapolated from a fourth order even polynomial curve fit of the third, fourth and fifth inverted points. This

process should occur in the intensity data, but circumvents the possibility of centerline "blowup" when performed on the emissive power profile.

A typical error assessment of a radial profile is shown in Fig. 23. The error was analyzed on the basis of a ± 10 percent error in the measured intensities. Since the line and continuum are measured adjacent to one another, one would expect the \pm local error to be in the same direction. This type of error resulted in a total temperature error of less than 1 percent throughout any given radial profile. This would be expected if indeed the Abel inversion process was working properly.

The other major source of error would be detector non-linearity. The line events, being relatively strong compared to the continuum, would affect the detector response over the accumulation of several scans. This would bias the total line intensity low which would result in higher calculated plasma temperatures. Thus for the error analysis shown in Fig. 23 the line intensity was varied ± 10 percent with the continuum held constant. The result is that a maximum error of 3.3 percent is seen at the centerline with a decreasing calculated error at larger radial distances. This is typical of errors seen in other studies [51] except that the outermost temperatures have larger errors due to the local temperature by approaching the sub 10,000 K range. Thus a conservative error of ± 4 percent was chosen and applied to all the temperature fields that will be presented in Chapter 4.

Nearly all Abel inversion techniques assume circular symmetry of the intensity data. This was found to be the case in the majority of

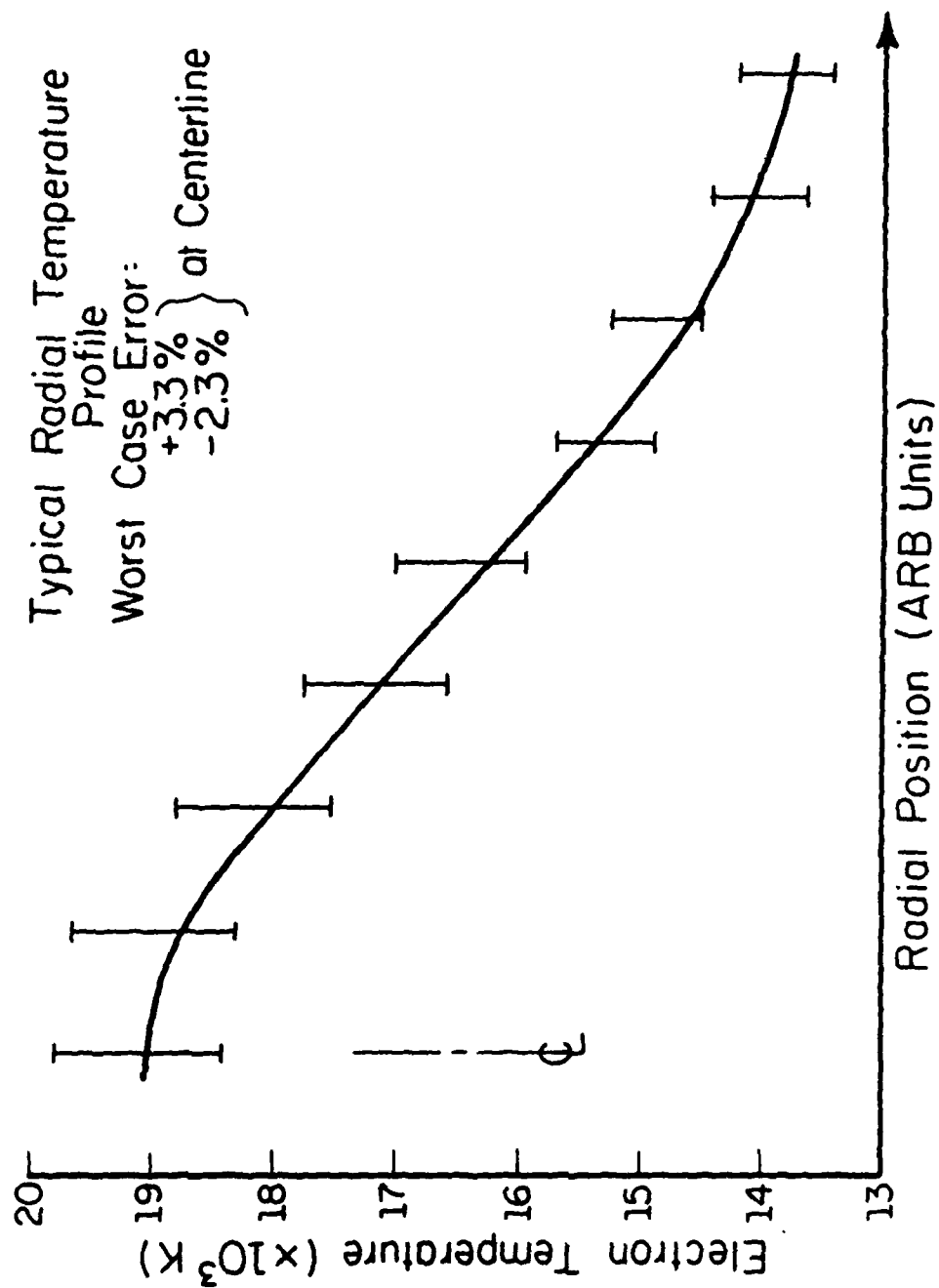


Figure 23 Radial Dependent Error Analysis of Abel Inversion

the plasmas in this investigation. Figure 24 shows the integrated line profile of the 415.8 nm ARI line as taken from Fig. 20 using the "Curve Calculations" and "Channel Profile" utilities of the OMA. Once the line or line and continuum pair has been inverted the ratio of the two signals is compared to the ratio as calculated in Eqns. (3.3) or (3.4). The ratios have been curve fit and the correct spline segment for the given ratio is applied to calculate temperature. The temperature output file is formatted for subsequent use in global property analysis and/or plotting.

The absorption code flow chart shown in Fig. 25, calculates the net power absorbed as the focussed laser beam propagates through the measured plasma temperature field. The properties of beam refraction and radiated power are also calculated. The code listing is presented in APPENDIX B.

The absorption code reads the temperature file which includes spatial and datum dimensions, laser power, and laser beam geometry. Once the beam geometry is determined, currently $f/7$ or $f/2.4$ TEM₀₁*, the beam cross-section is broken into twenty rays. The rays are propagated at increasing angles into the plasma, initially directed at some radial position offset from the laser axis at the focus. In the case of the pure gas analysis the rays are mirrored past the focus to account for downstream absorption. Each ray across the profile is weighted by a full Gaussian with the first and twentieth rays corresponding to the $1/e$ -points. The Gaussian profile arises from the nature of the beam and the fact that the absorption coefficient operates on intensity, not power. The Gaussian weights are summed prior to entering the plasma

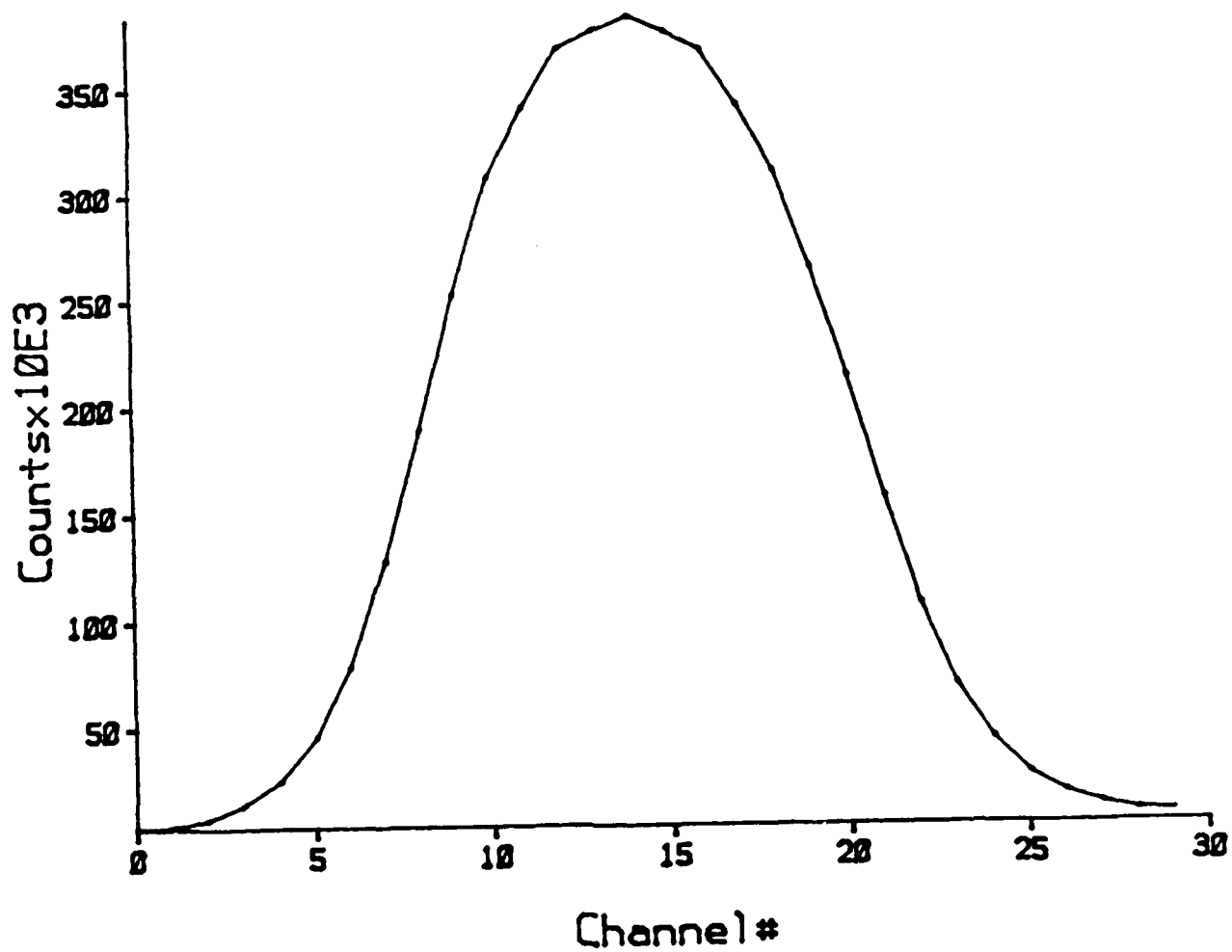


Figure 24 Example of an Integrated Line Profile

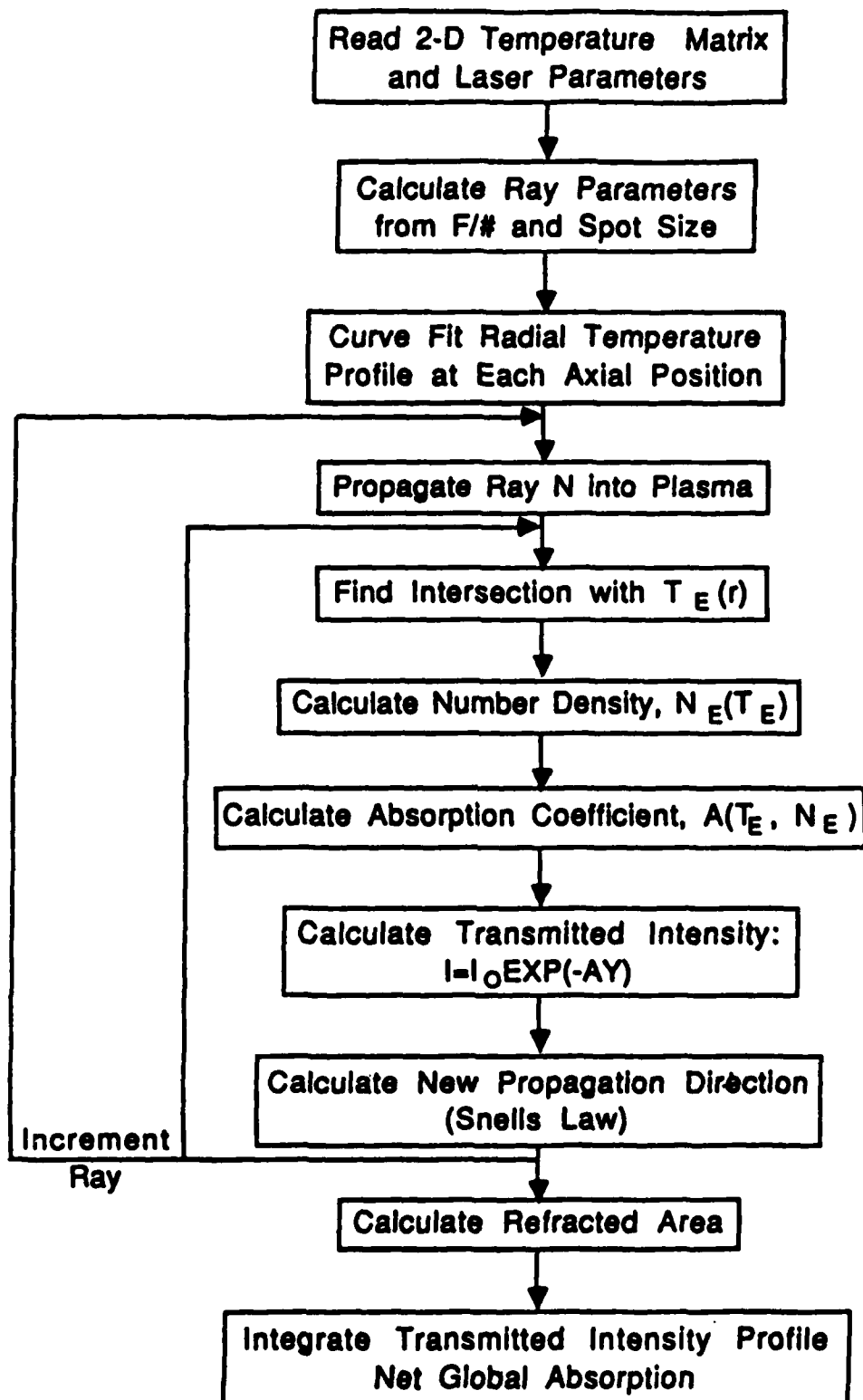


Figure 25 Transport Code: Flowchart

volume, being proportional to the incident power. As the ray bundle intersects the first axial position of the plasma the radial temperature profile is cubic spline curve fit. The radial location of each ray is calculated from geometrical optics and the local ray temperature is evaluated. The local electron number density is calculated from the local temperature [27]. The local absorption coefficient is calculated after the work of Wheeler [30] and Stallcop [31] as was discussed in Chapter 2. The local absorption is calculated using Eqn. (2.12) where Δz corresponds to the optical path length through the experimental cell size. When the rays have been propagated through the entire plasma volume, the attenuated ray weights are summed which are proportional to the transmitted laser power. The ratio of the difference between input and output summations to the input summation is the percentage of incident power absorbed.

A study was performed to assess the effect of refraction and datum errors. A datum shift of ± 2 mm typically changed the net absorption results by less than ± 5 percent. This type of error magnitude has been reported elsewhere [23]. When refraction of all rays was taken into account, the difference in absorption with respect to the straight-line geometrical ray trace was ± 0.5 percent, with a maximum error of $+1.1$ percent. However, beam refraction will be shown to be a non-negligible effect in metallic plasmas. The beam refraction results in a larger spot size which greatly affects target transport phenomena. Thus to include this effect, the beam refraction of the outermost ray is accounted for. Since the experimental axial data increments are larger and, in general, the radial temperature gradients are large with respect

to axial gradients, the radial index of refraction should have the greatest effect. Again, this has been seen in this effort and elsewhere [23].

Figure 26 shows the geometry under consideration. The twentieth ray is of concern and hence a twenty-first temperature point is linearly extrapolated from the nineteenth and twentieth points. The index of refraction at T_{19} and T_{20} (last two ray locations) is calculated after Cheng and Casperson [64]. Snell's law is used to calculate the new propagation direction to the next cell. Since the compliment of the incident angle is of concern, Snell's law in the radial direction reduces to:

$$n_{19} \sin(90-\beta) = n_{20} \sin(90-\beta')$$

or

$$\beta' = \cos^{-1} \left[\frac{n_{19}}{n_{20}} \cos(\beta) \right] \quad (3.10)$$

The index of refraction of argon as calculated is less than unity for temperatures in excess of 6000 K. This simply implies that the "group" velocity of the photons is greater than the speed of light. The index decreases with increasing temperature and thus the ray is bent away from the centerline.

To calculate the radiative losses from the plasma, a point-by-point volume analysis is made. The power emitted by the continuum is calculated in Eqn. (2.15). The line emission losses are determined from

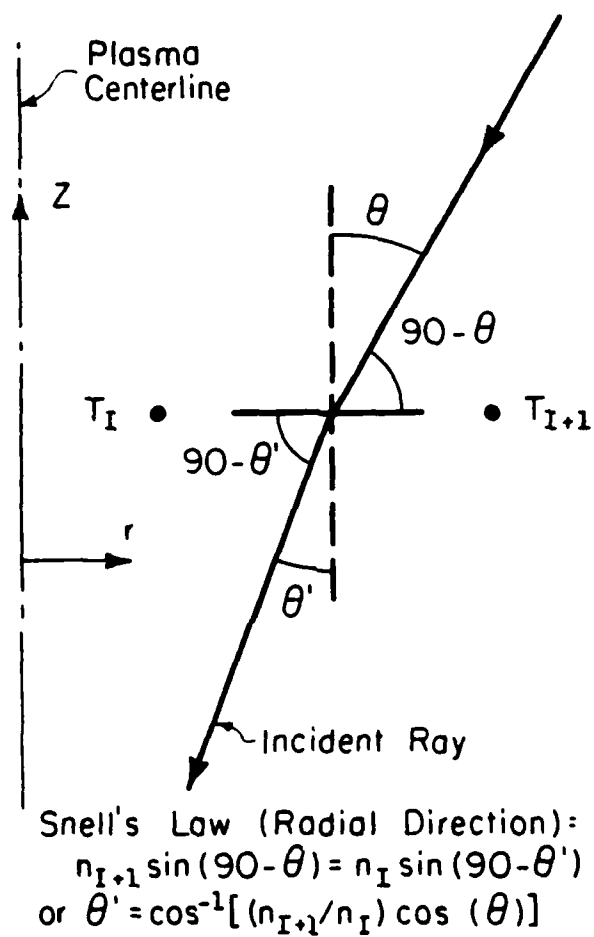


Figure 26 Geometry of Beam Refraction in Plasma Volume

the calculated continuum emission after the work of Kozlov [65]. The details of the radiation losses, absorption, and thermophysical properties are treated in Chapter 5 on the numerical model. The result is that a parameter, thermal efficiency, is defined as:

$$\eta_{th} = \frac{P_{absorbed} - P_{radiated}}{P_{incident}}$$

Thermal efficiency is a parameter which can be directly compared to thermocouple measurements in the pure gas experiments. The parameter is a value of the net energy retained by the gas that would be available for conversion to kinetic energy. However, due to errors, the value is a qualitative assessment of the overall temperature field. Thermal efficiency is sensitive to the grid size and a ± 1 percent change in a grid dimension has resulted in excess of ± 6 percent variation in thermal efficiency. Thus throughout this effort thermal efficiency is treated as a figure of merit which must be greater than zero (power absorbed > power radiated) for the data to be considered viable. The other calculated property, global absorption, has been seen to vary less than ± 2 percent for similar variation in axial dimensions and less than ± 1 percent for radial errors.

The absorption code also calculates the cell by cell reradiated energy delivered to the target. During the calculation of the total radiation losses a view factor between the lower face of a given cell and the laser spot at the target surface. The area of the lower cell face is calculated and the radius an equivalent disk is calculated. The view factor of a disk of radius r_c , height of above the laser spot disk of radius r_s is [66]:

$$F_{r_c-r_s} = 1/2 (Z - \sqrt{Z^2 - 4X^2Y^2})$$

where $X = r_c/z$, $Y = z/r_s$, and $Z = 1 + (1 + X^2)Y^2$. The total power delivered to the spot is summed over all cells. The results will be presented in Chapter 4 and will confirm the first-order calculations detailed in Chapter 2 that if all of the reradiated energy was coupled to the target, the magnitude is less than 2 percent of the transmitted laser power. Further, the total reradiated power is on the order of a few watts and should make little difference to the target areas outside the laser spot.

4. EXPERIMENTAL RESULTS

The previous chapter outlined the various data acquisition and reduction techniques utilized in this investigation. All techniques are applied to each radial profile at a given axial plasma location. All axial locations are then stacked to form a two-dimensional temperature mapping. This chapter will present representative two-dimensional temperature fields for qualitative comparison. Quantitative comparison will be made on the basis of global absorption and radiative loss terms.

The first section will develop the pure argon plasma results. The quantitative analysis is made as a function of power and flowrate. The results are then compared with independent measurements as a consistency check of the spectroscopic data. The second section discusses the applicability of relative line and line to continuum diagnostics in metal-gas plasma spectra. Quantitative comparison of plasma behavior is made as a function of power, translation speed, and surface treatment. The pure aluminum results have been used in conjunction with a transport model to demonstrate the effects of plasma formation on melt/solid interface growth.

4.1 Pure Argon Plasmas

The pure argon temperatures have been determined using relative line to continuum techniques as discussed in Chapter 3. The data shown in the following section corresponds to the 415.8 nm ArI line and adjacent blue wing continuum. Figure 27 is a typical quasi-three-dimensional plot of a 5.5 kW, $f/2.4$, argon plasma temperature field at 15 cm/sec. Figure 27a is a view from the upstream, 27b is a side-on view, and 27c a downstream view of the temperature field.

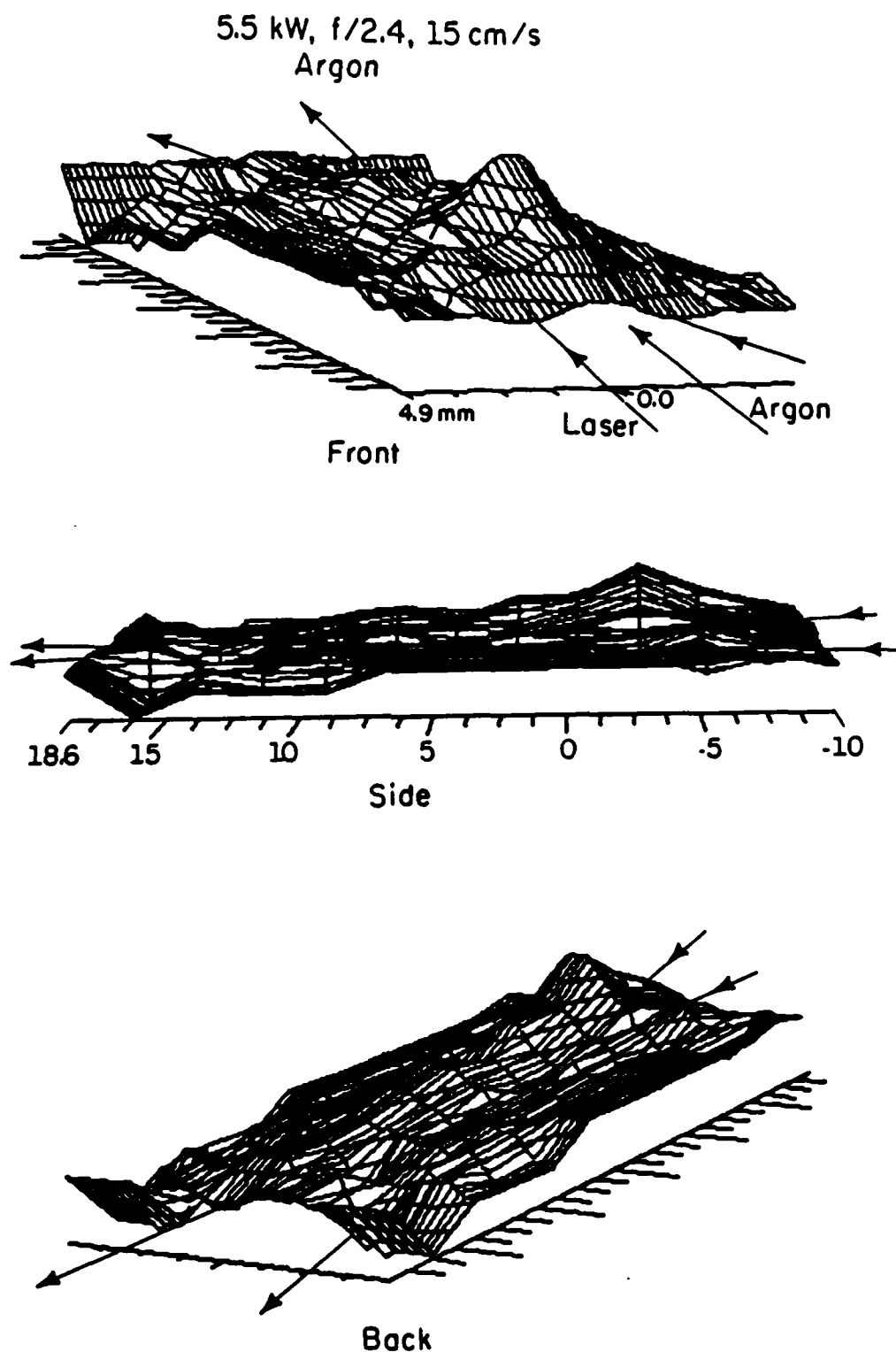


Figure 27 Three-dimensional Temperature Field of a 5.5 kW
Pure Argon Plasma, $f/2.4$, 15 cm/sec

One notes the rough edges depicted in Fig. 27. The rippling at the edges are due to the wing errors associated with the Abel inversion. The effect was discussed in Chapter 3. The edges, however, are at sub-10,000 K temperatures and thus have little effect on laser attenuation. The edge effects are also minimized when the geometrical propagation path of the laser beam in Fig. 27 is taken into consideration. The main effect of wing error is in the radiation calculations. Although relatively small temperatures are encountered in these regions, the local volumes are large compared to the centerline regions. This makes the wing contributions to radiative losses non-negligible and results in the relatively large error bars for thermal efficiency data, that will be seen in subsequent figures.

Welle, Keefer, and Peters [23], using absolute intensity calculations, showed off-axis peaks in certain regions of the pure argon plasmas. The off-axis peaks are directly attributable to the Abel inversion and therefore may not be real events. The Abel inversion can result in a reduced emissive power near the centerline. This reduction can be interpreted as a lower or higher electron temperature depending on what temperature the peak emission corresponds to. The off-axis peaks did not occur at higher flow rates in Ref. [23]. Nonetheless, the off-axis and centerline peaks result in negligible differences in the calculated global properties when comparing the results herein to Ref. [23].

The plasma begins at -10 mm (± 0.5 mm) upstream of the laser focus. The peak temperature at approximately -3.5 mm is 19,000 K. The core is approximately 30 mm long and 10 mm wide at the 10,000 K

isotherm, the lower limit of the spectroscopic analysis. The three-dimensional mapping is obtained by folding the radial data about the centerline. In the case depicted in Fig. 27, the global absorption was calculated to be 82.9 percent (4560 W). The reradiated power was 3653 W leaving 907 W retained by the gas for a thermal efficiency of 16.5 percent. The values will be shown to be within experimental error if values calculated from independent measurements and model predictions. The results also agree with the values reported elsewhere [23].

4.1.1 Power Dependence

Figure 28 depicts the spatial dependence of plasma extent as a function of power at $f/2.4$ and 15 cm/sec argon flow velocity. Figure 28a is for the case of 2.4 kW, 28b is 4.1 kW, and 28c is 5.5 kW (as was shown in Fig. 27). The peak temperature in Figs. 28a-c shows a general rise with power going from 17,500 K to 19,000 K in Figs. 28a and 28c. The peak temperature in Fig. 28b is only 17,000 K which is due to the error in the Abel inversion near the centerline. The more important trend is that the 17,000 K core region has grown significantly in volume from low power to high power. The core region and plasma front have also moved further into the upstream flow as power is increased. Finally, the plasma length has grown significantly between 2.4 kW and marginally between 4.1 kW and 5.5 kW. The net result will be seen to be an overall increase in absorption and radiative loss with increasing laser power.

The calculated values of global absorption are 60.0 percent (1440 W, 72.9 percent (2990 W), and 82.9 percent (4560 W) for 2.4, 4.1, and

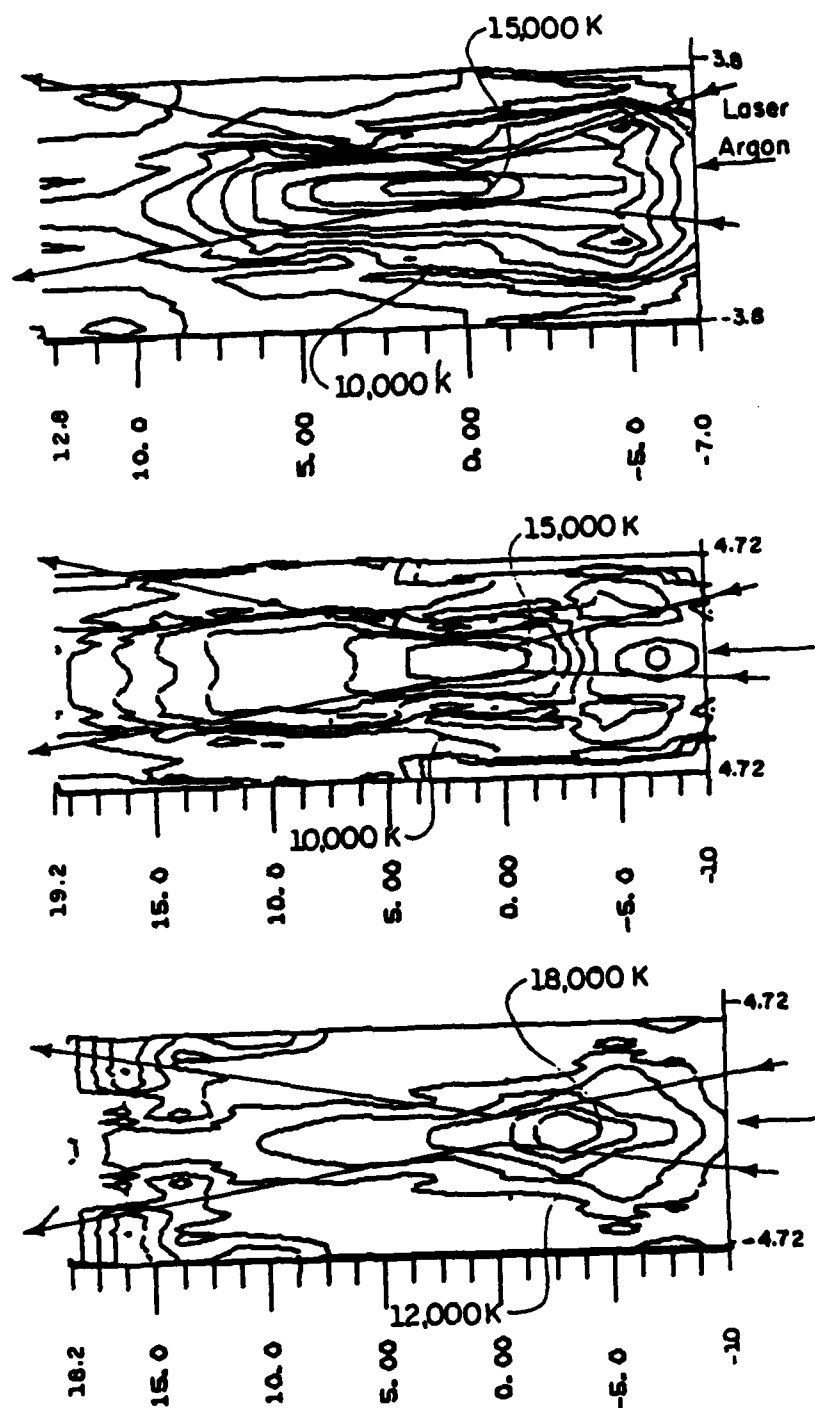


Figure 28 Two-dimensional Temperature Fields of:
 (a) 2.4 kW, (b) 4.1 kW, and (c) 5.5 kW Pure
 Argon Plasmas, $f/2.4$, 15 cm/sec

5.5 kW incident laser power, respectively. Figure 29 compares the results to the values calculated by a numerical model [22] and trend agreement within experimental error is indicated. The error bars represent the fluctuation about the data point given a ± 4 percent temperature error. The temperature error was applied uniformly across the temperature grid and thus represents a worst case scenario. The highly non-linear properties of absorption coefficient and radiation loss are the main contributions for error bands for absorption and thermal efficiency, respectively. A more realistic approach to error analysis would be to segment the error based on spatial location as was demonstrated in Chapter 3. Finally, the data points of Fig. 29 represent a summation over 400 to 1000 temperature cells and this type of error behavior is not unexpected. The important point is that the error bands indicate trends similar to the data.

The thermal efficiency, defined as the difference between power absorbed and power lost via radiation divided by incident power, has also been calculated. In Fig. 29, the results again are shown to agree with the modeling effort within experimental effort.

One notes the relatively large error bars on the efficiency data. Since the power radiated is a function of spatial extent, i.e. radial and axial increment, two more variables and associated errors are involved. In the absorption calculation, radius was shown to have little effect while axial dimensions are dominated by the absorption coefficient in a decaying exponential term. The two variables are directly used to calculate the unit volume in the radiation terms and thus ± 10 percent of radial and axial dimensions significantly alter the

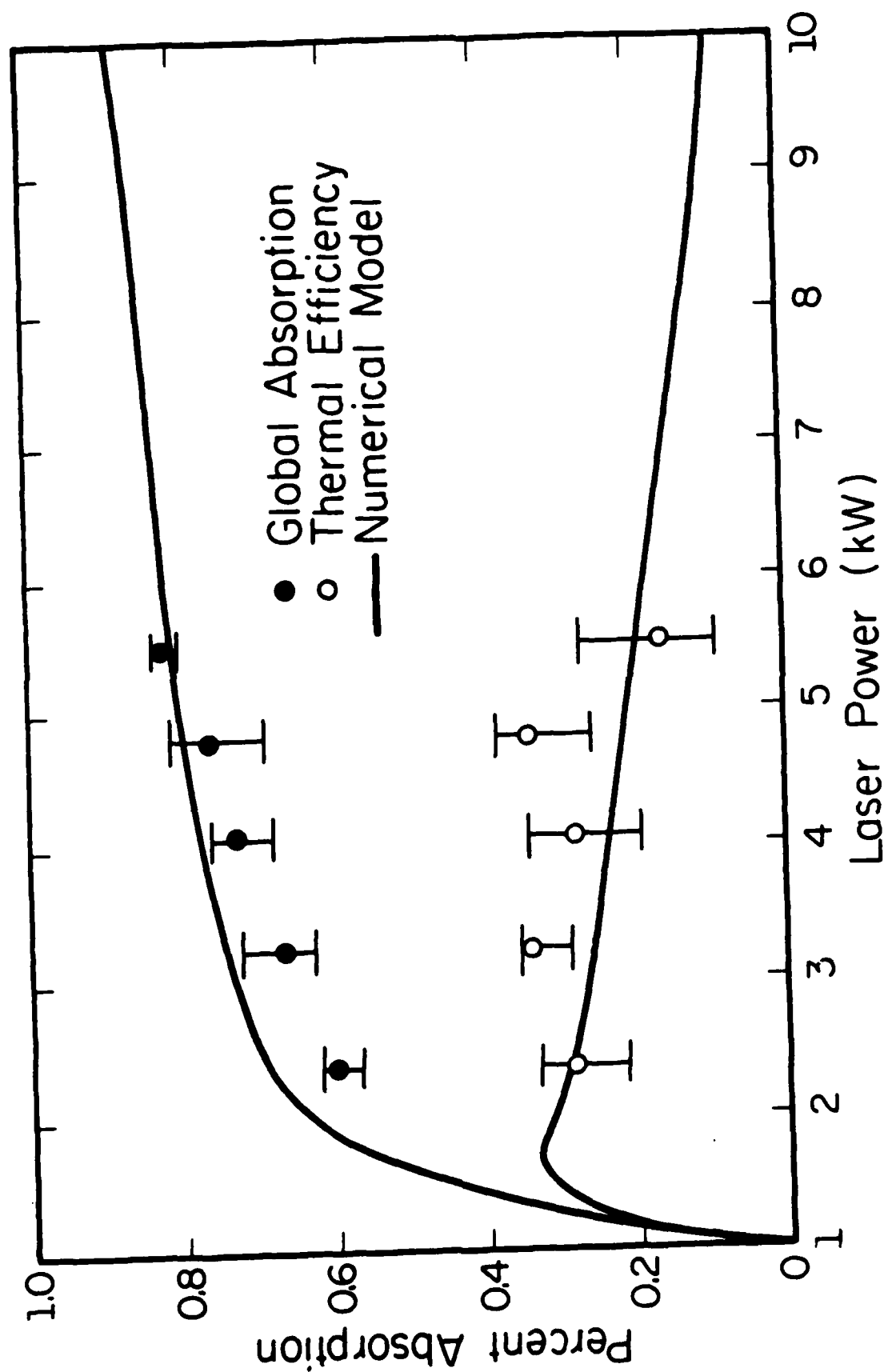


Figure 29 Global Laser Power Absorption as a Function of Laser Power: Pure Argon, $f/2.4$, 15 cm/sec

results. Thus it should be mentioned that the thermal efficiency and radiative losses are used in a qualitative sense throughout this investigation. The thermal efficiency must be greater than zero to avoid second law violations that imply radiated power to be greater than absorbed power. The important use of the efficiency data is that the trends of the numerical model have been verified. The thermal efficiency was calculated to be 28.2 percent (680 W), 28 percent, (1150 W), and 16.5 percent (910 W) for the cases of 2.4, 4.1, and 5.5 kW, respectively.

The agreement between the spectroscopic and numerical model are not unexpected. As will be seen in Section 4.1.3, the spatial agreement of plasma volume is reasonable. Although minor differences exist between the two methods of calculation, the thermophysical properties used were identical. Thus based upon the spatial agreement with respect to isothermal mappings, global absorption and thermal efficiency should be in close agreement as was shown in Fig. 29. The true consistency check on the spectroscopic data was made by comparison with thermocouple and calorimeter data.

The calorimeter, as shown in Fig. 5, is mounted above the plasma in the downstream region of the PIFC. The laser geometry is carefully aligned to insure that all transmitted laser energy impinges on the walls of the calorimeter. When the plasma is stabilized, the transmitted laser energy is measured. A correction for stagnant gas heating of the calorimeter has been made. Thus, knowing the incident and transmitted laser energy, the absorbed energy can be calculated.

The thermal efficiency is measured via locating the thermocouple carriage in the downstream region of the plasma. By assuming some velocity profile in this region whose average velocity equals the uniform flow field upstream of the plasma, a mixing cup analysis can be performed. The downstream enthalpy flux is calculated and compared with the inlet enthalpy flux to determine the net power retained by the gas. Unfortunately, the plasma radiation effects on thermocouple measurements have yet to be quantified and the thermal efficiency measurements are a qualitative indicator of trends.

Figure 30 depicts the comparison between the various experimental methods as well as the numerical model. Reasonable agreement between calorimetric and spectroscopic data is indicated at all powers. Thermal efficiency agrees in trend and to a lesser extent in magnitude. The result is that the spectroscopic results have been demonstrated to be reasonable and consistent such that the spectroscopic data may be used independently of the other diagnostics as an assessment of plasma behavior. The result was critical in the evaluation of metallic target plasma as will be detailed in Section 4.2.

4.1.2 Flow Rate Dependence

Figure 31 shows the effect of increasing flow rate on plasma spatial extent at a fixed laser power. The results are for 4.1 kW, $f/2.4$ at 15, 60, and 120 cm/sec flowrates in 31a, b, and c, respectively. It can be seen that the plasma is elongated into the downstream region significantly as flow rate is increased. Figure 31b and c have been expanded two and three times, respectively, in the

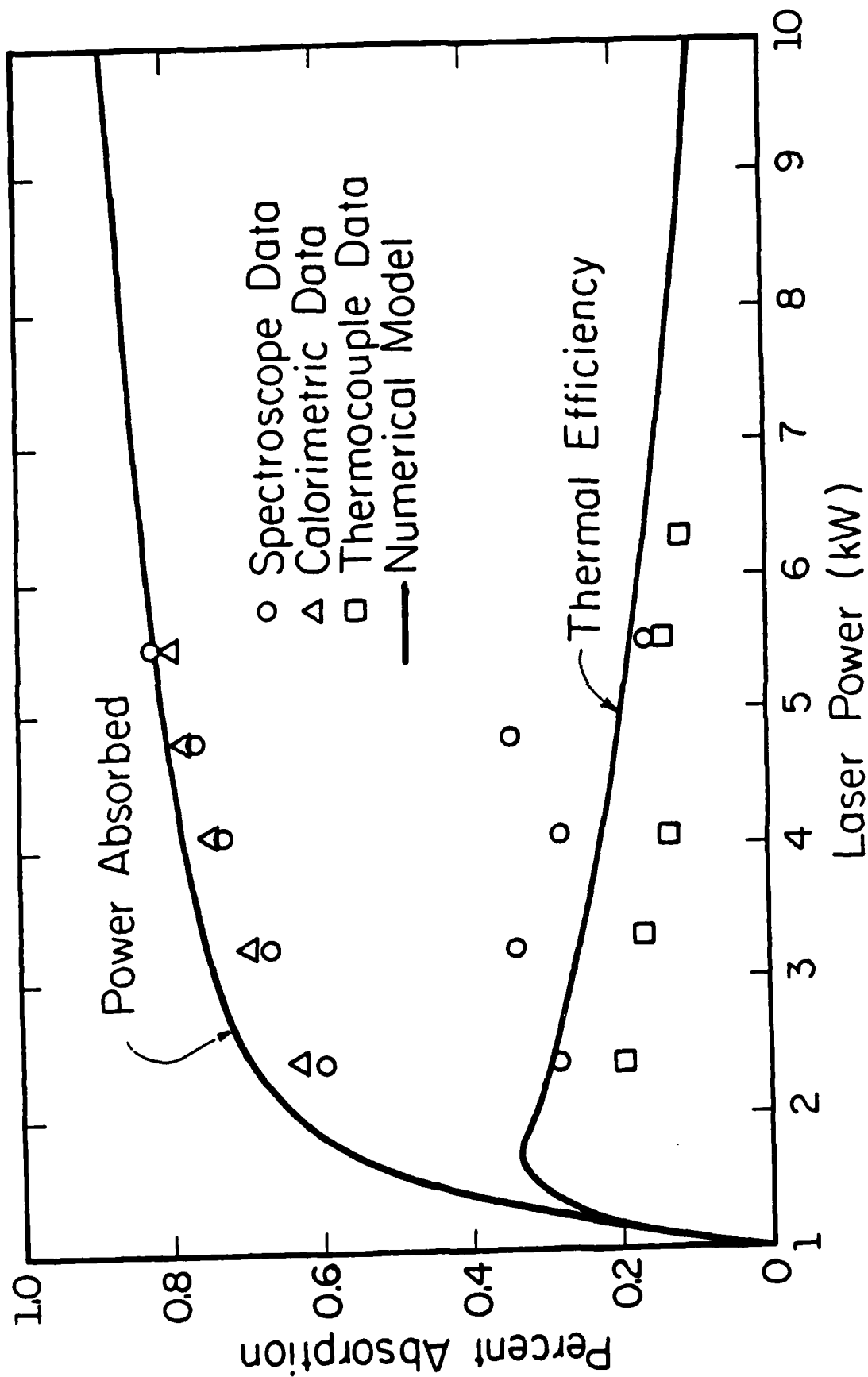


Figure 30 Comparison of Spectroscopically Determined Parameters with Calorimetry and Thermometry Data

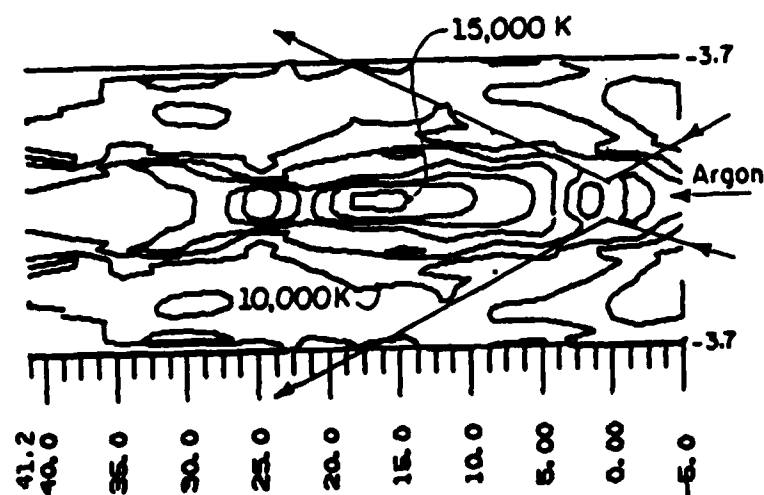
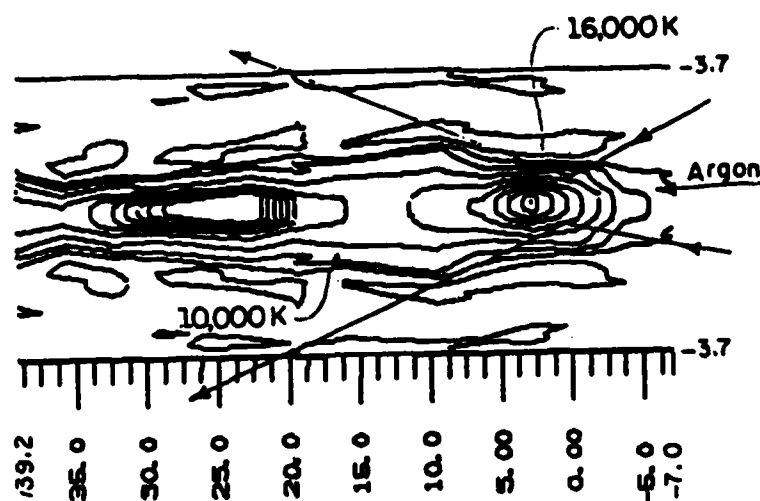
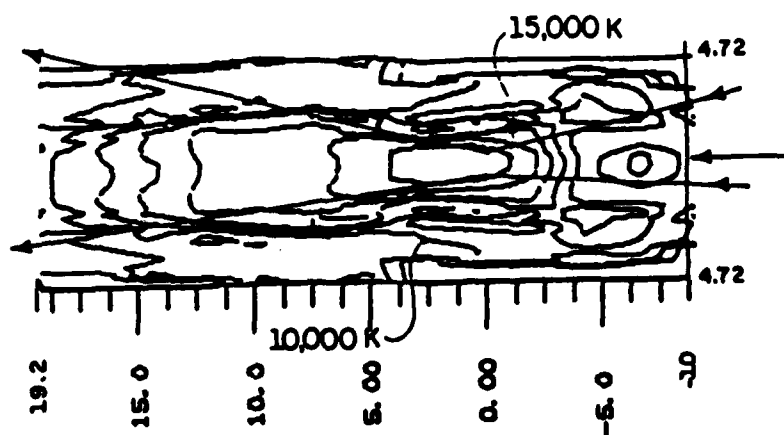


Figure 31 Two-dimensional Temperature Fields of:
 (a) 15 cm/sec, (b) 60 cm/sec, and (c) 120 cm/sec
 Pure Argon Plasma, $f/2.4$, 4.1 kW

radial dimension for clarity. Increasing the flow rate from 15 to 60 cm/sec nearly doubles the length of the plasma. The net absorption in this case is reduced since the absorption length gains are offset by an overall reduction in temperature. The peak temperature is further reduced to 15,400 K in the high flow case, Fig. 31c.

The plasma front has been pushed closer to the focal spot of least confusion with increasing flow rate. The plasma is also narrower approaching a cigar shape versus the tear drop shape at low flow rates. One also notes temperature peak downstream of the focus. At first this was thought to be an artifact of the Abel inversion. However, nearly all of the high flow cases (≥ 60 cm/sec), at any power, showed similar trends. A review of the measured intensity data occasionally showed local line-of-sight intensity increases in this region. This leads one to speculate on the possibility of downstream eddy mixing regions. This is a distinct possibility based upon the recent results of Ref. [24], a full solution of the Navier Stokes equations. The results of Ref. [24] indicate that relatively little or no mass flow is occurring in and about the central regions of the plasma near the laser focus. This would support streamline formation with components normal to the plasma axis immediately downstream of the focus. The results of Ref. [24] do not indicate this flow feature, as eddy generation is not treated in the effort. The effect cannot be verified until proposed flow measurement diagnostics have been applied.

Figure 32 shows the flow velocity dependence of absorption and thermal efficiency for the spectroscopic data at 5.5 kW. For comparison the model [22] results at 5 kW are shown. One sees that the total

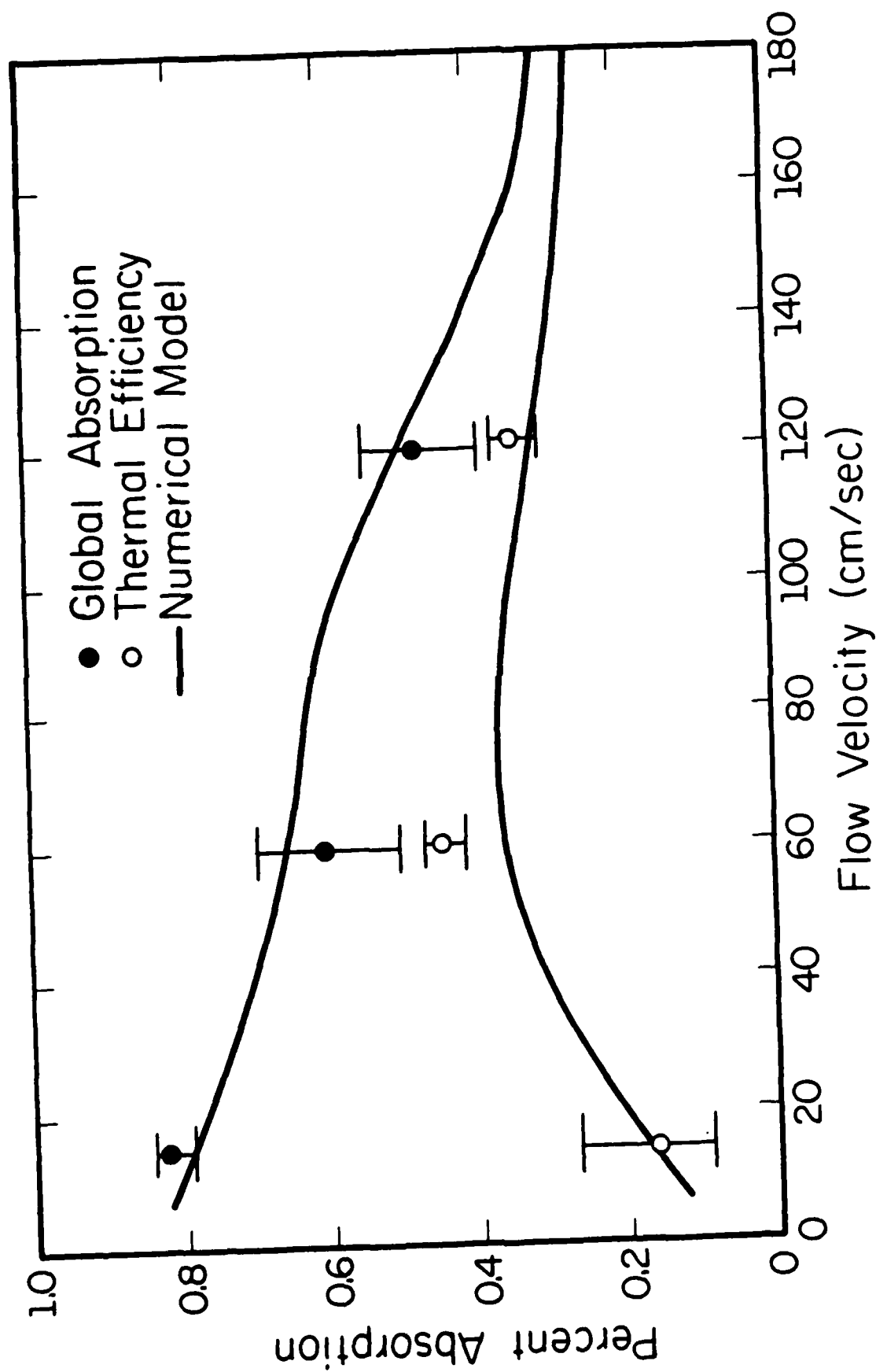


Figure 32 Comparisons of 5.5 kW Spectroscopic Data to a Numerical Model (22) at 5 kW as a Function of Flow Velocity: Pure Argon, $f/2.4$

absorption decreases with increasing flow velocity. The overall plasma temperature is lowered and dominates any effects of increased plasma length. The dip in the model prediction could not be verified with the limited number of data. The thermal efficiency data indicates that there is an optimal flow velocity for a given power and beam geometry, as calculated by the model. The peak arises again from geometrical considerations. At low flow rates the plasma length and temperature define absorption behavior. As the flow rate is increased the lower plasma temperatures reduce radiative losses and increasing thermal efficiency is the result. With further increases in flow rate the radiative losses are further reduced. The effect is that absorbed energy roughly approaches some minimum value, just prior to blow out, where radiative losses are negligible. Unfortunately, this regime exists at very low plasma temperatures where the net absorption is minimal.

Figure 33 shows the results for the cases of 2.4 and 4.1 kW versus flow velocity. In general, the trends are similar to Fig. 32. Decreasing absorption with flow velocity and indication of a peak in thermal efficiency. Another qualitative trend that the efficiency peak occurs at a lower velocity for a lower power is indicated. This trend was also predicted by the modeling effort.

4.1.3 Comparison with a Numerical Model [22]

Figure 34 is a comparison of the spatial extent of an argon plasma as calculated from the spectroscopic data (34a) and the model (34b). One notes the spatial agreement of the isotherms as mentioned

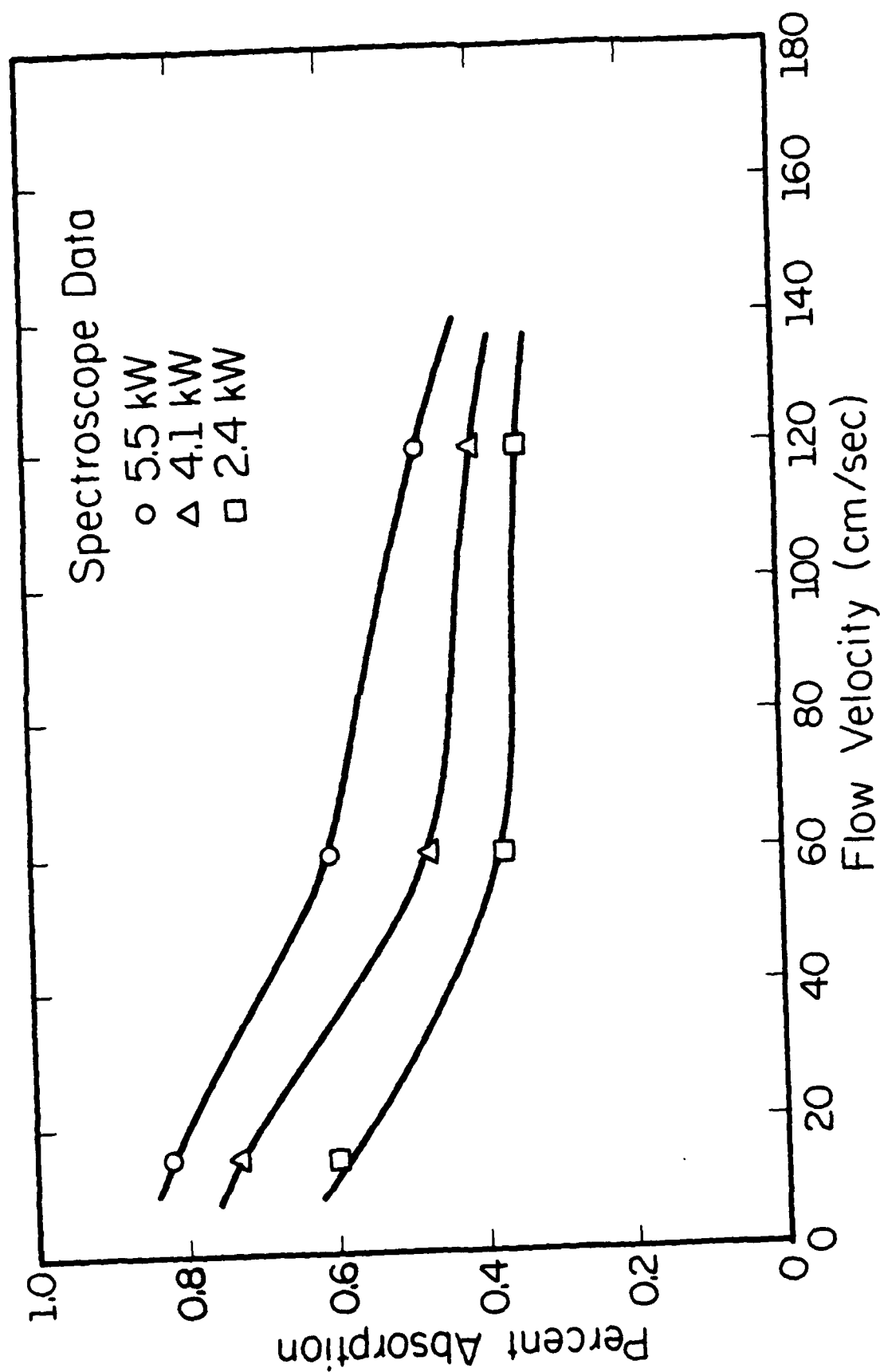


Figure 33 Global Laser Power Absorption as a Function of Flow Velocity: Pure Argon, $f/2.4$

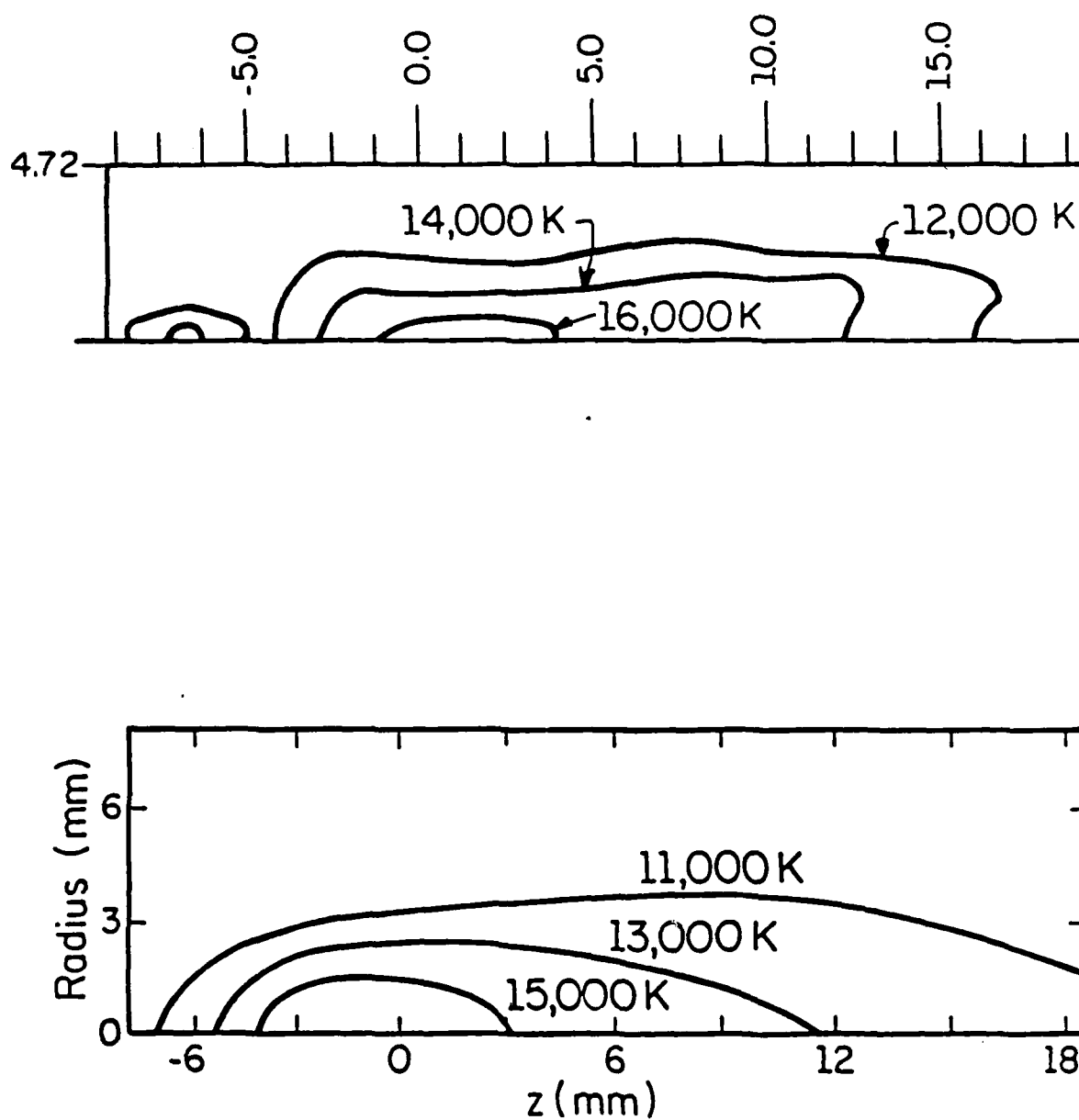


Figure 34 Comparison of Spatial Extent of Spectroscopic Data and a Numerical Model (22)

previously. Since the absorption and radiation calculations are treated similarly, the previously shown agreement between the data and model was expected. The agreement between the spectroscopic and calorimeter and thermocouple data demonstrated consistency in trends and magnitudes. This allows one to apply the diagnostics to more complicated plasmas.

From the data and model predictions, new plasma regimes of interest have been developed. First, the elongated, cooler plasma, to a certain extent, retained more useful energy in the downstream gas. This trend was indicated by all measurements. Thus, the next step is to geometrically elongate the plasma and operate at higher flowrates to obtain peak efficiencies. This will be accomplished by the use of higher $f/\#$ optics to confine the plasma in a longer, narrower cone. Also proposed is a means of reducing radiative losses via multiple plasma formation. The effect is largely geometrical as the radiative view factors to the wall have been reduced by the plasma-to-plasma view factors. Also, each of two plasmas operates at half power resulting in a lower percentage of radiative losses than in the case of one plasma at twice the power. The other area of interest is higher pressures where radiation losses dominate due to increased numbers of emitters and absorbers. Once the two proposed regimes, $f/\#$ and multi-plasma, as well as increased pressure have been quantified an accurate assessment of scaling laws from the model can be made.

4.2 Aluminum Targets in Argon Atmospheres

Throughout this portion of the investigation, an $f/7$ beam geometry was used. This was due to the inability to initiate the plasma on

aluminum targets at higher f/#s with the 10 kW AVCO CO₂ or with the Gaussian beam of the 1.5 kW Photon Sources CO₂ lasers. The plasma formation has been studied with respect to surface treatment and translation speed.

4.2.1 Comparison of Data Analysis Techniques

Ideally, one would prefer to utilize the same data reduction method for the aluminum data as was used in the pure argon studies. However, it was unknown a priori, the extent of aluminum effects in the argon plasma. Minimally, the aluminum was expected to bias the continuum emission rendering relative line to continuum techniques invalid. Thus, a pair of argon lines which could be used in a relative technique were sought.

The spectra, as was seen in Fig. 15, has resolvable ArII lines which meet the criteria for relative line diagnostics. This effect is attributed to the aluminum presence as the ArII spectra was not observable in the pure gas cases. Several authors had used the 457.9 and 458.9 nm ArII lines successfully. Two problems exist. First, the ArII lines exist only in the hotter central regions of the plasma. The ArI spectra must be calibrated to the ArII temperatures in order to completely map the plasma. The process is relatively complicated and requires approximately twice the number of data points compared to the relative line to continuum method. Secondly, the 457.9 and 458.9 nm ArII lines are separated from any ArI lines which have a reasonable signal-to-noise ratio above the continuum. Thus two independent mappings of the plasma emission are required which further increases error in the data.

The 457.9 and 458.9 nm ArII temperature data was compared to the 415.8 nm ArI line to continuum data. If it could be shown that the profiles agreed within experimental error, or that global properties agreed within experimental error, the easier line to continuum method could be used for the metal vapor/argon plasmas.

The analysis was performed on aluminum/argon plasmas at 3, 5, and 7 kW incident laser power. Figure 35 is a typical radial temperature profile. Figure 35a is the 415.8 nm to continuum data, 35b the 457.9/458.9 nm and 35c the 696.5 nm ArI to continuum data. As can be seen, fair agreement between all three techniques is indicated with most of the temperature field agreeing within experimental error. Table 1 is a listing of the calculated values of absorption and thermal efficiency for the case of 5 kW plasma. It can be seen that the global results are well within experimental error, further indicating the accuracy of the relative line to continuum technique. Finally, the aluminum line spectra were not resolvable except in the region within 2 mm of the target surface. This further supports the proposal to analyze the plasma as pure argon. The strongest aluminum lines resolved were the 394.4 and 396.6 nm resonant lines which extended a few mm into the plasma, but typically less than 30 percent of the overall plasma length.

Table 1

Technique	$P_{abs}(\%)$	$\eta_{th}(\%)$	$R_{spot}(mm)$
457.9/458.9 nm ArII	16.46	12.46	0.506
696.5 nm ArI	14.22	11.83	0.504
415.8 ArI	16.42	13.49	0.508

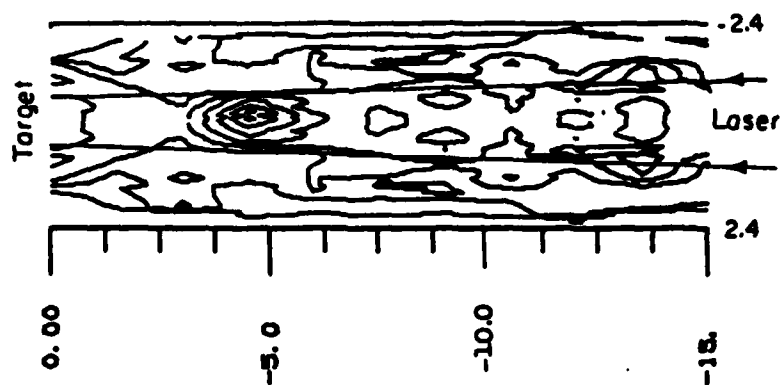
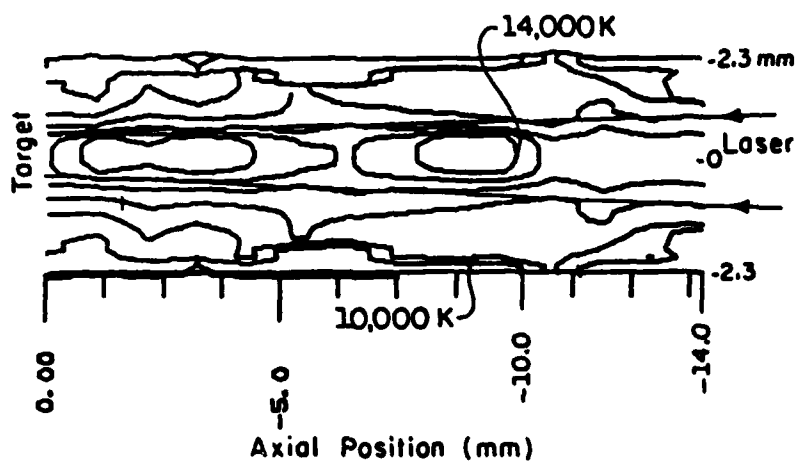
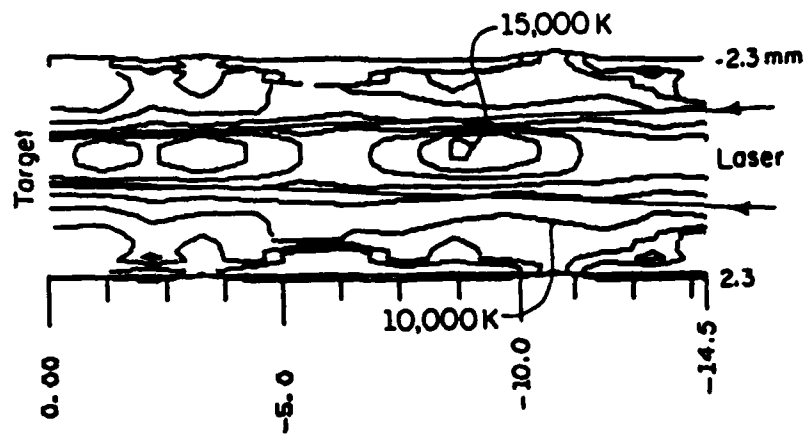


Figure 35 Comparison of Typical Radial Temperature Profiles using Various Reduction Techniques

Thus with a reasonable amount of confidence, the remainder of the aluminum/argon data will be reduced using the relative line to continuum technique. In light of the large errors shown in previous investigations [53,54] the above error has at least been demonstrated to be within the experimental accuracy of the various techniques. Also, when the software for the OMA is fully operational, it may prove useful to analyze the larger data sets required for relative line techniques. The inability to transfer data from the OMA to another computer system except manually is the main reason. The Hemenway® BASIC language supplied as an option on the OMA does not permit data reduction and analysis on the OMA. The BASIC system may not permit the access of certain intrinsic functions as well as external functions necessary for data reduction. The BASIC system is also extremely slow compared to the CYBER or HP systems available.

In the analysis of the aluminum/argon data an additional parameter was calculated. The refraction of the laser beam is calculated as the ray bundle propagates through the plasma. In this investigation and elsewhere [23] beam refraction was shown to have little effect on global absorption (± 0.5 percent). Thus, for simplicity, the refractive index of the outermost ray is calculated as detailed in Chapter 3. The refractive index variation in the plasma is such that the beam is refracted away from the laser axis. The effect will be shown to be considerable in Section 4.2.6 when the experimental results are utilized in a numerical model.

4.2.2 Power Dependence

Figure 36 is a quasi three-dimensional mapping of the temperature field of a 5 kW, f/7 plasma above a 99.9 percent pure aluminum target in an argon atmosphere. The plasma extends approximately 18 mm above the target surface (datum = 0.00) which agrees with visual observation (0.5 to 0.75 in.) the plasma is nearly cylindrical as would be expected for an f/7 beam and an 18 mm axial dimension. Several temperature peaks along the axis are noticeable. These are possibly due to induced flow fields within the plasma as the argon atmosphere was a slow flow with inlet and outlet ports for from the plasma (6 to 8 in.). Optical characteristics of the windows (i.e. reflections) could not be seen when using a spectral lamp source. The likely possibility is error in the Abel inversion as all the peaks in the 5 to 10 mm region are roughly within experimental error of one another.

Figure 37 depicts the temperature fields for 4, 5, and 7 kW, f/7 aluminum/argon plasmas. One sees the general trend of an increase in plasma length and volume as well as overall temperature. In particular in the 5 and 7 kW cases, plasma spreading well beyond the beam geometry is indicated near the target surface. This may be indicative of increased conduction effects in these regions between the plasma and the target.

Figure 38 shows the calculated values of absorption as a function of total incident power. The absorbed power rises relatively rapidly at low powers and again appears to approach some asymptotic value at powers above 7 kW. The thermal efficiency is a meaningless value in this

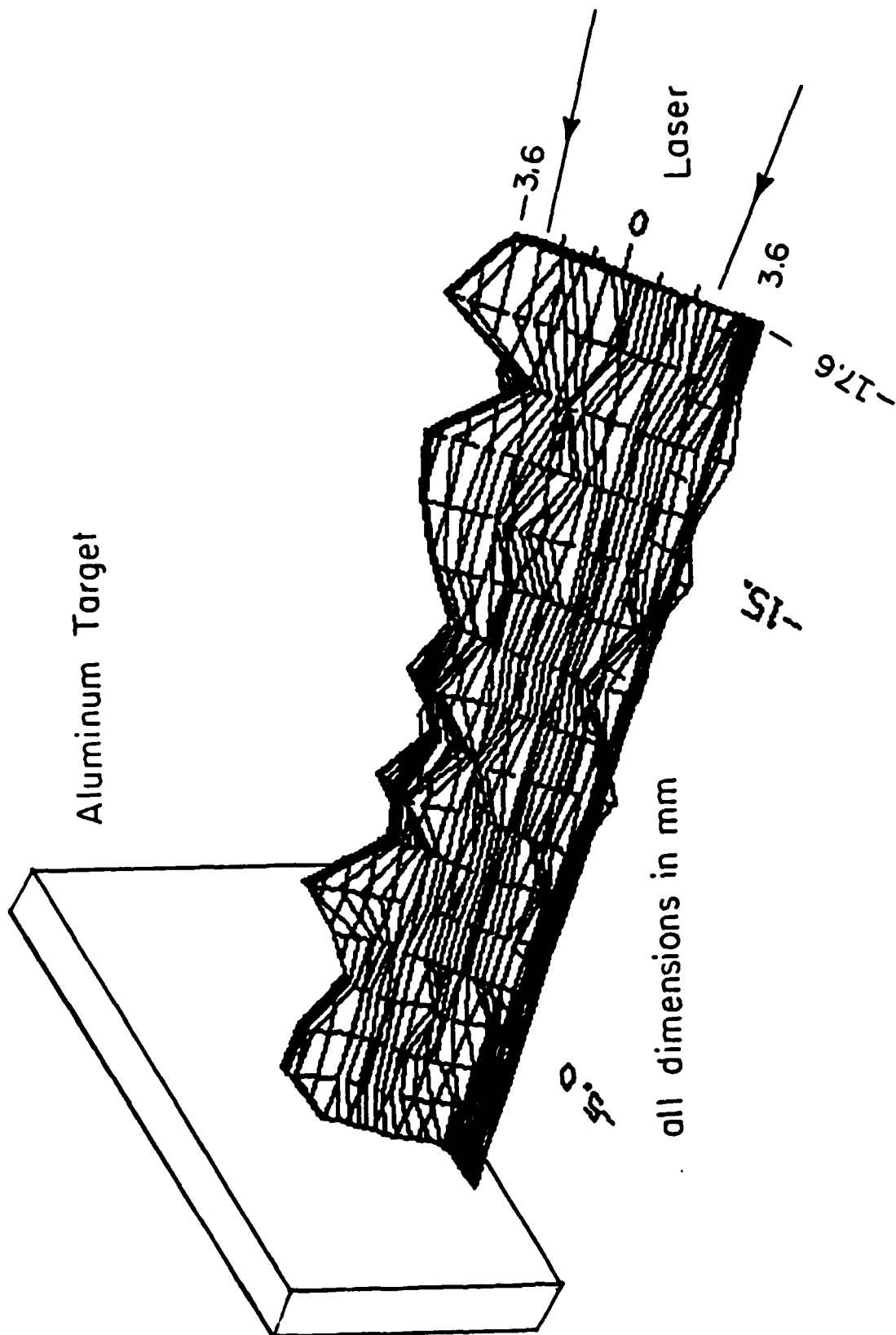


Figure 36 Three-dimensional Temperature Field of a 5 kW, f/7 Aluminum-Argon Plasma

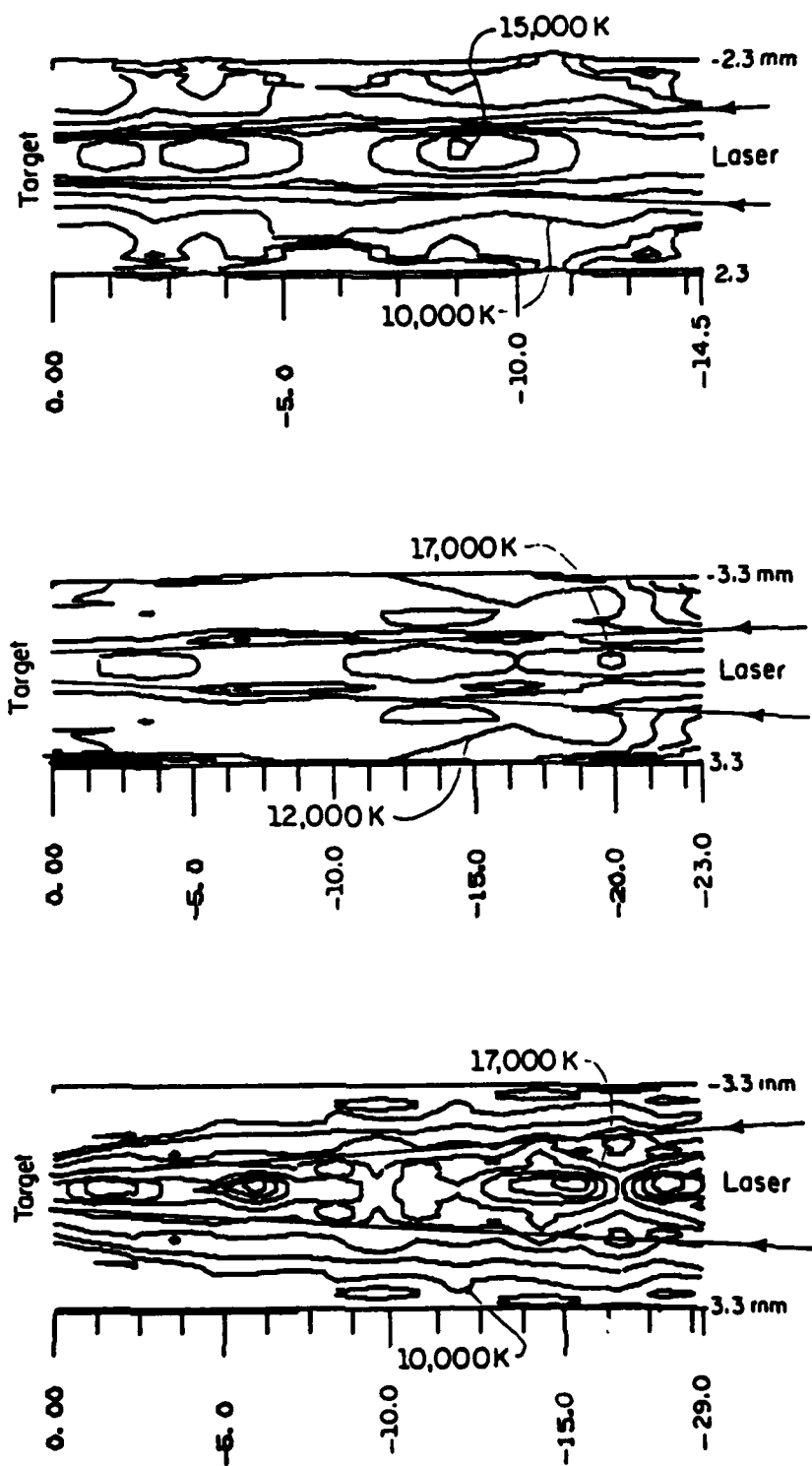


Figure 37 Two-dimensional Temperature Field of an Aluminum-Argon Plasma, $f/7$: (a) 4, (b) 5, and (c) 7 kW

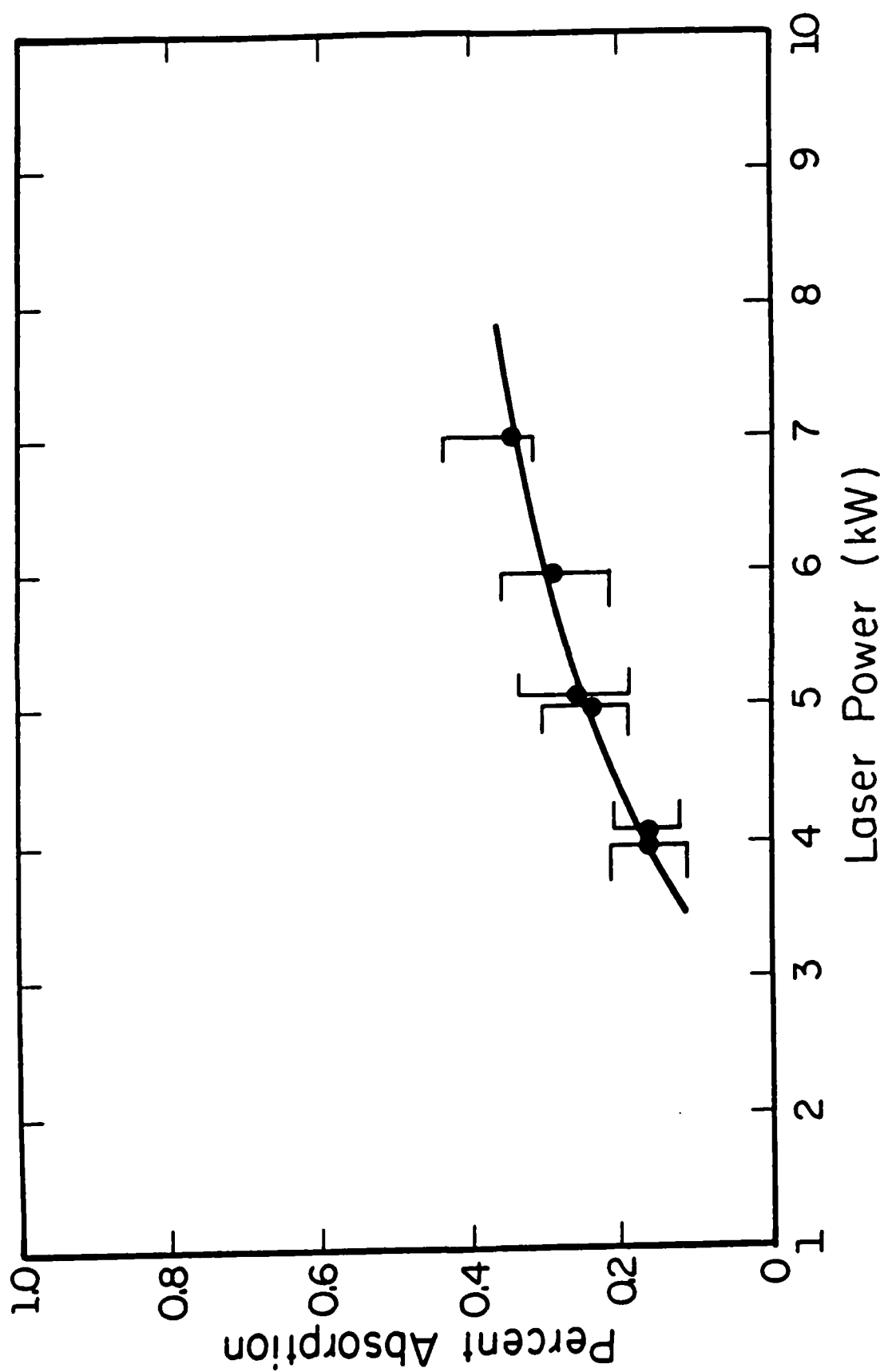


Figure 38 Global Laser Power Absorption as a Function of Laser Power: Aluminum-Argon Plasmas, f/7

portion of the study but is used as a benchmark to indicate the magnitude of the radiative losses. The thermal efficiency is 12.5 percent at 4 kW, rises to 15 percent at 5 kW and flattens out above 5 kW. The radiative transport was estimated via the methodology outlined in Chapter 2 and has been shown to account for less than 1.5 percent of the total energy (including transmitted laser energy) deliverable to the target.

Detailed calculations were made on a point-by-point basis in random plasma fields and further supported the above calculations. The radiative power of each cell was calculated and the solid angle view factor between the lower face of the cell and the laser spot was calculated. The net power delivered from each cell to the spot is summed and compared to the delivered laser power. The results indicated that the radiation effects account for less than 0.5 percent of the total delivered power. Since the view factors between cell side faces were not taken into account, the 1.5 percent figure of the first order calculation can be regarded as a conservative estimate. At first this result was disconcerting in the light of the almost universal acknowledgment of an enhanced coupling regime when a plasma forms.

The effect of beam refraction was later incorporated into the transport analysis, as detailed in Chapter 3. The results are depicted in Fig. 39. Figure 39 indicates that spot size increases with increasing laser power. The effect is a result of the larger radial temperature gradients and increasing plasma length with increasing laser power. The effect is intuitively obvious. The index of refraction is inversely proportional to temperature. Higher temperatures near the

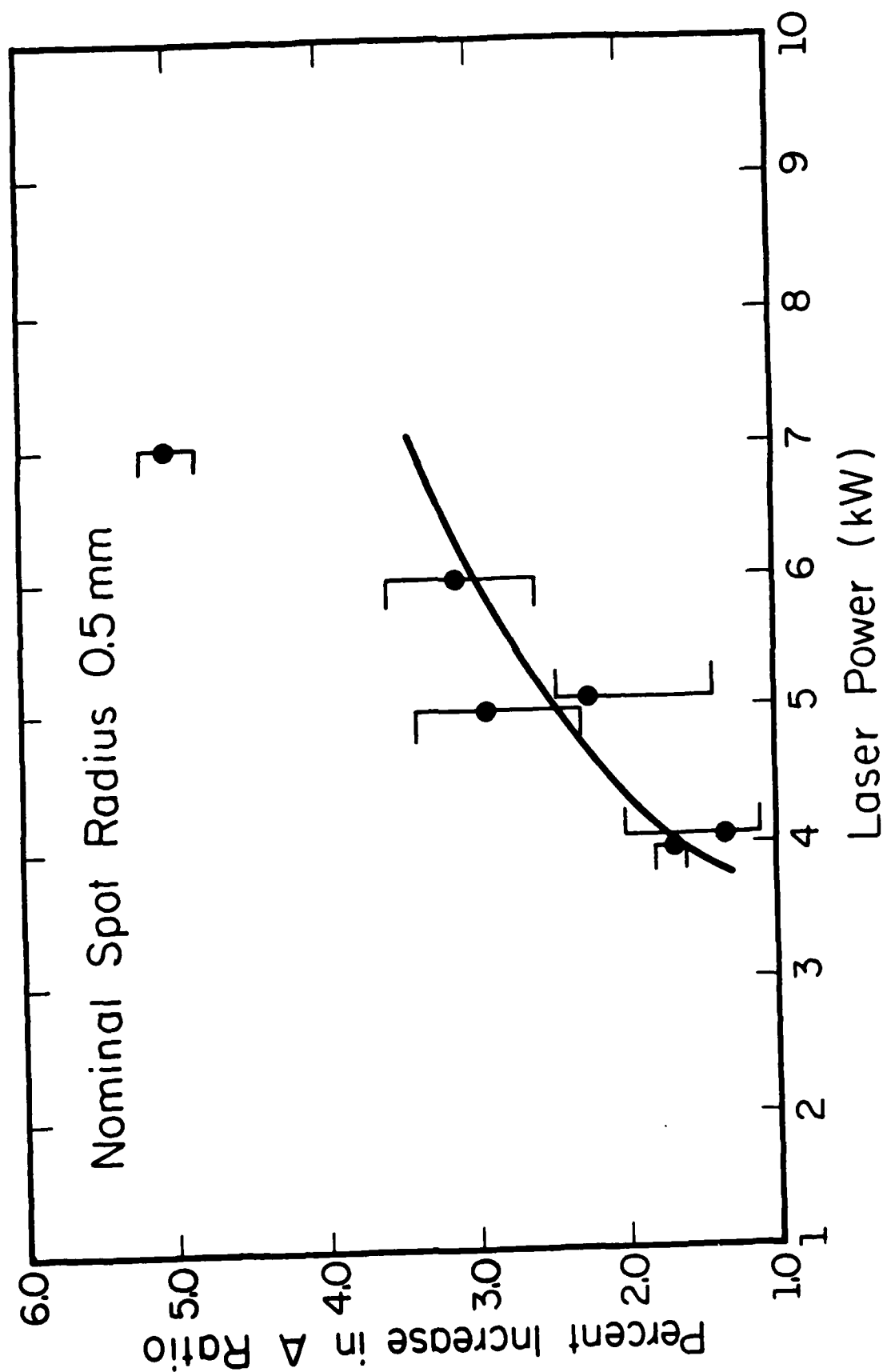


Figure 39 Effect of Beam Refraction on Spot Size at the Target

centerline thus tend to bend the laser rays away from the centerline, increasing spot size. From the temperature profiles shown in Fig. 37 it can be seen that the effect is continuous throughout the plasma volume. The error bars in Fig. 39 result from the uncertainty of the datum (± 0.5 mm). However, the trend is indicated and will be shown to be significant in the determination of the target melt-solid interface in Section 4.2.5.

4.2.3 Translation Speed Dependence

Figure 40 depicts the spatial dimensions of the plasma as a function of target translation speed. The effect of increasing translation speed is a lowering of plasma temperature and volume. Figure 41 shows the trend of the calculated power absorption as a function of translation speed. The 60 in/min speed was nearing the limit where the plasma begins to deflect out of the laser geometry, affecting the symmetry assumption.

Experimental observation indicates that the trend is not continuous as Fig. 41 would suggest. There appeared to be a threshold somewhere between the 20 and 60 in/min. values where the plasma volume suddenly became smaller at the given laser power. The threshold was apparent at all laser powers between 4 and 7 kW. The nominal intensity at 4 kW, 1.0 mm beam diameter, was 1.6×10^6 W/cm². The corresponding interaction time was 0.118 and 0.0393 seconds for the 20 and 60 in/min. speeds, respectively. The data taken in this region was very noisy, further supporting a threshold condition. The noise did not permit reliable assessment of plasma parameters.

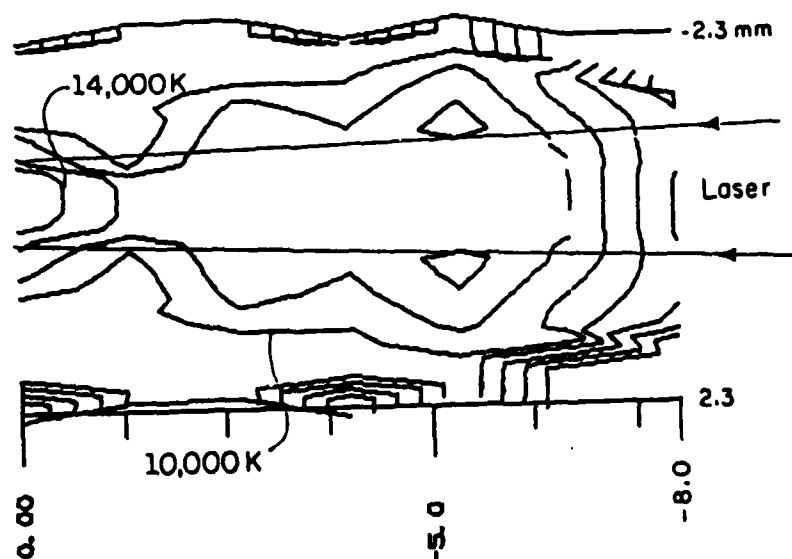
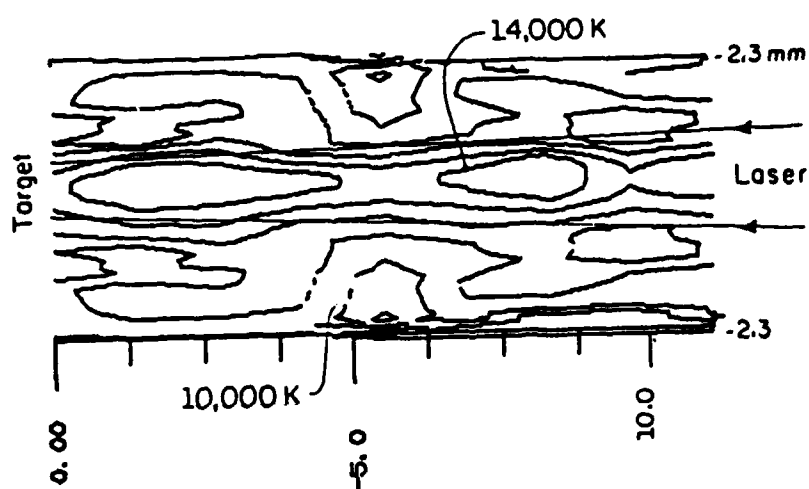
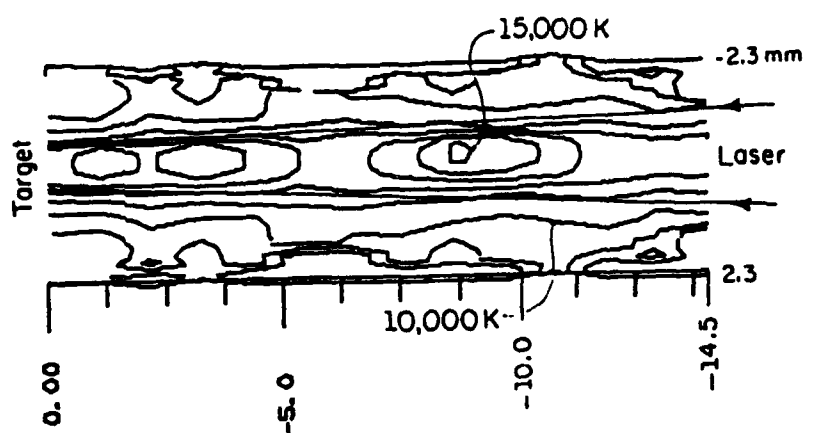


Figure 40 Two-dimensional Temperature Field of a 4 kW, f/7 Aluminum-Argon Plasma:
(a) 10, (b) 20, and (c) 60 in/min

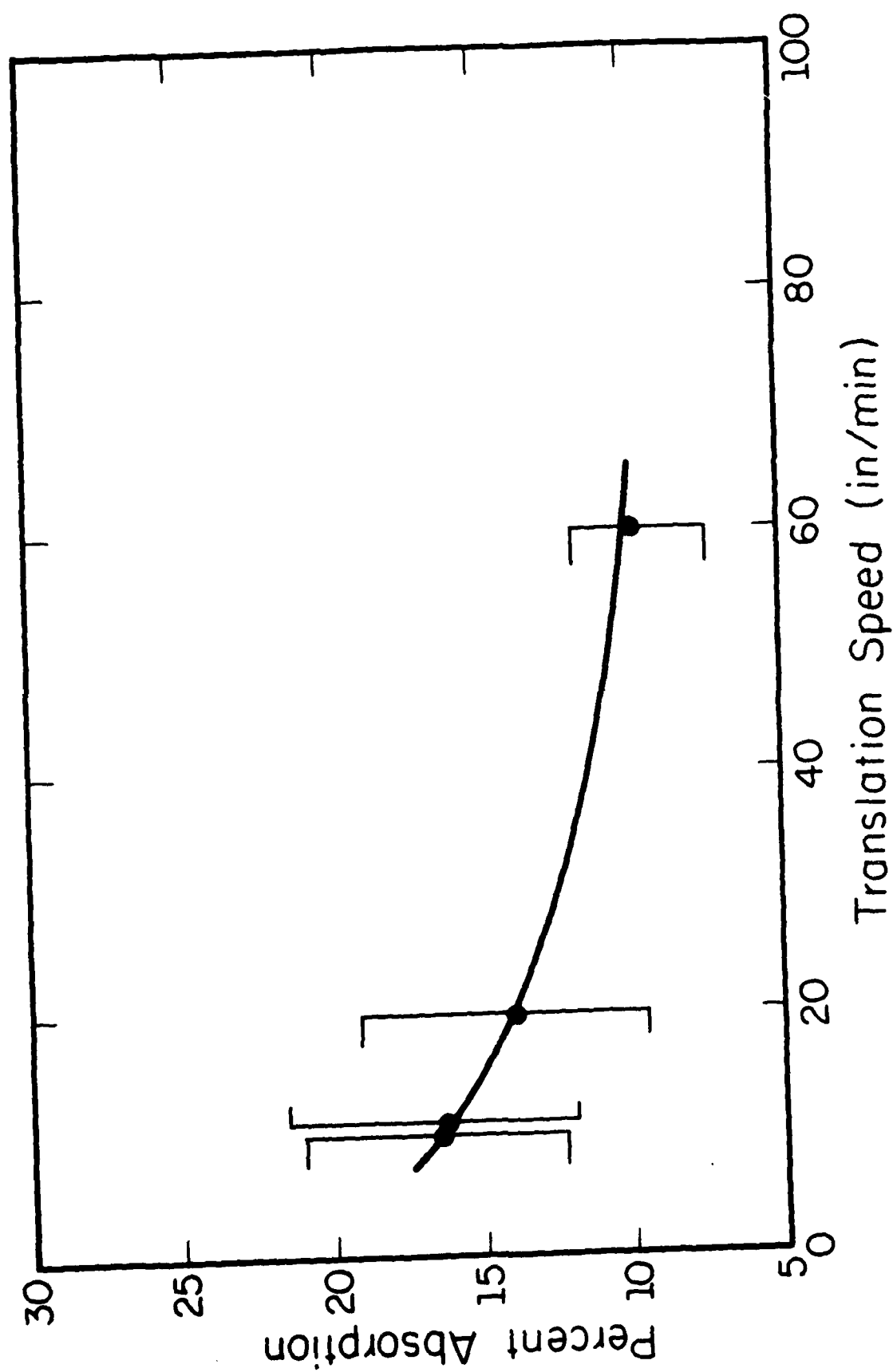


Figure 41 Global Laser Power Absorption as a
Function of Target Translation Speed:
Aluminum-Argon Plasma, f/7

The absorption lowering is largely due to the reduced temperatures between lower speeds. Absorption lowering is dominated by the smaller propagation path length at the higher speeds, above the threshold. The threshold is subjective however, since the plasma radiation is intense enough to distort visual observation.

4.2.4 Graphite Coated Aluminum Targets

Graphite and other absorbing coatings are commonly used to enhance laser coupling to targets. A brief set of experiments was performed to determine whether a graphite coating affected plasma formation. Figure 42 is a comparison of the 4 kW plasma temperature fields for coated and non-coated aluminum targets.

One sees that the graphite has little or no effect on the steady state plasma volume and temperature. No carbon lines could be resolved in any of the spectra at any laser power. The only effect that may occur is a lowering of the plasma threshold, but this could not be verified in this set of experiments. The calculated laser power absorption for the graphite coated targets was 14.3 percent which compares well with the pure aluminum results of Fig. 38.

The experiment was also performed at 5, 6, and 7 kW, f/7, but the intensity profiles were too noisy for Abel inversion and were not reduced. However, the visual observation of the plasma volume correlated with pure aluminum measurements. Future experiments may attempt to monitor the graphite aided plasma formation effect, if any, by gating the OMA detector off the laser or optically triggering from the plasma emission. At this point, an intuitive guess would be that

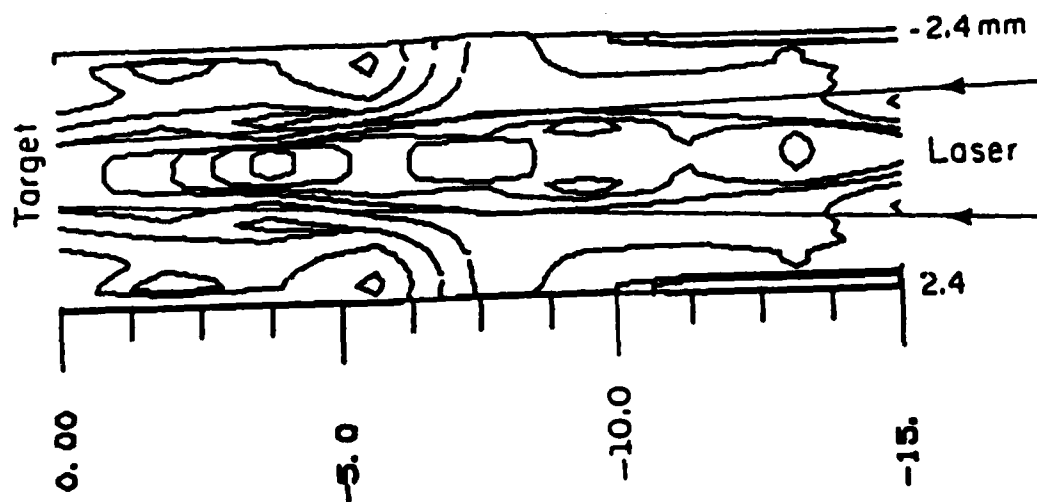
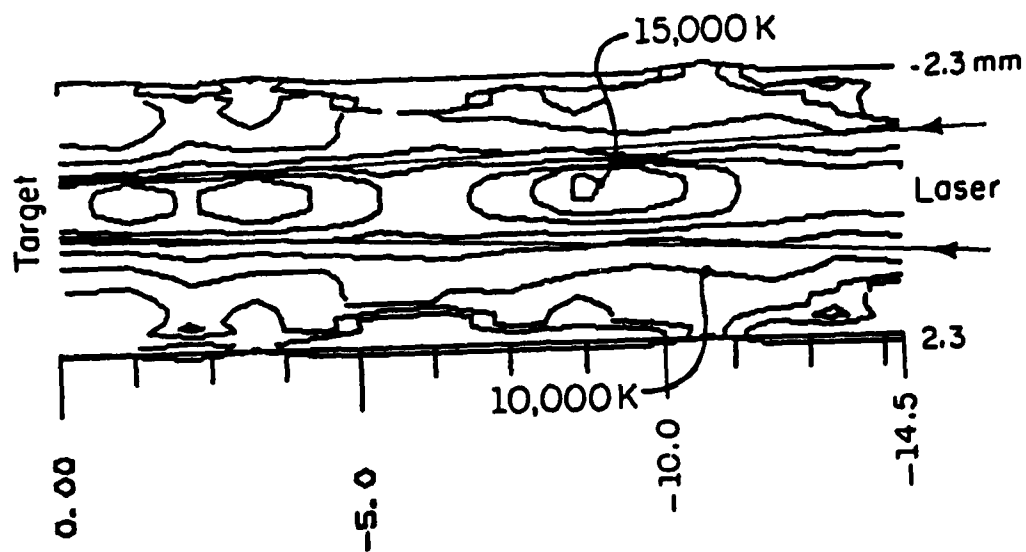


Figure 42 Comparison of 4 kW, $f/7$ Temperature Fields: (a) Pure Aluminum and (b) Graphite Coated Aluminum

graphite, although useful at sub-plasma intensities, serves little or no purpose above threshold.

4.2.6 Effect of Results on Target Transport Model

The effect of the calculated beam attenuation and refraction were analyzed in a target transport model. A three-dimensional conduction model [67] was used to evaluate the target surface temperature distribution and melt-solid interface. Nominal parameters of 5.0 kW, $f/7$, 1.0 mm spot size and the calculated 5 kW plasma parameters of 4 kW transmitted, 1.04 mm spot size.

Figure 43 depicts the results. The higher peak temperature profile corresponds to the 5 kW (no plasma) case, which is as expected. However, both temperature profiles peak well above the melting point of aluminum and significant melting has occurred in the target. The interesting result is depicted in the melt/solid interface predictions. The plasma case actually results in a larger melt volume, a counter-intuitive result.

However, the larger melt volume is indicative of the enhanced coupling regime, noted by several references in the literature survey. The theory for the effect in CW radiation is as follows. The plasma is of the weakly absorbing (LSC) type. Therefore sufficient power is transmitted to the target for vaporization and the plasma to be supported. The main contribution of the plasma is the refractive bending of the focused laser beam out of focus. Since significant melting has occurred at the target under plasma conditions, the dominant parameter in the process is interaction time. Interaction time is

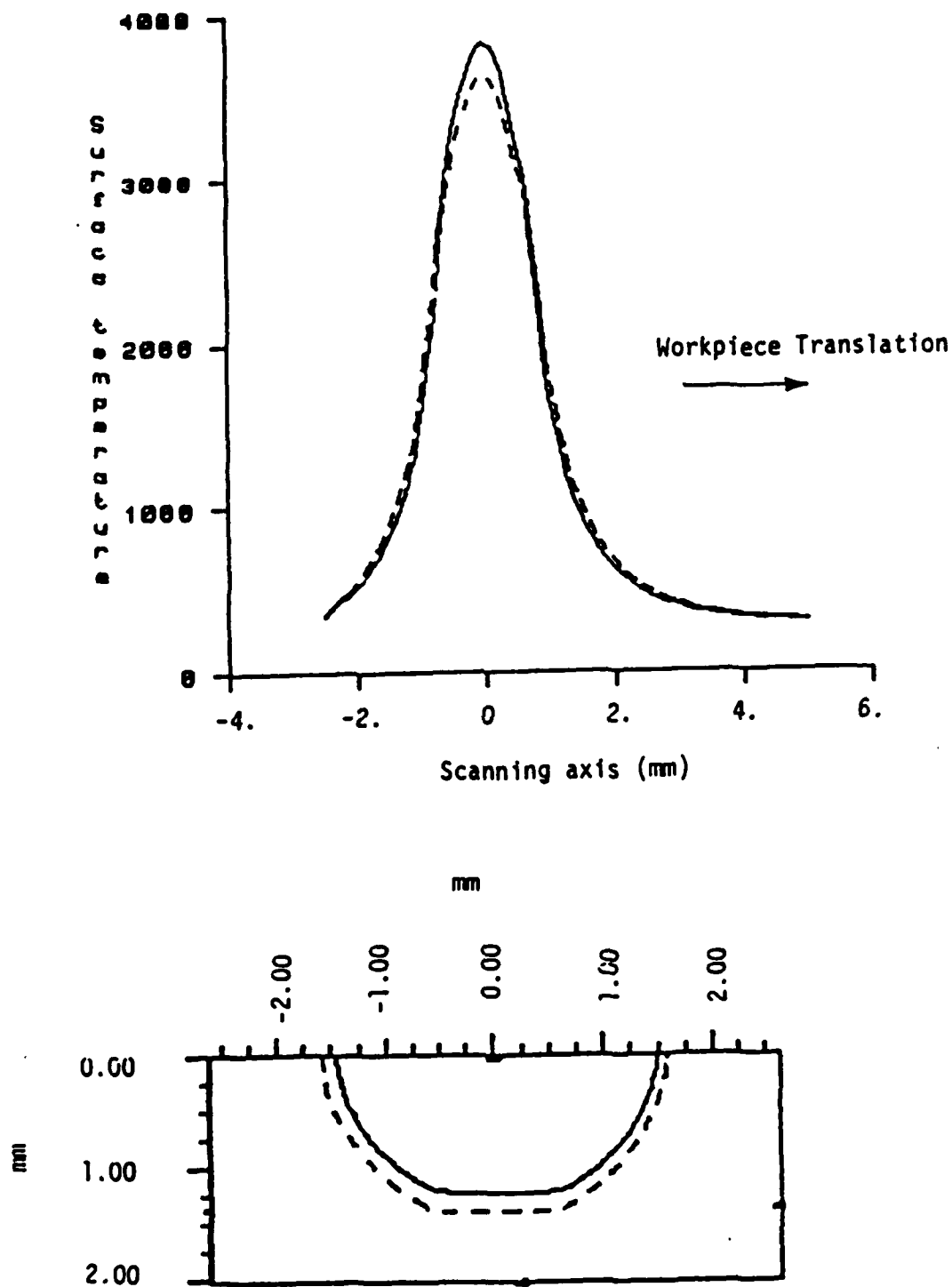


Figure 43 Surface Temperature Distribution and Melt-Solid Interface for 5 kW, f/7; With and Without Plasma Effects

defined as the laser spot size divided by the target translation speed. Thus a larger spot size results in a larger interaction time or a longer beam duration on any given point on the target.

The effect should occur at nearly all laser powers as the trend is for beam refraction to increase with laser power. Further modeling efforts have been hindered to date by the inability of the target model to converge at higher laser powers. The result is that if these difficulties can be overcome and a plasma model can be developed, complete a prior determination of melt volume (HAZ) can be achieved.

5. NUMERICAL MODEL

Several efforts have been made in modeling the steady-state plasma formation for CW laser radiation in pure gases. A complete review of these efforts can be found in Ref. 20. Early models were typically one-dimensional, using cylindrical (non-focused) beam geometries. Simplifying assumptions regarding the non-linear thermophysical properties of the high temperature gas were made to form analytical solutions. More recently, converging beam geometries and real gas properties have been incorporated in numerical solutions. One of the first successful two-dimensional, real gas, converging beam geometry models was reported by Glumb and Krier [22]. Recently a complete solution of the incompressible Navier-Stokes equations for a plasma system has been reported by Jeng and Keefer [24]. This investigation reports the development of a model following the procedure of Glumb and Krier [22]. The results of Jeng and Keefer [24] will be discussed and possible future enhancements.

5.1 Model Formulation

The physics of plasma formation above metallic targets were discussed in Chapter 2. The main difference between this type of plasma and a pure gas plasma is the existence of an upstream boundary condition (target surface) which affects the plasma formation via the vaporization characteristics of the target material. Figure 44 is the cylindrical domain used in the solution procedure. For the first model, zero radial flow is assumed. Further, since the axial Mach numbers have been measured to be on the order of 0.05 to 0.1, axial convection has also been neglected. The results of Jeng and Keefer [24] in flowing gas

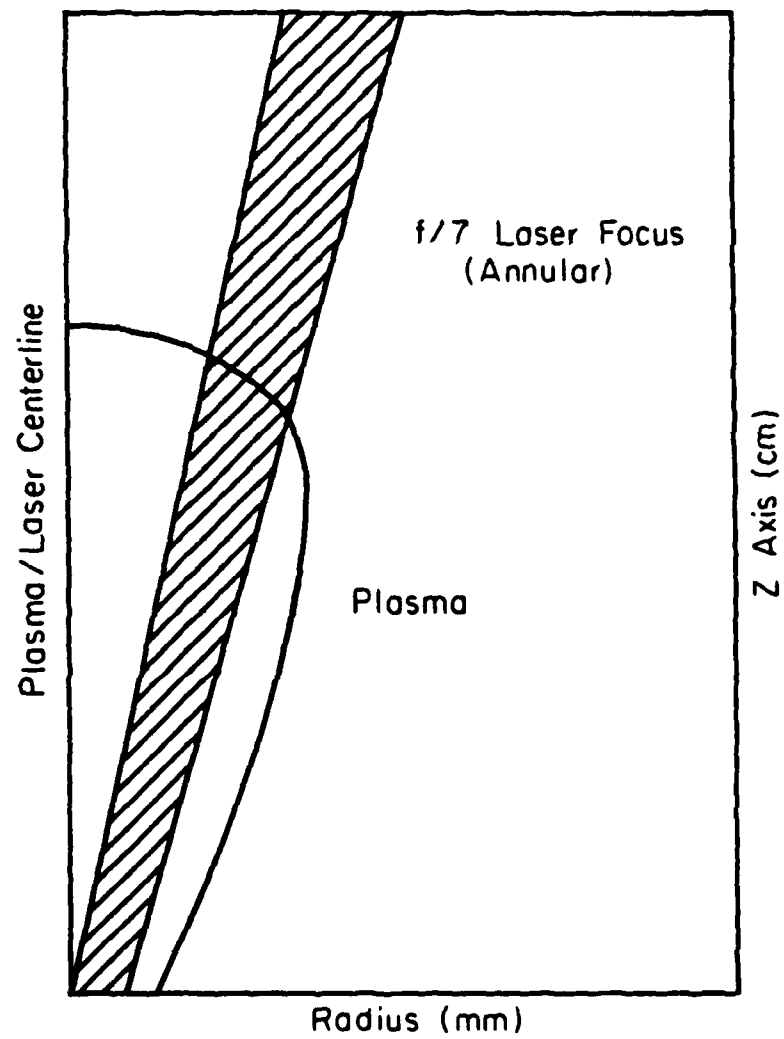


Figure 44 Cylindrical Domain of Metal-Gas Plasma Model

systems indicate nearly zero axial flow velocities in the plasma core, supporting the zero axial flow assumption.

The boundary conditions are as follows:

- a) centerline symmetry (adiabatic),
- b) free boundaries at upper- and outer-most cylindrical grid locations, and
- c) heavy particle temperature distribution known at the target surface.

Boundary condition a) is self-explanatory. Boundary condition b) is such that a fictitious final grid temperature is extrapolated from the two outermost iterated grid temperatures. The conduction losses across the two faces will then be calculated and used in the convergence test of the energy equation. Boundary condition c) results from a target transport model [67]. The temperature distribution is close to Gaussian with the peak temperatures being a few degrees above the melting point of the target material.

With the above assumptions and boundary conditions, the energy equation takes the form:

$$\frac{\partial}{\partial Z} \left[K \frac{\partial T}{\partial Z} + \frac{1}{r} \frac{\partial}{\partial r} (rK \frac{\partial T}{\partial r}) \right] - \rho u C_p \frac{\partial T}{\partial Z} + \alpha I - P_r = 0 \quad (5.1)$$

Where K is the temperature dependent conductivity, $\rho u C_p$ is the convection term, αI is the absorbed laser power, and P_r is the radiative loss term.

5.2 Solution Procedure

Equation 5.1 can be reduced to a difference form using the grid shown in Fig. 45.

$$\begin{aligned} & \bar{K}_W A_W \frac{(T_W - T_C)}{\Delta r} + \bar{K}_E A_E \frac{(T_E - T_C)}{\Delta r} + \frac{\bar{K}_N A_N (T_N - T_C)}{\Delta z} \\ & + \bar{K}_S A_S \frac{(T_S - T_C)}{\Delta z} + \rho u A_S C_{ps} T_S - \rho u A_S C_{ps} T_C + P_{abs} - P_{rad} = 0 \quad (5.2) \end{aligned}$$

\bar{K}_i corresponds to the average conductivity between the cells in question. Equation (5.2) and the modified forms at the various boundaries can be solved for T_C as explicit forms of the surrounding cell temperatures. The non-linearity of the gas properties prevents direct matrix reduction of the system and a Gauss-Seidel iterative procedure is used as in Ref. 22.

The laser beam is focused into the plasma grid, currently set at $f/7$. For simplicity, the beam is modeled as a Gaussian annular intensity profile. The iteration begins at the upper central grid and rasters radially and then axially, etc. The beam is geometrically propagated into the grid and each cell along the radius is checked to determine the percentage of the north boundary exposed to the laser beam. The local absorption coefficient and absorbed power is then calculated for use in Eqn. (5.2). The average conductivity between N, S, E, and W cells and the center cell is calculated as well as the radiative loss term at $T_C(OLD)$. The results are used in Eqn. (5.2) to determine the new grid temperature, $T_C(NEW)$. The procedure is amenable to the incorporation of an over- or under-relaxed Gauss-Seidel iteration procedure where the new cell temperature is determined by:

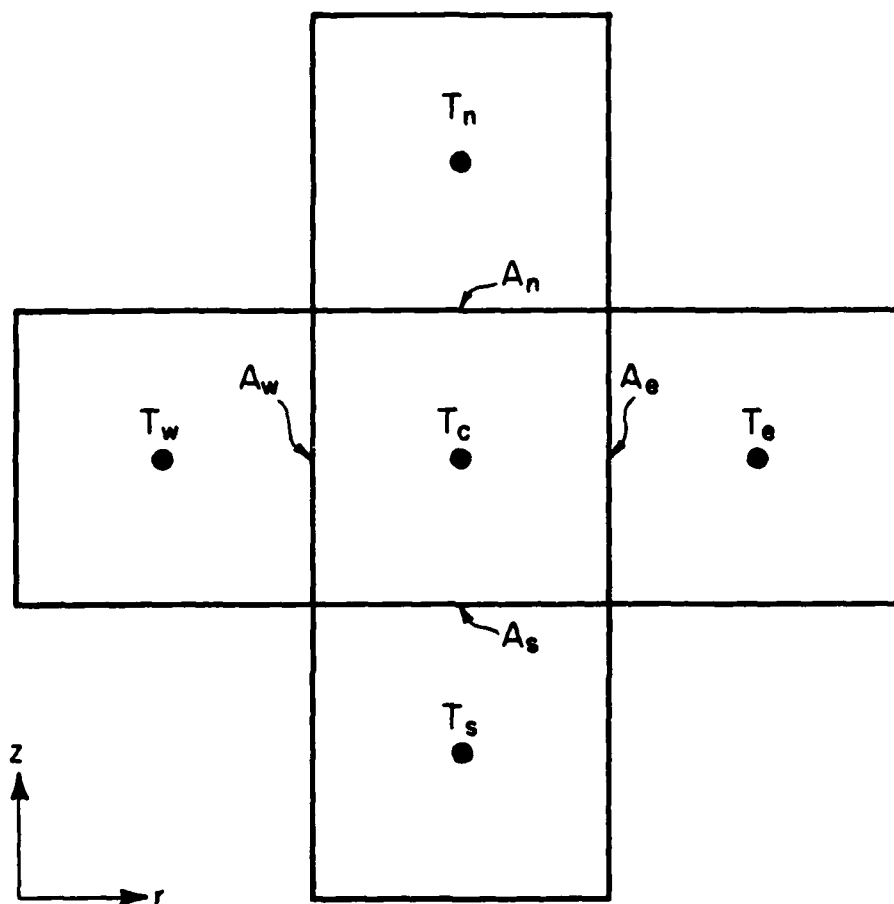


Figure 45 Metal-Gas Plasma Model Grid

$$T_{NEW} = T_{NEW} + W(T_{NEW} - T_{OLD}) \quad (5.3)$$

W is the weighting factor, 0 - 1 for the under-, and greater than unity for the over-relaxed case.

Once a given iteration has been performed the radiative losses and laser absorption are summed over the entire grid and an energy balance of the form:

$$P_{abs} - P_{rad} - P_{COND, N, S, E} - P_{CONV, N} = 0 \quad (5.4)$$

is checked for convergence.

5.3 Argon Properties

Argon has been used in this model since it was also used in the pure gas model and argon is frequently used as an assist gas in laser material processing. The electron number density was calculated from LTE considerations and the equilibrium after Dresvin [27]. The values include contributions from the second ionization stages at temperatures above 16,000 K. Figure 46 shows the variation of electron number density with electron temperature. The decline in population above 17,000 K corresponds to the slight decrease in ion production until the second ionization stage contributes significantly at about 20,000 K.

The inverse bremsstrahlung absorption coefficient is calculated following the work of Wheeler [30] and Stallcop [31] and was shown as Eqn. (2.3). The net result is that Wheeler's corrections account for

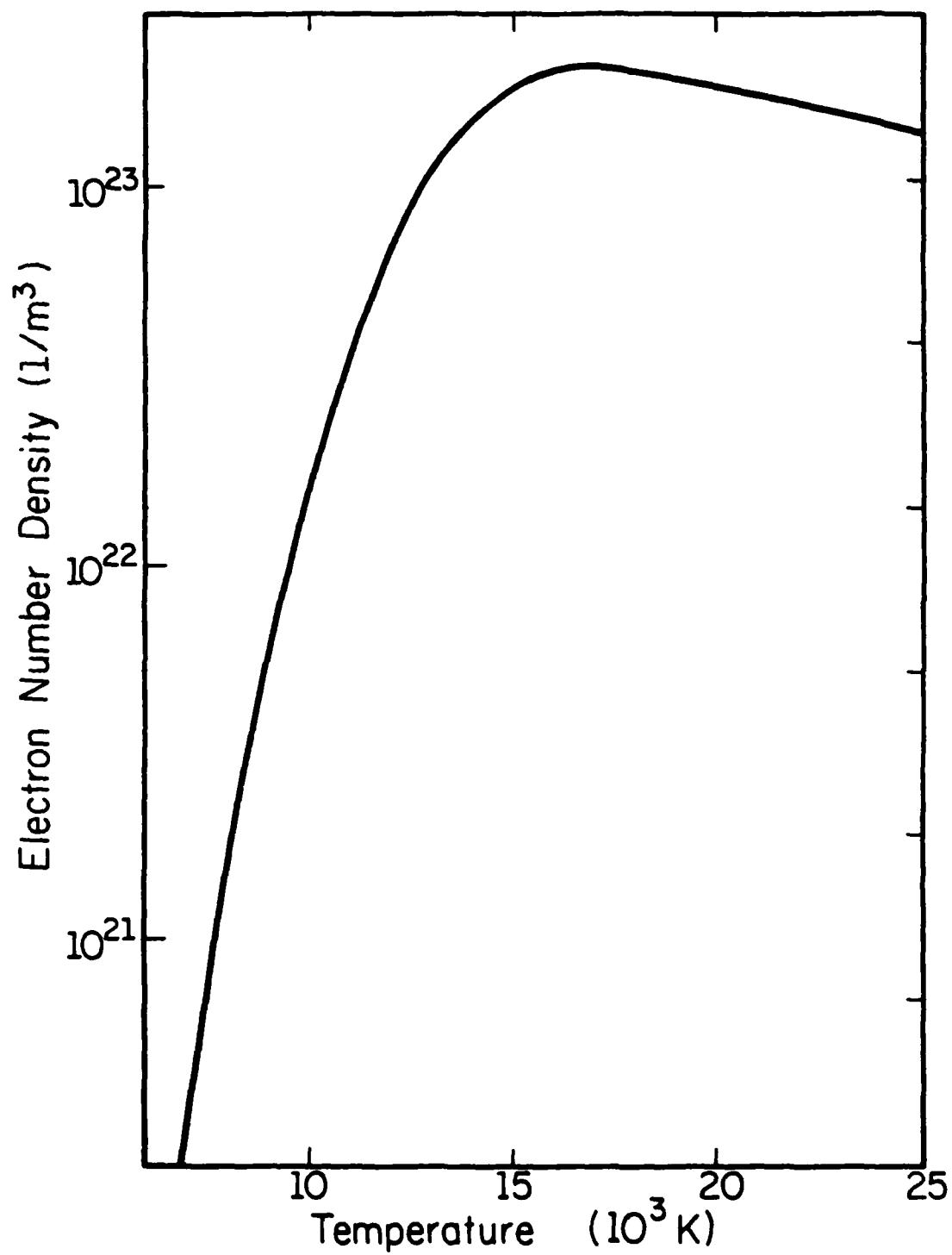


Figure 46 Electron Number Density for 1.0 atm Argon

photonization and non-hydrogenic behavior. Stallcop's effective Gaunt factor accounts for electron-neutral IB absorption at the lower temperature range. Figure 47 shows the absorption coefficient behavior as a function of electron temperature.

Thermal conductivity as calculated using gas kinetic theory does not agree with experimental measurements. This can be seen in Fig. 48. The discrepancy arises from the inability of experiment to discriminate between thermal conductivity and contributions from radiative absorption. Thus, the experimental data can be used in the modeling effort and radiative transport within the plasma will be automatically accounted for.

Radiation losses are more complex as both continuum and line radiation terms are present. As was shown in Chapter 2, the continuum emission is accurately modeled, on an integrated basis, by the Kramers-Unsold theory [58]. However, line radiation must be summed over all energy levels, a difficult task at best. Several experimental efforts concluded that the line radiation was the same magnitude as continuum losses and thus the continuum was doubled. The result is valid up to approximately 13,000 K. Kozlov [65] derived an expression for the line radiation as a multiplication factor of the continuum losses at a given electron temperature. The calculation was made on the basis of a smeared line spectrum where the line energy was modeled as perturbations on the continuum centered at the wavelength in question. In this manner, closely spaced discrete line spectra could be lumped into an analytical expression. The total emission is shown in Fig. 49 with the continuum contribution (Eqn. 2.15) shown for reference. More

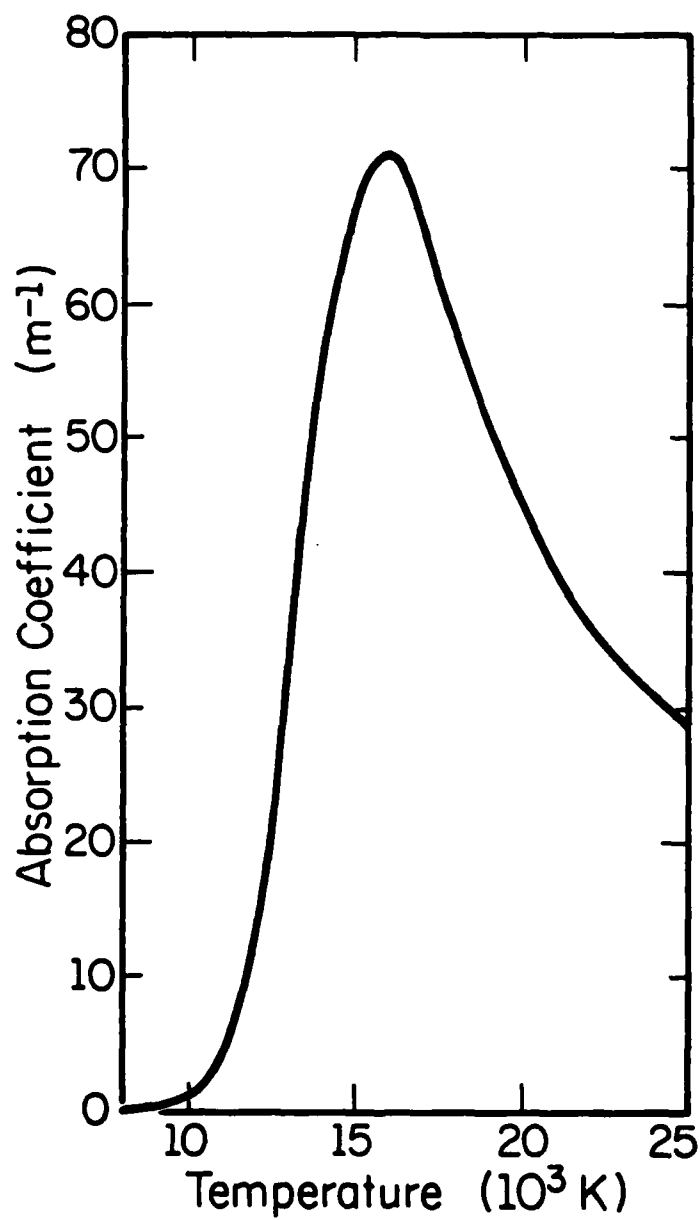


Figure 47 Inverse Bremsstrahlung Absorption Coefficient for 1.0 atm Argon

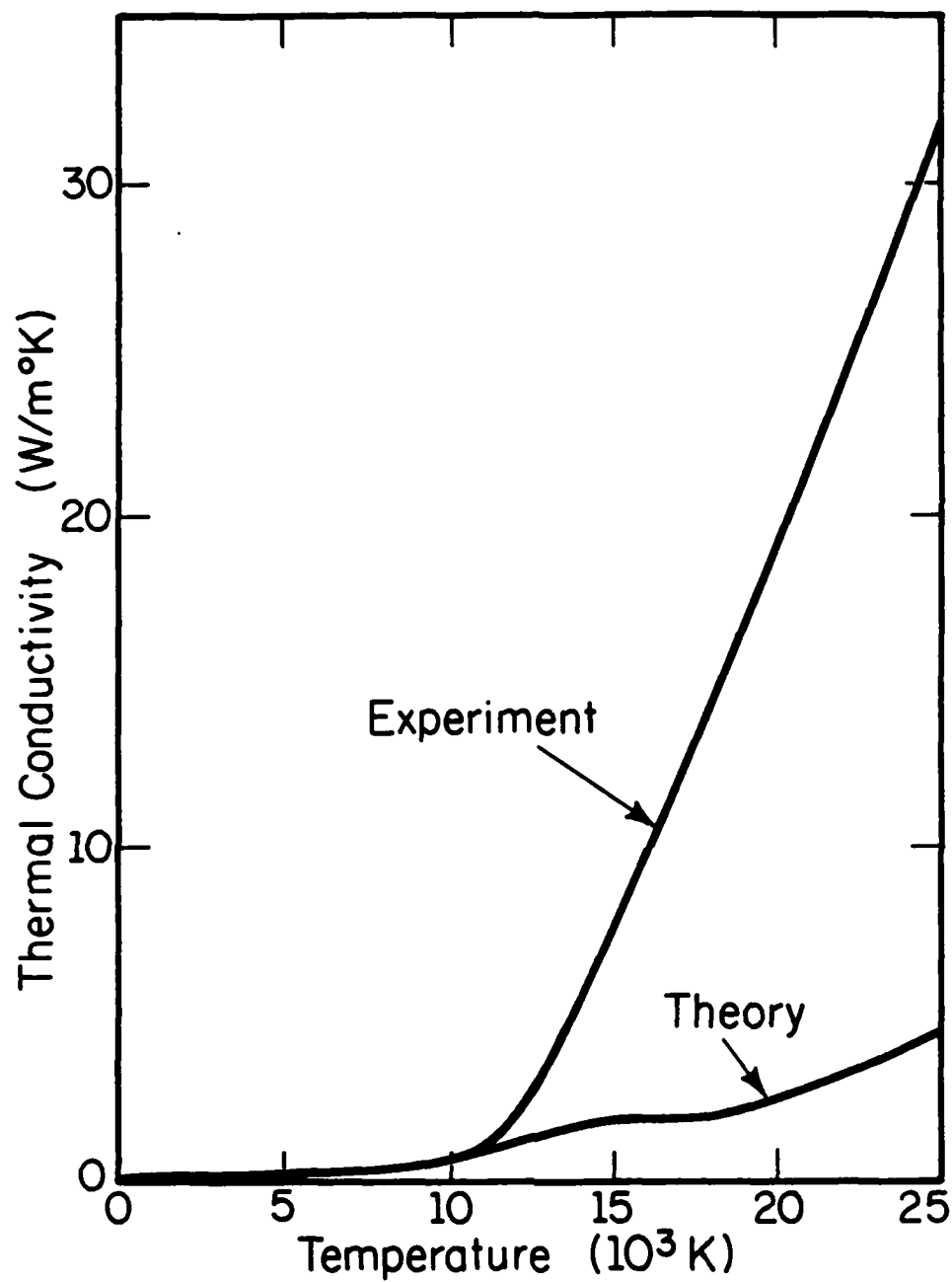


Figure 48 Thermal and Radiative Conductivity
for 1.0 atm Argon

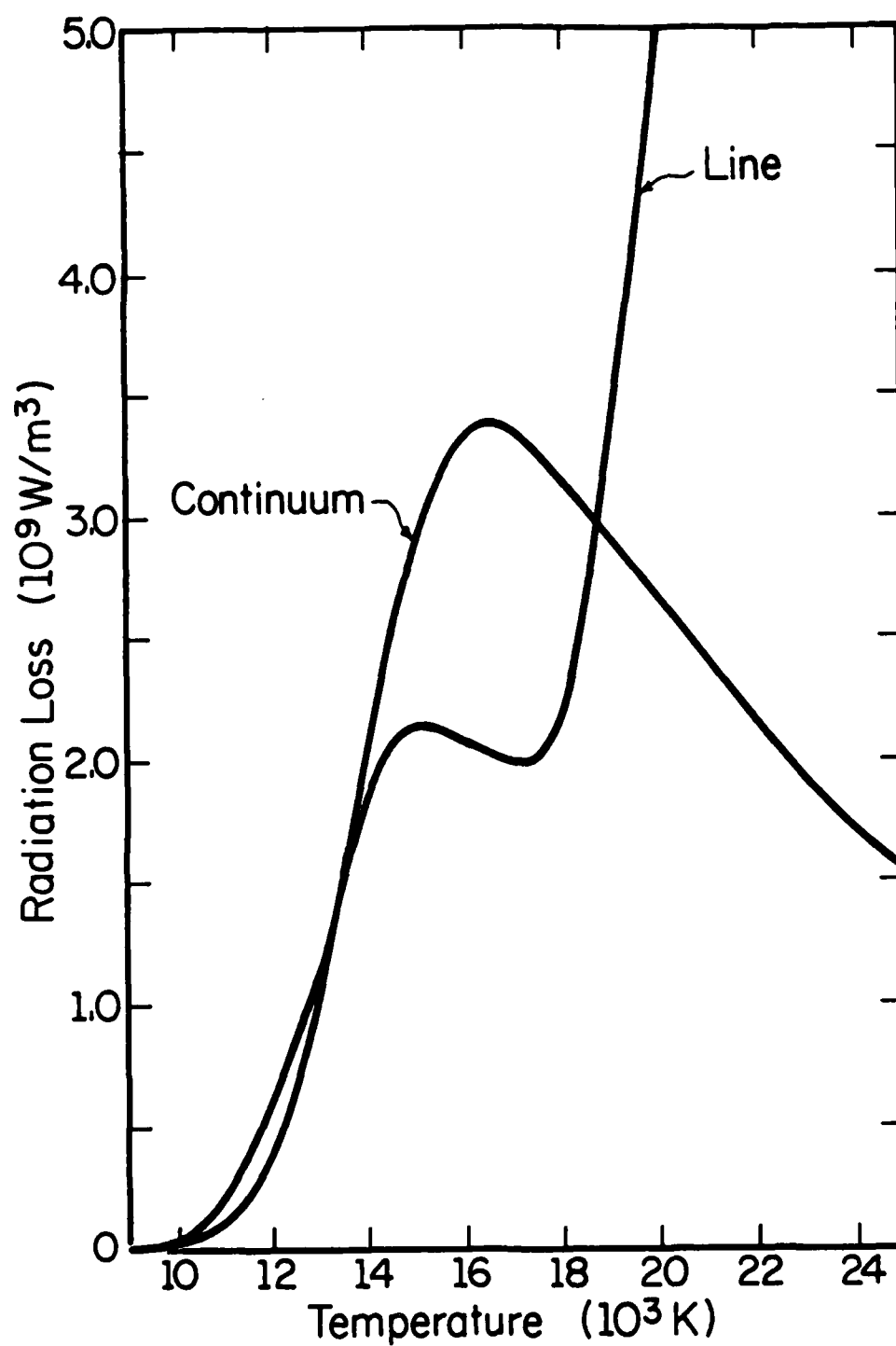


Figure 49 Line and Continuum Radiative Losses for 1.0 atm Argon

information on the argon properties can be found in the thesis of Dr. Ron Glumb [49].

5.4 Results: Comparison with Experiment

Figure 50 depicts the flow diagram for the plasma model. The spatial dimensions of the plasma grid and laser beam are read from a data file. The initial temperature grid is set to a constant value of 10,000 K or greater, otherwise a previous solution grid is read.

The boundary conditions are as mentioned before. The upper and outer boundaries are currently set to 300 K simply to minimize convergence time. The current code takes between 1000 and 2000 iterations to reach convergence of the energy equation.

There was a concern over the target surface boundary condition. It was desired to find a relationship between the experimentally observed electron temperatures in excess of 10,000 K and the predicted heavy particle temperature far below this value. Initially a non-thermochemical equilibrium scheme such as proposed by Lukens and Incropera [41] was desired. The authors cited imbalance between ohmic heating and elastic electron energy transfer as a source of thermal non-equilibrium between electrons and heavy particles. The effort was for a cylindrical arc plasma in which thermal conductivity at the anode walls could be neglected with respect to ohmic heating. Clearly this is not the case for a laser supported plasma and the unwieldy task of performing the thermal conductivity balance was undertaken. The results of predicting a temperature difference based on the local E-field magnitude were suspect, especially at E-fields above a few hundred V/cm, which is the case for laser radiation.

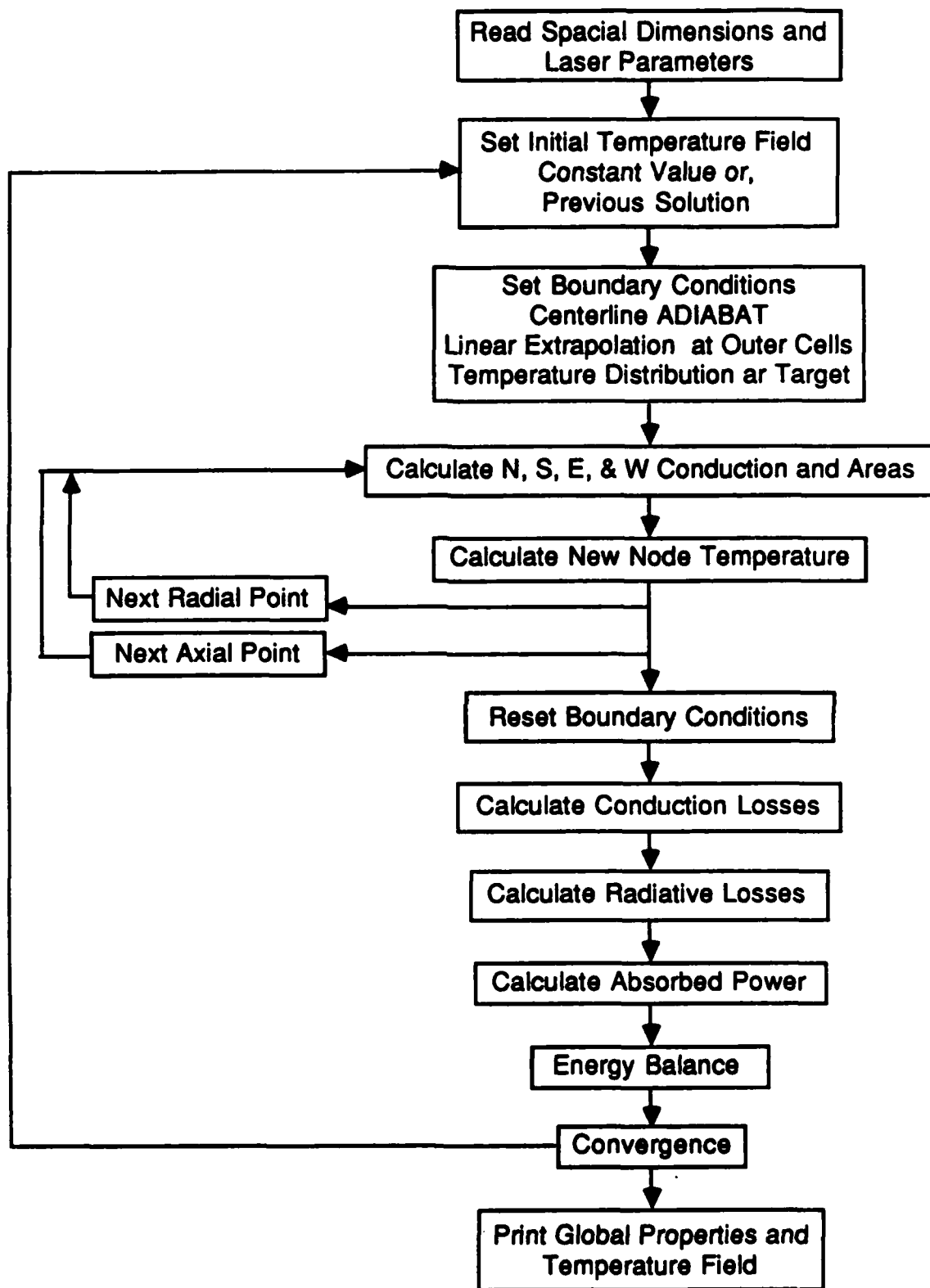


Figure 50 Metal-Gas Plasma Model Flow Diagram

After it was demonstrated by the modified target model that the heavy particle surface temperature distribution varied significantly with target material, it was decided to use this as the lower boundary condition. The Knudsen jump approximation [40] is applied to the predicted surface temperature distribution, lowering the temperature between 5 and 35 percent, depending on keyhole pressure conditions. This effect follows the laboratory observation that the plasma formed above a steel target is larger than a plasma above an aluminum target, and thus the predicted surface temperature distribution has been used as a first approximation.

The conduction heat transfer to the adjacent nodes, power absorption, and radiative losses are calculated for each cell. The algorithms are nearly identical to those used in the data reduction code. The exception is power absorption. In the data analysis code, the laser beam was broken into 20 rays, each weighted to a Gaussian annular intensity profile. The integration (piece-wise summation) of the inlet and exiting ray bundle defined power absorption. The intensity is necessary as the local absorption coefficient operates on intensity, not power, as defined in Chapter 2. In the model the local intensity is assumed to be an annular Gaussian distribution and local power is determined by integrating the "absorbed" intensity over the beam area.

The model was initially run with zero convection. The result is that the model overpredicts absorption when compared to the experimental results. Figure 51 is a comparison of the zero flow condition and the experimental results that were shown in Fig. 38. The model predicts

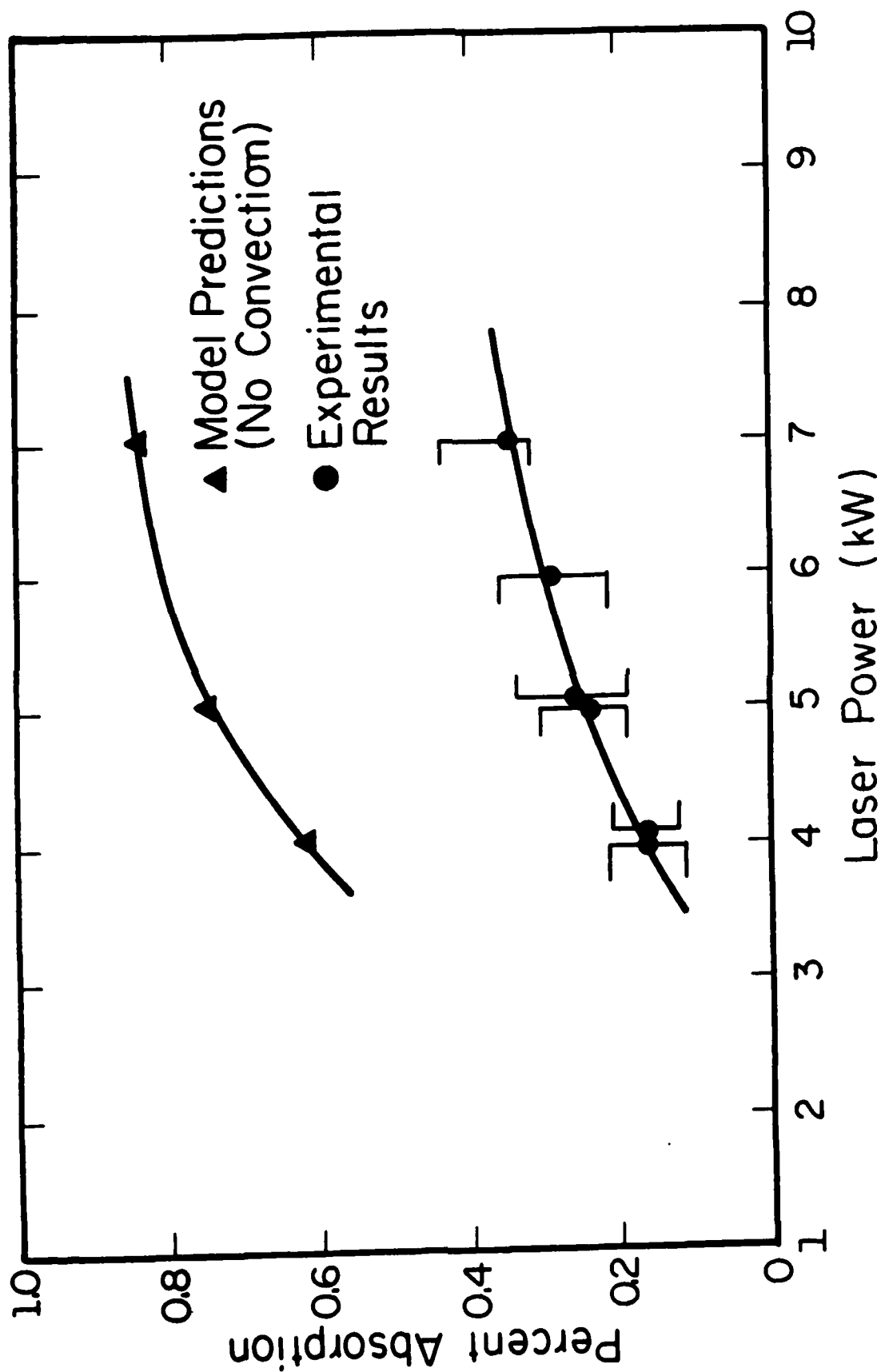


Figure 51 Plasma Model Predictions: Zero Convection, as a Function of Laser Power

approximately 3 times the absorbed laser power with respect to the experimental results. This would be physically impossible as the power transmitted to the target would be insufficient to support vaporization and hence the plasma. The experimental targets indicated that the laser had coupled to the target throughout the given trial, further supporting the above conclusion.

After the mechanics of the model code were checked, two possible solutions existed. First there is a large variation, in some cases in excess of ± 50 percent, in thermophysical properties from author to author [19,22,24]. One approach would be to alter the thermophysical properties within the model. The exercise was performed on the absorption coefficient and the model predictions agreed with the data to within the experimental error. However, the model has now been made empirical which is not the goal. More importantly, the full property values had been used in the data analysis algorithms and thus a paradox existed.

The second alternative was to include convection in the model and was incorporated via Eqn. (5.2). Recently, the target transport model [67] has predicted Mach numbers on the order of 0.3 outside the Knudsen layer. From the predicted heavy particle temperature, assuming atmospheric pressure within the plasma, the gas density and speed of sound were calculated. The prediction of $M = 0.3$ appears high with respect to measured velocities implying $M = 0.01$ to 0.005 . Thus, the Mach number was left as a free parameter input to the model.

The Mach number was varied and by trial-and-error a Mach number of 0.0001 was found to result in a model solution which agreed with the

experimental results. The manner in which the Mach number is incorporated into the plasma model, the corresponding gas velocity at $M = 0.0001$ is approximately 100 mm/sec. Figure 52 is a comparison of the $M = 0.0001$ predicted temperature field and the experimental results as taken from Fig. 37b.

One sees that fair spatial agreement has been obtained. The model still overpredicts absorption at the given Mach number. At larger Mach numbers the model grid relaxes to 300 K throughout, which is interpreted as plasma "blowout". Figure 53 shows the model predictions as a function of laser power. The experimental results are shown for comparison.

The relatively low flow velocity is not unexpected in light of the experimental measurements [67] and the predictions of a full two-dimensional model [24]. Both note low axial flow velocities within the plasma core at Mach numbers on the order of 0.01 or less. The measured flow velocities [67] were between 80 and 120 mm/sec. Thus the model solution at 100 mm/sec appears to be a reasonable first iteration. The main conclusion is that the plasma core flowfield must be quantified prior to significant revisions of the current plasma model. The surface boundary condition should also be investigated further.

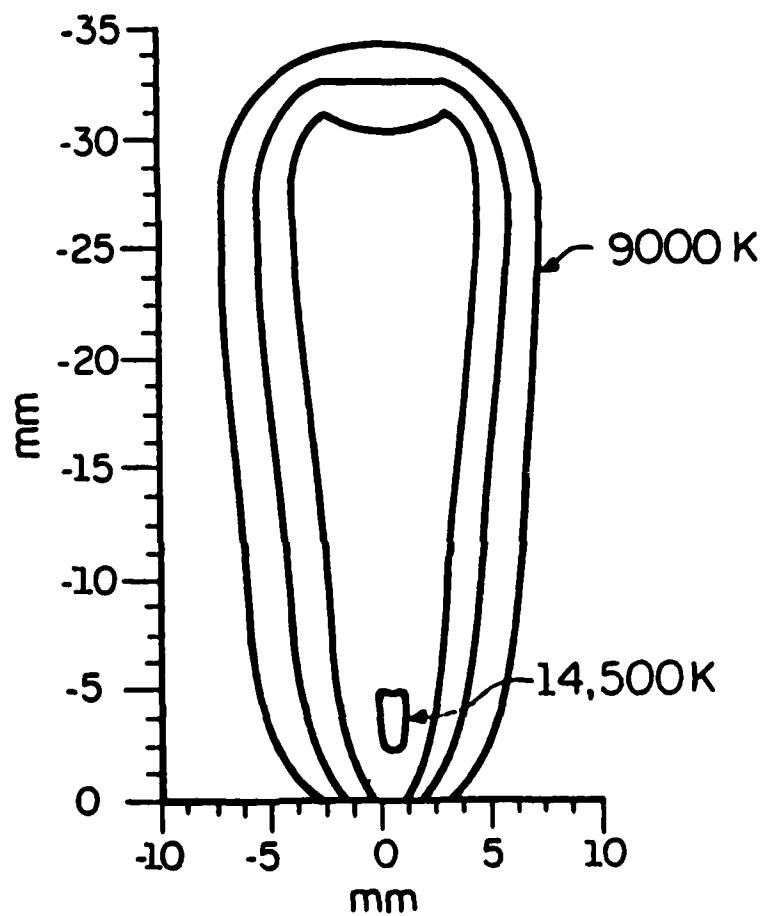


Figure 52 Model Prediction of 5 kW, f/7 Laser Supported Plasma Above an Aluminum Target

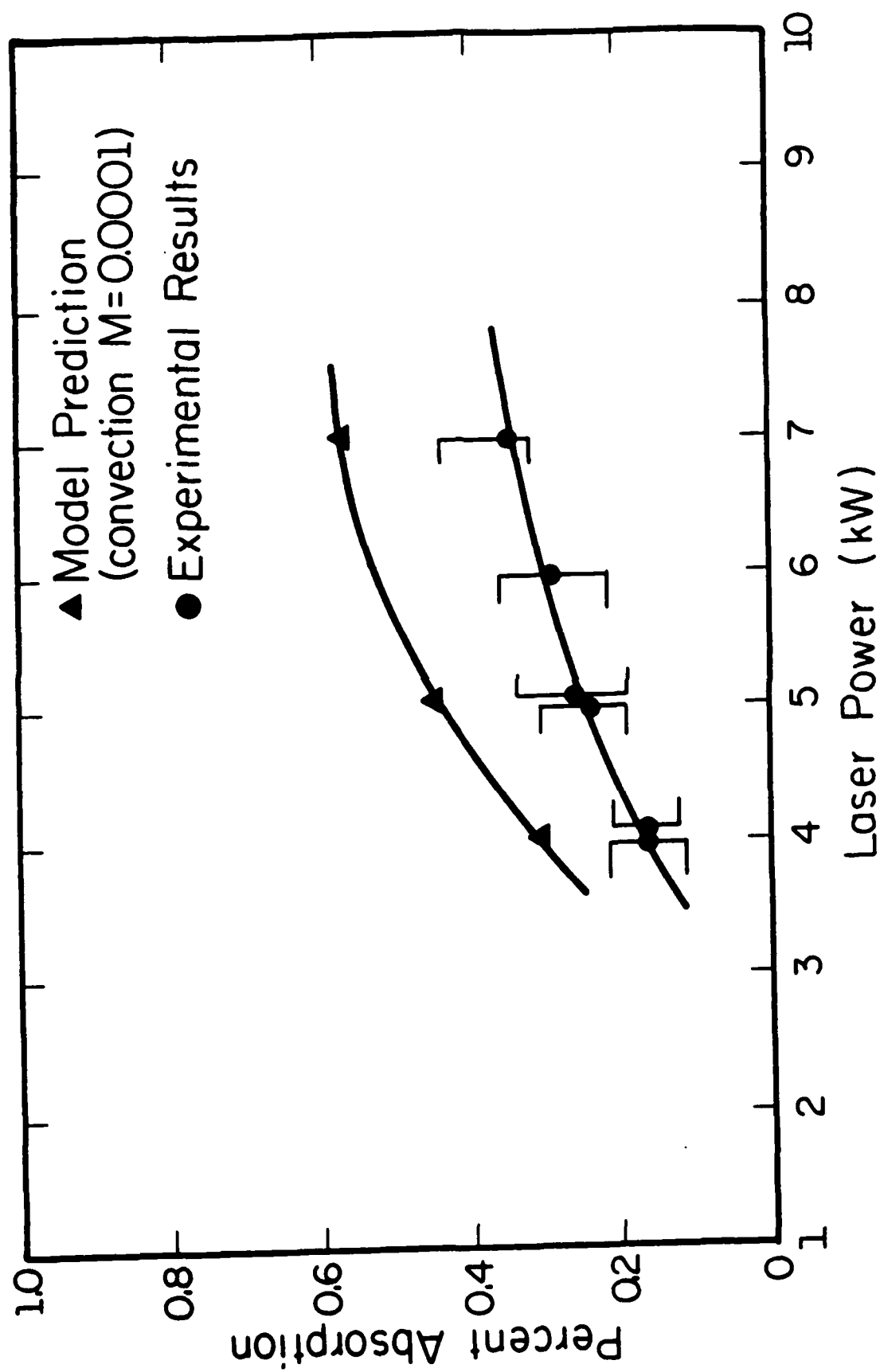


Figure 53 Plasma Model Predictions: Convection with $u = 100$ mm/sec as a Function of Laser Power

6. CONCLUSIONS

The pure gas plasma studies are one of the first treatments of CW laser-sustained plasma at powers up to 10 kW. At the onset of the project many concerns were expressed concerning plasma generation. First, initiation was to be a problem due to the high laser intensities required for breakdown of a room temperature gas. This was circumvented by the use of thin zinc foils and more recently a reusable tungsten rod. Initiation is now routine and our techniques have been used by others [23].

Another area of concern was plasma maintenance and stability. It was thought that the plasma may extinguish due to laser fluctuations or flowfield variations near the focus. Neither laser or flowfield fluctuations were seen to alter the plasma behavior. The effect may become critical at higher pressures and flowrates, but the numerical modeling [22,24] and other experiments [23] have not indicated any alteration in plasma stability.

Radiative loading of the chamber was a concern. Experiments have been limited to sub-ten minute intervals with cooling periods in between to prevent chamber damage. As thermal efficiencies are improved the problem may be circumvented. Other engineering techniques could be utilized such as reflective inner chamber walls and regenerative cooling of the chamber by the propellant system. The argon systems have shown promise for laser propulsion. No critical area has been demonstrated which would be fatal to the concept of laser propulsion. Thermal efficiencies on the order of 40 percent and absorption in excess of 75 percent have been demonstrated.

The spectroscopy work is one of the first two-dimensional studies of laser supported plasmas over a wide range of laser power and flow-rate. The work is the first study in which the spectroscopic data was checked for continuity against independent experimental diagnostics. Agreement between the spectroscopic data and the experimental data [2] and the numerical model [22] have allowed the development of new regimes of plasma propulsion.

To reduce radiative losses, higher $f/\#$'s have been theoretically shown feasible. The concern for plasma stability at $f/\#$'s above $f/10$ is questionable in light of the results of the other concerns addressed previously. The current system has been limited to $f/3$ or less and the current plans are to install $f/8$ to approximately $f/16$ optics. Splitting of the laser beam into multiple foci is another proposal to be tested. It is theorized that two smaller, more efficient plasmas will operate more efficiently as a whole rather than a single plasma. The radiative loading of the chamber walls would also be reduced by the energy absorbed between the plasmas.

The laser-supported plasma propulsion concept appears feasible and the types of engineering refinements previously mentioned should be investigated. In lieu of a full scale laser system, a more complete mapping of plasma characteristics is prerequisite to defining scaling laws for full-scale systems.

With respect to the hardware and software required to acquire and reduce the spectroscopic data, several items are in need of improvement. First, the bottleneck in the system is data transfer between the acquisition and reduction stages. As future software

enhancements from EG&G are released, the in-house software should be generated to dump OMA data to the CYBER or HP computing systems. The OMA has an RS-232 serial port for this function, but to date, the port has not been addressable.

The Abel inversion used in the data reduction is functional, not sophisticated. Many efforts have been devoted to the subject (see Appendix A) and more sophisticated algorithms are available. The question remains as to whether the university's computational software will support the required utilities. Another possibility would be remote access of the algorithms. The hardware for the data acquisition was designed to be flexible and should support most applications with only minor adjustments.

A first attempt at a numerical model has also been undertaken. The model currently predicts power-dependent plasma volumes that are consistent with the experimental results. The model, as run for aluminum, predicts no plasma formation for laser powers below 4 kW at $f/7$, which is also consistent with experiment. The model currently overpredicts global absorption when compared with the experimental results. The absorption trends, however, follow experiment.

The two-dimensional spectroscopic studies of CW laser-supported plasmas above metallic targets are the first to be found in the literature. The conclusions are based on the consistency of the spectroscopic data in pure gas systems with respect to independent measurement techniques. The plasmas were found to have little or no metallic spectra in the emission profiles and were treated as pure argon plasmas, which is in agreement with other studies [10,51,52]. The plasmas were

experimentally determined to absorb 15 to 35 percent of the incident laser radiation at laser powers between 4 and 7 kW. Temporal measurements of the plasma event indicated that the plasma is a CW event and does not initiate, propagate, extinguish, and re-initiate as proposed by another investigation [17]. OMA system was used at 50 μ s scanning times with scan-to-scan times of 100 μ s for temporal resolution. Future experiments might try to verify the results with transmission measurements using a fast photodetector. The plasma was also shown to radiatively behave essentially as a pure argon plasma. This conclusion was drawn from the inability to resolve aluminum spectra except for resonant structures within the first few millimeters of the target surface. This also simplified data analysis and is consistent with other studies. Future efforts might reconsider the near surface behavior of the plasma to determine if the metallic species significantly affect plasma absorption. Intuitively, the effect should be at most a few percent.

More importantly, the plasma has been shown, in theory, to significantly refract the laser beam, altering the energy distribution at the target. When recently coupled with a three-dimensional target conduction model [67], the result was that the HAZ was increased upon plasma formation. This supports the expected enhanced coupling regime noted by other authors as reported in Chapter 1. A metallographic study of the laser/plasma irradiated targets should be performed in a future effort. The study would indirectly support the refraction modeling and could be used to refine both the target and plasma models.

The above result is significant as it alone appears to explain the enhanced coupling effect. Many theories have been proposed including

plasma-target conduction and radiative transport. In the data analysis it was seen that conduction was small compared to the transmitted laser power. Radiative transport, as calculated using view factors on a point-by-point plasma volume analysis was also shown to be negligible even when assuming blackbody behavior by the target.

APPENDIX A: ABEL INVERSION

In Chapter 3, the Abel inversion technique that is used in this investigation was discussed. This appendix presents a detailed treatment of previous efforts and the details of the inversion code "NABEL".

Early on in spectroscopic work it was realized that line of sight measured values of an inhomogeneous plasma volume did not necessarily conform to local properties. Assuming circular symmetry, the line-of-sight intensity can be written:

$$I(y) = 2 \int_y^r \frac{\epsilon(r) r dr}{\sqrt{r^2 - y^2}} \text{ (W/cm}^2 \text{ - sr)} \quad (\text{A.1})$$

Typically, the measured quantity is the line-of-sight intensity, $I(\text{W/cm}^2 \text{ - sr})$. Equation A.1 is of the form of Abel's integral which can be inverted to yield:

$$\epsilon(r) = \frac{1}{\pi} \int_r^R \frac{(dI/dy) dy}{\sqrt{y^2 - r^2}} \text{ (W/cm}^3 \text{ - sr)} \quad (\text{A.2})$$

From this basic set of equations a large effort has been made by many investigators or analytical and numerical solutions.

One of the first treatments was made by Bockasten [68]. The intensity distribution was substituted by a third degree polynomial which is constrained to zero slope at the centerline from consideration of symmetry. A series of matrix coefficients were then calculated, centerline out, such that the local emissivity

$$\epsilon(r) = r_0^{-1} \sum_K a_{iK} N_K \quad (A.3)$$

where a_{iK} are the matrix elements, N_K the intensity data, and r_0 the outermost radius for normalization. The disadvantages of the techniques are that by starting at the centerline the error in a_{iK} is a minimum at the outer radii. This error is then propagated and summed inward when the matrix reduction occurs. However the technique works reasonably well for smooth, noise-free data, especially if the radial profile is near Gaussian.

Barr [69] derived a similar treatment using second order polynomials. The main contribution was a substitution for the dI/dy term in Eqn. (A.2) such that the integration (smoothing) was performed prior to differentiation (amplification of noise). The result was reduced error compared to the previous efforts. However, both techniques accumulate errors from outside in. This results in the prediction of negative emissive powers near the centerline if the profile is flattened. This is the case in many laboratory plasmas and in a majority of the plasmas in this investigation. Edels, Hearne, and Young [70] performed an analysis similar to Barr [69]. The authors broke the profile into equal sub-ranges and the integral at each point was replaced by the sum (Taylor series) of a series of integrals over the outer sub-ranges. The result was that a correction factor could be assessed, as well as errors, such that corrections to the inversion could be made numerically. However, the method still has similar problems near the centerline.

More recent efforts have included that of Cremers and Birkebak [63] as used in this investigation, the use of orthogonal polynomials [71], and derivative free inversion processes [72]. The last three inversion techniques have been demonstrated to have the ability to invert flattened profiles accurately. The Cremers and Birkebak was the simplest to program and demonstrated equivalent errors as the other two techniques. The method by Deutsch and Beniaminy [72] involves the integration by parts of Eqn. (A.2) and an expansion of the integrand assuming a well behaved function. This treatment appears to be the most rigorous to date. The code is available on the CPC Library at Queen's University of Belfast, N. Ireland. The technique's results were not satisfactory in this investigation and upon personal communication with Dr. Deutsch it was concluded that the IMSL cubic spline utilities were not accurate enough for the method to succeed. It may prove desirable in the future to investigate the routine further.

One final technique worth noting is that of Yasutomo, et al. [73]. The inversion process has been extended in this effort to accommodate asymmetrical profiles. The distribution is divided into even and odd (symmetrical and asymmetrical) components and a relative weighting function defined. The weighting function is a measure of the asymmetry of the data. The even part was inverted using Barr's [69] method. The inverted signal was then calculated via the product of the inverted even profile and the asymmetry function. The technique was developed for the highly asymmetrical profiles seen in toroidal plasmatrons. The technique may prove useful if future investigations find plasmas to be asymmetrical, e.g., horizontal laser axis where buoyancy may affect the plasma volume.

The numerical Able inversion code "NABEL" is currently supported on the laser lab UNIX® system. The code is accessible in the laser/todd/abeldata directory. Data file formatting is listed in the initial comments within the code. The code listing follows this text and the following is a brief walk through the process.

Several data statements at the beginning of the code are used in the calculation of temperature. The data statements contain the coefficients of the 415.8 nm line-to-continuum ratio as a function of electron temperature. Once the data file has been read the normalized position vector corresponding to the data points is calculated. A dummy vector is set at all data points and one point in between data to be used in the inverted data calculations. The number of data points is checked and the number of spline segments is determined based on previous error analysis. The radial profile (line and then corresponding continuum) is the cubic spline fit using the IMSL utility ICSVKU. Initial knot location estimates are made and the utility iterates the knot locations to minimize total curve error. Once the coefficients have been calculated, the error is calculated at each data point and the average data error per axial profile is printed in the output file "error".

The method of Cremers and Birkebak [63] assumes that the outer most intensity values are zero. Since the experimental data rarely obeys the rule, a correction is made. The finite outermost intensity value is linearly extrapolated to zero at the $N + 1$ radial point. The linear function has been integrated in Eqn. (A.2) and the result is an offset value added to the Abel kernel throughout the remaining evaluation of the given profile.

The inversion begins at the outermost point and segment of the radial profile. Equation (3.9) is used to calculate the inverted value. At the junction of two spline segments the kernel is summed over the previous spline kernel. The integration continues between the current radial point and the outermost knot of the given spline. The process continues to the centerline. The third, fourth, and fifth data points from the centerline are fit by a fourth order even polynomial and the first and second data points are extrapolated. This process insures symmetry at the centerline, one of the initial assumptions.

The ratio of the inverted line and continuum emissive powers are compared to the initial spline knots (data statements). Once the proper spline segment has been chosen the electron temperature is calculated from the spline coefficients. The ratio is also checked to insure it is within the temperature limits. If not, the data point is flagged high (20,000 K) or low (6,000 K) which is easily detected in the output file. The output file is then formatted in a rectangular grid. If a given radial profile has fewer points than the largest radial profile, the wings are strapped artificially to 9,000 K. The 9,000 K value was chosen to provide a skirt for the quasi-three-dimensional plotting code as the spectroscopic analysis cannot be used below 10,000 K. The 9,000 K value is not used in the absorption code and thus has no effect on radiation calculations.

The functions at the end of the code are the analytical forms of the first, second, and third degree integrals of Eqn (3.9). The outpile file "tempout" is formatted for direct use in either the plotting or transport analysis routines.

APPENDIX B: TRANSPORT CODE FOR EXPERIMENTAL DATA

The code "ABSORB3" was developed to calculate the laser beam attenuation, refraction, and radiative transport from a predefined temperature field (see Appendix A). The code sets up an incident laser beam intensity profile and divides the beam into 20 rays. Each ray is propagated at a measured angle until the first axial plasma temperature profile is encountered. The temperature profile is cubic-spline fit (8 knots) and the temperature at each ray location is evaluated. The temperature dependent absorption coefficient is evaluated and each ray is attenuated by

$$I_{OUT} = I_{IN} \exp(-\alpha \Delta Z) \quad (B.2)$$

where ΔZ is the optical path length through the given cell.

The temperature dependent number density [27] and subsequently the index of refraction are calculated for each ray position where

$$n(r) = (1 - \omega_p^2/\omega^2) \quad (B.3)$$

where ω_p is the plasma (electron) frequency and ω is the laser frequency. The new propagation direction is calculated using Snell's Law.

After the plasma has been traversed, the ray bundle is summed and compared to the incident ray sum to determine net power transmission, power being proportional to intensity. Each discrete temperature cell is used to calculate total hemispherical continuum radiative power lost

as derived in [59]. The power lost is modified by a factor of 2 to include line radiation at temperatures below 8,000 K. For temperature above 8,000 K, the line radiation factor as developed by Kozlov [65] had been used. The final output file is formatted for input to one of the various plotting routines.

APPENDIX C: NUMERICAL MODEL CODE LISTING

The following is a listing of the numerical model code for plasma formation above a metallic target. The details of the code were discussed in Chap. 5. The code is operational on the High Power Laser Lab HP 9000 computer system.

REFERENCES

1. Locke, E. V., Hoag, E. D., and Hella, R. A., "Deep Penetration Welding with High-Power CO₂ Lasers," IEEE J. of Quant. Elect., Vol. QE-8, Feb. 1972, pp. 132-135.
2. Pirri, A. N., Schlier, R., and Northam, D., "Momentum Transfer and Plasma Formation Above a Surface with a High-Power CO₂ Laser," Appl. Phys. Let., Vol. 21, Aug. 1972, pp. 79-81.
3. Lowder, J. E., Lencioni, D. E., Hilton, T. W., and Hull, R. J., "High-Energy Pulsed CO₂-Laser-Target Interactions in Air," J. of Appl. Phys., Vol. 44, June 1973, pp. 2759-2762.
4. Fowler, M. C., and Smith, D. C., "Ignition and Maintenance of a CW Plasma in Atmospheric-Pressure Air with CO₂ Laser Radiation," Appl. Phys. Let., Vol. 22, May 1973, pp. 500-502.
5. Engel, S. L., "Laser Cutting of Thin Materials," SME Paper MR74-960, Lasers in Manufacturing Conference, Chicago, IL, Dec. 1974.
6. Robin, J. E., and Nordin, P., "Improved CW Laser Penetration of Solids Using a Superimposed Pulsed Laser," Appl. Physics Let., Vol. 29, July 1976, pp. 3-4.
7. Duley, W. W., CO₂Lasers: Effects and Applications, Academic Press, 1976.
8. Von Allmen, M., Blaser, P., Affoltee, K., and Sturmer, E., "Absorption Phenomena in Metal Drilling with Nd-Lasers," IEEE J. of Quant. Elect., Vol. QE-14, Feb. 1978, pp. 85-88.
9. McKay, J. A., and Schriempf, J. T., "Thermal Transient Analysis of Pulsed Heat Deposition in Sheet Targets and Observations of Plasma Spreading," Appl. Phys. Let., Vol. 31, Sept. 1977, pp. 369-371.
10. McKay, J. A., Bleach, R. D., Nagel, D. J., Schriempf, J. T., Hall, R. D., Pond, C. R., and Manlief, S. K., "Pulsed-CO₂-Laser Interaction with Aluminum in Air: Thermal Response and Plasma Characteristics," J. of Appl. Phys., Vol. 50, May 1979, pp. 3231-3241.
11. Walters, C. T., Barnes, R. H., and Beverly, R. E., J. of Appl. Phys., Vol. 49, 1978, pp. 2937-2943.
12. Maher, W. E., and Hall, R. B., "Pulsed Laser Heating Profile Width and Changes in Total Coupling with Pulse Length and Pressure," J. of Appl. Phys., Vol. 51, March 1980, pp. 1334-1345.
13. Carlhoff, C., Krametz, E., Schafer, J. H., Schildback, K., Uhlenbusch, J., and Wroblewski, D., "Continuous Optical Discharges at Very High Pressure," Physics, Vol. 103C, 1981, pp. 439-449.

14. Rosen, D. I., Mitteldorf, J., Kothandaraman, G., Pirri, A. N., and Pugh, E. R., "Coupling of Pulsed 0.35 μm Laser Radiation to Aluminum Alloys, J. of Appl. Phys., Vol. 53, April 1982, pp. 3190-3200.
15. Miyamoto, I., Maruo, H., and Arata, Y., "Mechanism of Bead Transition in Laser Welding," Proc. of Int. Conf. on Welding Res. in the 1980's, Oct. 1980, pp. 103-108.
16. Bass, M. (Editor), Laser Materials Processing, North-Holland Publishing Company, 1983.
17. Donati, V., Garifo, L., Pandarese, F., Onorato, M., Lavorelli, P., LaRocca, A., and Cantello, M., "On the Ignition of Laser Supported Waves from Solid Targets by CW CO_2 Laser Radiation," AIAA Paper 84-1573, AIAA 17th Fluid Dynamics, Plasma Dynamics, and Lasers Conference, June 1984.
18. Wu, P. K., and Pirri, A. N., "The Dynamics of Air Plasma Growth in a 10.6 μm Laser Beam," AIAA Paper 78-176, AIAA 16th Aerospace Sciences Meeting, January 1978.
19. Muller, S., and Uhlenbusch, J., "Theoretical Model for a Continuous Optical Discharge," Physics, Vol. 112C, 1982, pp. 259-270.
20. Glumb, R. J., and Krier, H., "Concepts and Status of Laser-Supported Rocket Propulsion," J. of Spacecraft and Rockets, Vol. 21, Jan. 1984, pp. 70-79.
21. Krier, H., Mazumder, J., Rockstroh, T. J., Bender, T. D., and Glumb, R. J., "Studies of CW Laser Gas Heating by Sustained Plasmas in Flowing Argon," AIAA Paper 85-1551, AIAA 18th Fluid Dynamics and Plasmadynamics and Lasers Conference, July 1985.
22. Glumb, R. J., and Krier, H., "A Two-Dimensional Model of Laser Sustained Plasmas in Axisymmetric Flow Fields," AIAA Paper 85-1553, AIAA 18th Fluid Dynamics and Plasma Dynamics and Lasers Conference, July 1985.
23. Welle, R., Keefer, D., and Peters, C., "Energy Conversion Efficiency in High-Flow Laser-Sustained Argon Plasmas," AIAA Paper 86-1077, AIAA/ASME 4th Fluid Mechanics, Plasma Dynamics and Lasers Conference, May 1986.
24. Jeng, S-M., and Keefer, D. R., "Numerical Study of Laser Sustained Argon Plasmas in a Forced Convection Flow," AIAA Paper 86-1078, AIAA/ASME 4th Fluid Mechanics, Plasma Dynamics and Lasers Conference, May 1986.
25. Chan, C., Zehr, R., Mazumder, J., and Chen, M. M., "Three-Dimensional Model for Convection in laser Weld Pool," 3rd Engineering Foundation Conference on Modeling and Control of Casting and Welding Processes, Jan. 1986; proceedings to be published by AIME.

26. Chande, T., and Mazumder, J., "Two-Dimensional Transient Model for Mass Transport in Laser Surface Alloying," J. of Appl. Physics, Vol. 57, 1985, pp. 2226-2232.
27. Desvin, S. V. (Editor), Physics and Technology of Low-Temperature Plasmas, The Iowa State University Press, 1977, pp. 18-23.
28. Zeldovich, and Raizer, I. P., Physics of Shock "Waves and High-Temperature Hydrodynamics Phenomena, Academic Press, 1966.
29. Kramers, H. A., "On the Theory of X-ray Absorption and of the Continuous X-ray Spectrum," Philosophy Magazine, Vol. 46, 1923, p. 836.
30. Wheeler, C. B., and Fielding, S. J., "Absorption of Infrared Radiation as a General Technique for Determination of Plasma Temperature," Plasma Physics, Vol. 12, 1970, pp. 551-564.
31. Stallcop, J. R., "Absorption Coefficients of a Hydrogen Plasma for Laser Radiation," J. of Plasma Physics, Vol. 11, 1974, pp. 111-129.
32. Hughes, J. P., Plasmas and Laser Light, John Wiley and Sons, 1975, pp. 167-170.
33. Griem, H. R., Plasma Spectroscopy, McGraw-Hill Book Company, 1964, pp. 169-180.
34. Desvin, S. V. (Editor), Physics and Technology of Low-Temperature Plasmas, The Iowa State University Press, 1977, pp. 57-58.
35. Biberman, L. M., Norman, G. E., Ulyanov, K. N., Optics and Spectroscopy, Vol. 10, 1961, p. 297.
36. Raizer, I. P., "Subsonic Propagation of a Light Spark and Threshold Conditions for the Maintenance of Plasma by Radiation," Soviet Physics JETP, Vol. 31, Dec. 1970, pp. 1148-1154.
37. Desvin, S. V. (Editor), Physics and Technology of Low-Temperature Plasmas, The Iowa State University Press, 1977, pp. 35-39.
38. Raizer, I. P., Laser-Induced Discharge Phenomena, Consultants Bureau, 1977, Chapter 4.
39. Hughes, J. P., Plasmas and Laser Light, John Wiley and Sons, 1975, pp. 190-197.
40. Knight, C. J., "Theoretical Modeling of Rapid Surface Vaporization with Back Pressure," AIAA Journal, Vol. 17, May 1979, pp. 519-523.

41. Lukens, L. A., and Incropera, F. P., "Nonequilibrium in an Arc Constrictor," Inst. J. of Heat and Mass Transfer, Vol. 15, 1972, pp. 935-972.
42. Ushio, M., and Matsuda, F., "Mathematical Modeling of Heat Transfer of Welding Arc," Trans. of IWRI, Vol. 11, 1972, pp. 3-11.
43. Griem, H. R., Plasma Spectroscopy, McGraw-Hill Book Company, 1964, Chapter 6.
44. Eddy, T. L., "Critical Review of Plasma Spectroscopic Diagnostics Via MIE," IEEE Trans. on Plasma Science, Vol. PS-4, June 1976, pp. 103-111.
45. Farmer, A. J. D., and Haddad, B. H., "Local Thermodynamic Equilibrium in Free-Burning Arcs in Argon," Appl. Phys. Let., Vol. 45, July 1984, pp. 24-25.
46. Emmons, H. W., Physics of Fluids, Vol. 10, 1967, p. 1125.
47. Golden, D. E., and Bandel, H. W., Physical Review, Vol. 138, 1965, p. A14.
48. Bender, T. D., M. S. Thesis, University of Illinois at Urbana-Champaign, August 1985.
49. Glumb, R. J., Ph.D. Thesis, University of Illinois at Urbana-Champaign, October 1986.
50. Henricksen, B. B., and Keefer, D. R., "Experimental Study of a Stationary Laser-Sustained Air Plasma," J. of Appl. Physics, Vol. 46, Jan. 1975, pp. 138-150.
51. Key, J. F., Chan, J. W., and McIlwain, M. E., "Process Parameter Influence on Arc Temperature Distribution," Welding J., Vol. 62, 1983, pp. 1795-1845.
52. Mills, G. S., Welding J., 1977, pp. 93s-104s.
53. Tsao, K. C., and Pavelic, V., "Spectroscopic Studies of a Constricted Argon Plasma Arc," Paper 23, UK Welding Inst. Conf., 1982.
54. Kobayashi, M., and Suga, T., "A Method for the Spectral Temperature Measurement of a Welding Arc," Paper 18, UK Welding Inst. Conf., 1982.
55. Personal communications with Dr. Dennis Keefer, University of Tennessee Space Institute, January and October 1985, April 1986.
56. Personal communication with Dr. Hans Griem, University of Maryland, July 1985.

AD-A174 579

THE ROLE OF THE PLASMA DURING LASER-GAS LASER-METAL
INTERACTIONS (U) ILLINOIS UNIV AT URBANA DEPT OF
MECHANICAL AND INDUSTRIAL ENG T J ROCKSTROW ET AL

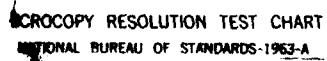
1/3

UNCLASSIFIED

13 OCT 86 UILU-ENG-86-4011 AFOSR-TR-86-1052 F/G 20/5

NL





57. Griem, H. R., Plasma Spectroscopy, McGraw-Hill Book Company, 1964, pp. 100-101.
58. Barzelay, M. E., "Continuum Radiation from Partially Ionized Argon," AIAA J., Vol. 4, May 1966, pp. 815-822.
59. Oettinger, P. E., and Bershader, D., "A Unified Treatment of the Relaxation Phenomena in Radiating Argon Plasma Flows," AIAA J., Vol. 5, Sept. 1967, pp. 1675-1632.
60. Wiese, Smith, and Miles, Atomic Transition Probabilities, NSROS-NBS 22, Vol. 11, National Bureau of Standards, 1969.
61. Tan, C-W, Ph.D. Thesis, University of Illinois at Urbana-Champaign, 1968.
62. Lerner, J. M., and Thevenon, A., "Optimizing Grating-Based Systems," Lasers and Applications, Jan. 1984, pp. 89-93.
63. Cremers, C. J., and Birkebak, R. C., "Application of the Abel Integral Equation to Spectrographic Data," Appl. Optics, Vol. 5, June 1966, pp. 1057-1064.
64. Cheng, J. K., and Casperson, L. W., "Plasma Diagnostics by Laser Beam Scanning," J. of Appl. Physics, Vol. 46, May 1975, pp. 1961-1965.
65. Kozlov, G. I., Kuznetsov, V. A., and Masyukov, V. A., "Radiative Losses by Argon Plasma and the Emissive Model of a Continuous Optical Discharge," Soviet Phys. JETP, Vol. 39, Sept. 1982, pp. 66-73.
66. Sparrow, E. M., and Cress, R. D., Radiation Heat Transfer, McGraw-Hill, 1978.
67. Chande, T., and Mazumder, J., "Estimating Effects of Processing Conditions and Variable Properties Upon Pool Shape, Cooling Rates and Absorption Coefficients in Laser Welding," J. of Appl. Physics, Vol. 56, October 1984, pp. 1981-1986.
68. Bockasten, K., "Transformation of Observed Radiances into Radial Distribution of the Emission of a Plasma," J. of the Optical Soc. of America, Vol. 51, Sept. 1961, pp. 943-947.
69. Barr, W. L., "Method for Computing the Radial Distribution of Emitters in a Cylindrical Source," J. of the Optical Soc. of America, Vol. 52, Aug. 1962, pp. 885-888.
70. Edels, H., Hearne, K., and Young, A., "Numerical Solutions of the Abel Integral Equation," J. of Math. and Physics, Vol. 41, 1962, pp. 62-75.

71. Minerbo, G. N., and Levy, M. E., "Inversion of Abels Integral Equation by Means of Orthogonal Polynomials," SIAM J. of Numerical Analysis, Vol. 6, Dec. 1969, pp. 598-616.
72. Deutsch, M., and Beniaminy, I., "Derivative-Free Inversion of Abel's Integral Equation," Appl. Phys. Lett., Vol. 41, July 1982, pp. 27-28.
73. Yasutomo, Y., Miyata, K., Himeo, S-I., Enoto, J., and Ozawa, Y., "A New Numerical Method for Asymmetrical Abel Inversion," IEEE Trans. on Plasma Science, Vol. PS-9, March 1981, pp. 18-21.

END

12-86

DTIC